Title	Self-phase Modulation Effects on the THz Radiation from a Two-color Laser Filament
Author(s)	巩, 辰
Citation	大阪大学, 2021, 博士論文
Version Type	VoR
URL	https://doi.org/10.18910/85392
rights	
Note	

Doctoral Dissertation

Self-phase Modulation Effects on the THz Radiation from a Two-color Laser Filament

(2色レーザーフィラメントからのTHz放射に対する自己位相変調効果)

Chen Gong

June 2021

Department of Electrical, Electronic and Information Engineering
Graduate School of Engineering
Osaka University, Japan

PREFACE

Recent advances in terahertz (THz) science and technology have made it one of the most promising research topics in the 21st century in the field of spectroscopy, remote sensing, imaging and other cross-cutting areas. Air-based THz generation-detection systems have many unique advantages compared with conventional time-domain spectroscopy (TDS) systems based on photoconductive antennas and optical rectification schemes, such as a wider radiation spectrum, high intensity, and the possibility of long-range operation. The method is based on the ultrafast pulse laser-induced filaments by focusing infrared (IR) fundamental wave (ω) and its second harmonic (2ω), in which the current surge is capable to generate intense wideband THz waves. This promising tool has attracted a lot of attention in recent years as a strong THz source which can be used in revealing intense THz field induced nonlinear effects, including nonlinear THz spectroscopy of condensed states, resonant and non-resonant control of materials and nonlinear response of metamaterials.

Despite the asymmetric transient current model successfully explains the theoretical principles of the two-color excitation scheme, the nonlinear effects in the filament associated with changes of the refractive index, which lead to various modulation effects of the output THz pulses, have not been studied in depth. In this dissertation, the intensity-dependent nonlinear effects in two-color filaments were experimentally investigated by observing the intensity evolution of the output THz pulses and its time domain waveform shaping. The physical mechanisms leading to these modulations are discussed in conjunction with theoretical models.

This dissertation is organized as follows: Chapter 1 is an overall introduction to THz science and technology. We enumerate the common methods of THz pulse generation and detection based on ultrafast laser pulse interaction with solid emitters and detectors and explain the advantages of an air-based two-color laser scheme. The problem of nonlinear effects that cannot be explained by microscopic models of two-color scheme is highlighted and motivates the research of this dissertation. Chapter 2 provides a brief introduction to the principle of laser filamentation process involves intensity dependent nonlinearities, mechanism of THz emission from two-color filaments, and air-biased coherent detection methods. Chapter 3 introduces our experimental results and discussion of intensity-dependent nonlinear modulation on the phase matching conditions during THz emission. The relative phase of the two-color pulse regulating this condition is influenced not only by the air dispersion, but also by the intensity-dependent plasma refractive index. We reveal that the additional phase is proportional to the incident laser field intensity utilizing a nonlinear fit. The fitting result is experimentally validated by the two-color spectral spread and elliptical polarization orthogonal component ratio. Chapter 4 explores the waveform shaping effect due to intensity variations. This phenomenon is explained by the modified photocurrent model based on the macroscopic coherent emission mechanism. High plasma density at the focal center causes a π phase slip between the two-color fields, resulting in a bipolar THz waveform. Weak photoionization near the front of the focus gradually affect the initial phase as the pumping energy increases, resulting in waveform shaping. And the slow-varying peak at the tail is caused by the fading of the residual current. Chapter 5 shows an example application of two-color laser filament THz-TDS system. We characterized the refractive index and absorption coefficient of cyclic olefin polymers (COPs), which is highly anticipated for future THz band applications. Its potential for application in THz lens, cuvettes and substrates of broadband transmission lines is also revealed. Chapter 6 summarizes the whole study.

ACKNOWLEDGEMENTS

I would like to express my sincere gratitude and appreciation to all the professors and colleagues who have helped me during these years and contributed in the realization of this dissertation.

First and foremost, I would like to thank my supervisor Professor Masayoshi Tonouchi at Institute of Laser Engineering, Osaka University, for giving me the opportunity to have such an experience. This work would not be possible without his mentorship and encouragement. He provided for many research ideas and a wonderful research environment throughout my Ph.D. years. I have really learned a lot from him over the years.

I would like to express my gratitude to Professor Ryuji Katayama at Division of Electrical, Electronic and Infocommunications Engineering, Graduate School of Engineering, Osaka University, for his valuable time to give me detailed and useful advice and guidance on this dissertation.

I am very grateful to Associate Professor Hironaru Murakami at Institute of Laser Engineering, Osaka University, for his precious and passionate scientific support and for being good mentor and fellow in different occasions. Sincere thanks to him for precise guidance and advice during the preparation of this thesis.

I wish to acknowledge Professor Yusuke Mori, Professor Mitsuhiro Katayama, Professor Masanori Ozaki, Professor Masahiko Kondo, Professor Nobuya Mori, and Professor Tetsuya Hirose at Division of Electrical, Electronic and Infocommunications Engineering, Graduate School of Engineering, Osaka University, for their guidance, helpful discussions and valuable comments on this thesis.

I would like to express my thanks to Associate Professor Takahiro Teramoto at Institute for Radiation Sciences, Osaka University, for his insight and efforts in our collaboration. He has also guided me through the completion of this work as well as suggestions to my researches.

My sincere thanks to Associate Professor Iwao Kawayama (currently at Kyoto University) for collaboration during preliminary investigations, and constructive criticism to this work.

I would like to thank Dr. Zuo Jian and Professor Cunlin Zhang at Department of Physics, Capital Normal University, China, for providing us with very valuable cyclic olefin polymer samples and for discussing the results of our experiments on terahertz time-domain spectroscopy.

Thanks also to Dr. Kazunori Serita, Dr. Razanoelina Manjakavahoaka (currently at Shizuoka University) and Dr. Baggsican Filchito Renee (currently at Okinawa Institute of Science and Technology) for their helpful advice on the basics of experimental equipment, operation methods and routine maintenance, and data analysis.

I also greatly appreciate the Terahertz Photonics group members: Appointed Professor Keiko Kitagishi, Technical staff Kengo Ota, PhD students Jiang Hao, Kosuke Okada, Abdul Mannan, Fumikazu Murakami, Yang Dongxun, Master students Satoshi Kobatake, Li Zhixian, Wang Ke, Tomohisa Okumura, Taiga Fukuda and research student Chen Haidong; and colleagues who have worked at THP in the past: Tomoya Takarada, Kota Yamahara, Kengo Tamura, Ryohei Taie, Keisuke Ikeda, Kazuma Konishi, Motoki Kuwano. The members of our research group who have helped me in different ways and provided solutions to numerous problems during all my work. It is a real pleasure and honor to be a part of the THP lab. Thank you and good luck my friends!

I would like to express a special word of thanks to our secretary, Mayo Iwami who helped me to weather the turmoil of settling into a new place unprecedented support, and the ritual cups of coffee after lunch. Thank you for making the atmosphere in the office so relaxed and friendly.

I also wish to thank the Ministry of Education, Culture, Sports, Science and Technology of Japan for the generous financial support and the enthusiastic help from the Student Support Affairs Section of Graduate School of Engineering, Osaka University.

Finally, I would like to thank all my family and friends; especially my mum for being eternally support.

Contents

Chapter 1. **INTRODUCTION**

1.1 TERAHERTZ SCIENCE

In the last two decades, terahertz (THz) radiation, one of the least explored regions of the electromagnetic spectrum, has attracted great interest from researchers. Typically, it is referred to as the electromagnetic waves that vibrate one trillion times per second (10^{12} Hz), which sandwiched between the infrared (IR) and microwave frequencies and has been believed as the most undeveloped region of the electromagnetic spectrum traditionally called as the "THz gap" [1]. Due to the lack of bright coherent sources and effective detection techniques, science at THz frequencies has not been fully understood, and the applications have remained undeveloped for a long time in history. With the development of ultrafast laser technology, scientists have made remarkable achievements in the tabletop THz pulse sources based on ultrafast laser pulses down-conversion for many decades. Nowadays, THz radiation has become increasingly relevant to the most diverse fields, such as medical imaging, industrial detection, remote sensing, and basic science [2,3].

The attraction of THz radiation lies in its properties. First, THz waves have X-ray-like penetrating ability. Dielectric materials such as paper, plastic, cloth, wood and ceramics are usually opaque at optical wavelengths but transparent at THz frequencies. This property is useful for practical THz imaging and sensing to nondestructive inspect sealed packages where hydrated and metallic materials can be separated from other materials [4,5]. Second, because the energy levels of many biomolecular interactions fall in the THz band, they are able to exhibit strong absorption and resonance in this band [6]. In particular, THz waves are extremely sensitive to biological water content and can be an important tool in the study of water distribution in living organisms as spectroscopic fingerprinting [7]. Additionally, THz waves have the advantage of higher safety for biomedical imaging and human body security inspection equipment because their low photon energy (4.1 meV for 1 THz) does not cause photodissociation of biological tissues [8,9]. Besides these, THz radiation is also applied in basic scientific research area to reveal some ultrafast light-matter interaction such as carrier dynamics in semiconductors [10–12], nanostructures [13–16], and superconductors [17,18], etc.

As a key tool for studying ultrafast phenomena, THz time-resolved pump-probe techniques take advantage of short, intense ultrafast laser-material interaction to excite ionization, transient photocurrents, birefringence and lattice vibrations. These THz spectra can be obtained with optical pump/THz probe, THz pump/THz probe, or THz pump/optical probe measurements. In these setups, the time resolution is achieved by finely controlling the relative time delay between the pump and probe beam. The time resolution of this technique is typically on the femtosecond scale, depending on the pump and probe pulse durations.

1.2 ULTRAFAST LASER-BASED TECHNIQUES FOR THZ PULSE GENERATION AND DETECTION

Notable progress has been made in developing tabletop THz pulse sources by utilizing mode-locked oscillator emitted IR laser pulses. As two widely used examples, THz pulses are emitted by using transient photocurrent in photoconductive antennas (PCAs) or optical rectification (OR) effect in nonlinear crystals via frequency down-conversion. Being pumped by ultrashort (typically <100 fs) laser pulses, the generated THz pulses are very short (~1 ps) approaching a near half-cycle oscillation.

The PCA composed of two micron-sized metal electrodes deposited on a semiconductor substrate, usually low-temperature-grown GaAs (LT-GaAs). As shown in Fig. 1.1(a), IR laser pulses whose photon energy higher than the semiconductor energy bandgap illuminate the center area of two electrodes and excite free carriers. These ultrafast carriers (electrons and holes) are then accelerated by an external bias field, and produce a current surge. As the photocurrent varies with time, it emits THz radiation in the far-field [19,20]. In contrast, photoconductive sampling is the inverse process of emission mechanism. The unbiased PCA is placed in the optical path. By measuring the transient currents between electrodes driven by THz field shown in Fig. 1.1(b), the THz waveform can be sampled in the time domain by delaying the THz pulse relative to the optical probe pulse.

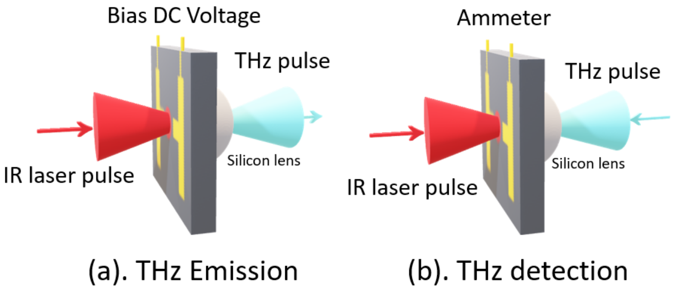

Figure 1.1 Schematic diagram THz pulse generation (a) and detection (b) by using the photoconductive antenna.

The OR process is a second-order nonlinear effect in which quasi-DC polarization is induced by an ultrashort pulse propagating through non-centrosymmetric crystals such as ZnTe, GaP, and GaSe. The nonlinear optical interactions can be described in terms of a nonlinear polarization given by $P^{(2)} = 2\varepsilon_0\chi^{(2)}|E_0(t)|^2$ [21], here $E_0(t)$ is the time dependent optical beam electric field, and $\chi^{(2)}$ is the second order nonlinear optical susceptibility. If the OR process is within the laser pulse width rather than continuous, the rectified nonlinear polarization will be a time-varying function associated with the pulse envelope (Fig. 1.2(a)). When the optical pulse duration is in a picosecond or sub-picosecond level, the radiation frequency is within THz range [22].

THz detection process in nonlinear crystals is known as electro-optic (EO) sampling. By co-focusing the femtosecond laser pulses with THz pulses in the detection crystal, the Pockels effect induces birefringence proportional to the THz field amplitude (Fig. 1.2(b)), causes an anisotropic change in the refractive index of the crystal and affects the polarization state of the probe pulse. By tracking the relative changes in the two orthogonal polarization components of the probe beam transmitted through the detection crystal, one can directly measure not only the amplitude, but also the phase with high precision ($< 10^{-2}$ rad) [23].

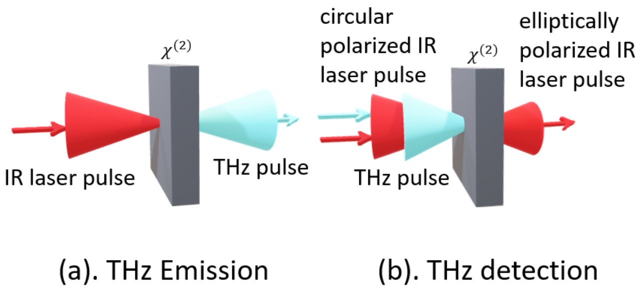

Figure 1.2 THz generation (a) and detection (b) by IR laser pulse in a nonlinear crystal via optical rectification and Pockels effect.

It is important to note that although solid-state based THz emitters and detectors can provide theoretically optimal bandwidths, the THz spectra in practice are always affected by the degradation associated with the absorptive nature of the solid materials. For the example of PCA, the emitted THz power and bandwidth strongly depend on the electrodes structure, bias voltage and the IR pump power. THz field amplitude increases linearly with weak bias fields and low energy pumping. However, a high bias voltage may lead to the breakdown of the substrate material, and the THz radiation output power saturates due to the screening effect of photoexcited carriers on the bias field as the pump power reaches a certain level. Also, the phonon modes in PCA semiconductor substrates limit the rise time (and corresponding THz pulse bandwidth) of the photocurrent to the carrier-phonon scattering time (several hundred femtoseconds) [20,24].

For nonlinear crystals, THz output bandwidths are limited by the nonlinearity induced dispersion, the phase-matching condition between the pump pulse group velocity and the emitted THz phase velocity, and the phonon mode absorptions. For ZnTe and GaP, they have TO phonon resonance modes at 5.3 THz and 10.98 THz, respectively [25–27]. To limit the THz pulse absorption and dispersion in the crystal and to achieve wide bandwidth detection, thinner crystals are usually considered, but sensitivity is also reduced [28].

1.3 THZ EMISSION FROM TWO-COLOR LASER INDUCED FILAMENTATION

Such sources mentioned above can provide THz electric fields on the order of kV/cm. But in response to the demand for explorations for novel nonlinear effect in a variety of materials, there is an urgent need to develop more efficient, broadband and coherent THz sources that will enable new research and applications. Intense THz pulses can trigger ultrafast electromagnetic field switching operations on time scales of tens of femtoseconds to picoseconds, which is much faster than conventional electronic devices. Great efforts have been made to improve the two methods based on PCA and OR, and strong THz sources have been developed such as large-aperture photoconductive antennas (LAPCA) [29], inorganic EO crystals $LiNbO_3$ [30] and organic crystals 4-N-methylstilbazolium tosylate (DAST) [31]. However, they still have the problems of laser damage threshold, thermal and multiphoton effects that exist in solid materials themselves.

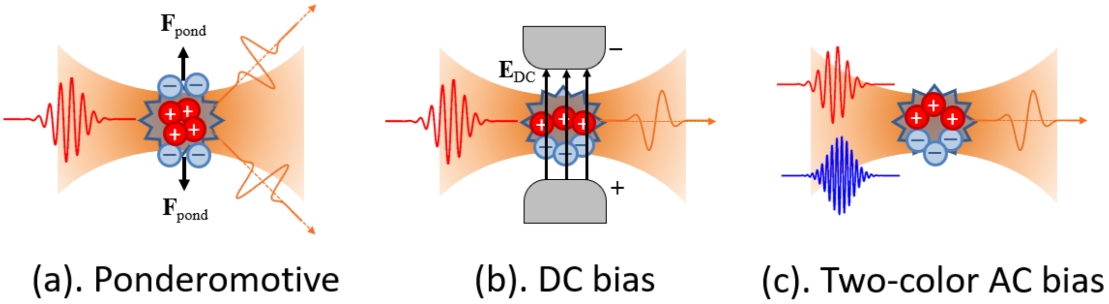

(a). Ponderomotive (b). DC bias (c). Two-color AC bias

Figure 1.3 Air plasma radiated THz mechanism based on (a) electrons are drifted away by ponderomotive force, (b) external DC source, and (c) two-color mixed field.

In addition to using solid materials, gaseous media which can be ionized by an intense laser pulse to form a laser filament are considered as a novel broadband coherent THz source. This scheme not only eliminates the worry about the laser damage threshold, but also the THz emission process is not affected by the absorption and dispersion inside the solid matters. The historical development of this method proceeds as follows. In the first demonstration by Hamster et al., femtosecond laser pulses with energies up to 50 mJ were focused to ionize gas molecules and emit THz pulses [32,33]. As shown in Fig. 1.3(a), these transient electric field radiations were associated with ponderomotive forces that only accelerated the electrons and expelled them from the focus, while the inertia of the positive ions prevented them from moving during the duration of the ultrashort laser pulse, resulting in intense and broadband THz radiation.

Subsequently, Löffler et al. increased the amplitude of the coherent THz pulse by applying a DC bias voltage at the focus and perpendicular to the laser propagation direction to accelerate the electrons of the plasma (Fig. 1.3(b)) [34,35]. However, the electric breakdown limits the further expansion of the THz field. Fig. 1.3(c) shows an alternative method of generating stronger THz fields based on a combination of two-color laser pulses proposed by Cook et al. [36]. With an intense IR pulse (ω) emitted from a regenerative amplified Ti:Sapphire laser system, its second harmonic (2ω) is frequency-converted by a nonlinear crystal such as type-I β-BaB_2O_4 (BBO) for 800 nm laser. They are co-focused by a lens or an off-axis parabolic mirror to ionize the air. Similar to the external DC field method, the two-color field accelerates the electrons in the plasma and emit intense THz pulses, but the THz yield efficiency increases by 40 times compared to monochromatic techniques. Also, the THz generation process is sensitive to two-color field phase difference which can be adjusted by modulating the dispersion of air or inserting a phase-shifted glass plate.

Two-color laser filament method is popular for its relatively simple experimental implementation, fairly high conversion efficiency, and wide spectral coverage. Matsubara et al. produced ultra-broadband electromagnetic pulses up to the 200 THz range using plasmas induced by 10-fs pulses focused with their second harmonics [37]. Yoo et al. obtained maximum THz energy of 2.6 μJ with a 200 fs IR pulse pump by refocusing the spot size to 43 μm, which provides a maximum THz field strength of about 16 MV/cm at a 1 kHz repetition rate [38]. Such ultrafast THz pulses with very high peak intensities have recently emerged as powerful tools to directly control the strongly correlated electron systems or complex condensed-matter systems. Many applications have been stimulated in strong-field matter interaction studies like the field-free orientation of rotationally excited molecules [39], atomic structure coherent modulation [40] and coherent phonon excitation [40], based on this promising intense THz source.

1.4 MECHANISM OF THZ EMISSION FROM TWO-COLOR FILAMENTS AND ITS LIMITATIONS

To explain the THz generation mechanism in a two-color laser filament, two different models have been proposed historically: four-wave mixing (FWM) model based on the third-order nonlinearity $\chi^{(3)}$ [36,41,42], and a photocurrent (PC) model based on the symmetry-breaking electron drift motion [43–45]. The two models correspond to the bound and free electrons induced nonlinear polarizations respectively. The common point of the two models is the two-color phase matching condition for the effective THz radiation, expressed as

$$E_{\mathrm{THz,FWM}} \propto \chi^{(3)} |E_{2\omega} E_{\omega} E_{\omega}| \cos\theta, \tag{1.1}$$

$$E_{\mathrm{THz,PC}} \propto f(E_\omega) E_{2\omega} \sin\theta, \tag{1.2}$$

where E_ω and $E_{2\omega}$ are the amplitudes of the ω and 2ω electric fields respectively, θ is the relative phase between two-color fields, $\chi^{(3)}$ is the third-order nonlinear optical susceptibility, and $f(E_\omega)$ is a function dependent on the fundamental electric field E_ω. Eqs (1.1) and (1.2) are the two most commonly used scaling laws to describe the filament THz emission process and have explained some experimental observations.

However, the nonlinear effect introduced by high intensity on the THz emission characteristics has rarely been studied in depth. Strong photoionization induced by the high intensity ($10^{12} \sim 10^{14}$ W/cm^2) at the focal center leads to a huge number of free electrons, in which laser pulses undergoes a series of focus-defocus cycles consisting of the optical Kerr effect and plasma defocusing. These complex nonlinearities lead to a macroscopic ionization trajectory, which is known as laser filamentation, also trigger complicate modulation on the laser pulses. One of the better-known examples is the white light generation during self-focusing of ultrashort lasers [46,47]. At sufficiently high input intensities, the infrared filament emission pulse spectrum appears blueshift capable of covering the UV region, which can be explained by the temporal distortion of the laser pulse due to the dispersion of the intensity-dependent refractive index. Specifically, the additional phase caused by the interaction of the high-intensity electromagnetic field with the nonlinear response of bound and free carriers during the filamentation process is known as self-phase modulation (SPM). The same mechanism also introduces a phase modulation to the 2ω field, called cross-phase modulation (XPM). These modulation effects destroy the phase-matching conditions of the two THz emission models mentioned earlier, resulting in reduced outgoing efficiency, waveform shaping, etc. When using an air plasma THz source for the corresponding study of nonlinearities in the matter, the intensity-induced modulation may be mistaken for a property of the matter itself. Therefore, it is crucial to investigate the effect of laser intensity-induced self-modulation effects on the THz emission mechanism.

1.5 SUMMARY OF DISSERTATION

This thesis focuses on the THz radiation mechanism via the filament formation process in air with two-color laser pulses. The main argument is on the role of the relative phase of the two-color field which modulates the emitted THz energy and waveform. This work is divided into the following sections:

Chapter 2 reviews the basics of the principle of photoionization, laser filamentation, and THz emission of focused two-color laser pulses. General concepts, photocurrent models and regulation parameters are introduced. The air-based broad-spectrum THz detection method is also presented at the end of the chapter.

Chapter 3 presents the results of our experimental observation on the modulation of THz emission energy by varying incident IR pump energy. We attribute the phenomena to the additional phase of the two-color laser modulated by the incident IR pulse energy to the refractive index change due to the intensity-dependent electron density in the filament, which also contributes to the spectral spread of the two-color pulses. The additional phase leading to a shift in the optimal THz emission position is in good agreement with the spectral spread of the two-color light after passing through the filament, confirming our point.

Chapter 4 introduces the results of the THz emission waveform modulation by different incident powers. We recorded the THz waveform evolution for the input IR pump energy varied from 1.75 ~ 2.75 mJ by the ABCD method, which features low absorption and dispersion due to solid materials. The experimental results show that the amplitude ratio of positive and negative peaks of the bipolar THz waveform increasing with the pump pulse energy, and the slow-varying peaks at the tail gradually disappear. This phenomenon is explained by the modified photocurrent model based on the macroscopic coherent emission mechanism. As in Chapter 3, this modulation is caused by the additional phase induced by the plasma. High plasma density at the focal center causes a π phase slip between the two-color fields, resulting in a bipolar THz waveform. And weak photoionization near the front of the focus gradually affect the initial phase as the pumping energy increases. Based on these, we calculated the positive-negative peak ratio which fits our observation with a good agreement. In addition, the smoothed peak in the tail is considered to be caused by the fading out of the residual current after the negative peak.

Chapter 5 shows an application example of the two-color laser filament THz-TDS system. Optical characteristics of a variety of amorphous materials with potential applications in the THz band have been obtained by an intense THz beam emitted by a two-color filament and a weak beam emitted by a PCA source, respectively. Among them, the cyclic olefin polymer (COP) material shows a low absorption coefficient and a low dispersion in the broadband range. And it shows little nonlinear responses under strong THz pumping, revealing its potential for application in THz lens, cuvettes and broadband transmission line substrates.

Chapter 6 concludes this thesis by reviewing our works. We emphasize the importance of this dissertation for the theory and experiment of THz emission from two-color laser filaments. An outlook for future work is also provided.

REFERENCES:

1. Y. S. Lee, *Principles of Terahertz Science and Technology* (Springer US, 2009).
2. B. Ferguson and X. Zhang, "Materials for terahertz science and technology," Nat. Mater. **1**, 26–33 (2002).
3. M. Tonouchi, "Cutting-edge terahertz technology," Nat. Photonics **1**, 97–105 (2007).
4. B. B. Hu and M. C. Nuss, "Imaging with terahertz waves," Opt. Lett. **20**, 1716 (1995).
5. K. Kawase, Y. Ogawa, Y. Watanabe, and H. Inoue, "Non-destructive terahertz imaging of illicit drugs using spectral fingerprints," Opt. Express **11**, 2549 (2003).
6. H. Elgabarty, T. Kampfrath, D. J. Bonthuis, V. Balos, N. K. Kaliannan, P. Loche, R. R. Netz, M. Wolf, T. D. Kühne, and M. Sajadi, "Energy transfer within the hydrogen bonding network of water following resonant terahertz excitation," Sci. Adv. **6**, 1–9 (2020).
7. W. Shi, Y. Wang, L. Hou, C. Ma, L. Yang, C. Dong, Z. Wang, H. Wang, J. Guo, S. Xu, and J. Li, "Detection of living cervical cancer cells by transient terahertz spectroscopy," J. Biophotonics **14**, 1–7 (2021).
8. L. Yu, L. Hao, T. Meiqiong, H. Jiaoqi, L. Wei, D. Jinying, C. Xueping, F. Weiling, and Z. Yang, "The medical application of terahertz technology in non-invasive detection of cells and tissues: opportunities and challenges," RSC Adv. **9**, 9354–9363 (2019).
9. O. P. Cherkasova, D. S. Serdyukov, A. S. Ratushnyak, E. F. Nemova, E. N. Kozlov, Y. V. Shidlovskii, K. I. Zaytsev, and V. V. Tuchin, "Effects of Terahertz Radiation on Living Cells: a Review," Opt. Spectrosc. **128**, 855–866 (2020).
10. H. C. Guo, X. H. Zhang, W. Liu, A. M. Yong, and S. H. Tang, "Terahertz carrier dynamics and dielectric properties of GaN epilayers with different carrier concentrations," J. Appl. Phys. **106**, (2009).
11. T. Wang, M. Zalkovskij, K. Iwaszczuk, A. V. Lavrinenko, G. V. Naik, J. Kim, A. Boltasseva, and P. U. Jepsen, "Ultrabroadband terahertz conductivity of highly doped ZnO and ITO," Opt. Mater. Express **5**, 566 (2015).
12. H. Jiang, C. Gong, T. Nishimura, H. Murakami, I. Kawayama, H. Nakanishi, and M. Tonouchi, "Terahertz Emission Spectroscopy and Microscopy on Ultrawide Bandgap Semiconductor β-Ga_2O_3," Photonics **7**, 73 (2020).
13. J. Lloyd-Hughes and T. I. Jeon, "A review of the terahertz conductivity of bulk and nano-materials," J. Infrared, Millimeter, Terahertz Waves **33**, 871–925 (2012).
14. Y. Zhang, Y. Zhao, S. Liang, B. Zhang, L. Wang, T. Zhou, W. Kou, F. Lan, H. Zeng, J. Han, Z. Feng, Q. Chen, P. Mazumder, and Z. Yang, "Large phase modulation of THz wave via an enhanced resonant active HEMT metasurface," Nanophotonics **8**, 153–170 (2018).

15. P. Bowlan, E. Martinez-Moreno, K. Reimann, T. Elsaesser, and M. Woerner, "Ultrafast terahertz response of multilayer graphene in the nonperturbative regime," Phys. Rev. B - Condens. Matter Mater. Phys. **89**, 1–5 (2014).

16. P. Bowlan, J. Bowlan, S. A. Trugman, R. Valdés Aguilar, J. Qi, X. Liu, J. Furdyna, M. Dobrowolska, A. J. Taylor, D. A. Yarotski, and R. P. Prasankumar, "Probing and controlling terahertz-driven structural dynamics with surface sensitivity," Optica **4**, 383 (2017).

17. K. Katsumi, N. Tsuji, Y. I. Hamada, R. Matsunaga, J. Schneeloch, R. D. Zhong, G. D. Gu, H. Aoki, Y. Gallais, and R. Shimano, "Higgs Mode in the d -Wave Superconductor $Bi_2Sr_2CaCu_2$ O_{8+x} Driven by an Intense Terahertz Pulse," Phys. Rev. Lett. **120**, 117001 (2018).

18. R. Matsunaga, N. Tsuji, K. Makise, H. Terai, H. Aoki, and R. Shimano, "Polarization-resolved terahertz third-harmonic generation in a single-crystal superconductor NbN: Dominance of the Higgs mode beyond the BCS approximation," Phys. Rev. B **96**, 2–6 (2017).

19. M. Van Exter, C. Fattinger, and D. Grischkowsky, "High-brightness terahertz beams characterized with an ultrafast detector," Appl. Phys. Lett. **55**, 337–339 (1989).

20. D. H. Auston, K. P. Cheung, and P. R. Smith, "Picosecond photoconducting Hertzian dipoles," Appl. Phys. Lett. **45**, 284–286 (1984).

21. R. Boyd, *Nonlinear Optics* (Academic Press, 2008).

22. X. C. Zhang, X. F. Ma, Y. Jin, T. M. Lu, E. P. Boden, P. D. Phelps, K. R. Stewart, and C. P. Yakymyshyn, "Terahertz optical rectification from a nonlinear organic crystal," Appl. Phys. Lett. **61**, 3080–3082 (1992).

23. Q. Wu and X. C. Zhang, "Free-space electro-optic sampling of terahertz beams," Appl. Phys. Lett. **67**, 3523 (1995).

24. M. Tani, S. Matsuura, K. Sakai, and S. Nakashima, "Emission characteristics of photoconductive antennas based on low-temperature-grown GaAs and semi-insulating GaAs," Appl. Opt. **36**, 7853 (1997).

25. O. Hatem, "Peak emission of terahertz waves from (110)-oriented ZnTe by interacting phase-matched phonon resonances," J. Opt. Soc. Am. B **36**, 1144 (2019).

26. I. D. Vugmeyster, J. F. Whitaker, and R. Merlin, "GaP based terahertz time-domain spectrometer optimized for the 5-8 THz range," Appl. Phys. Lett. **101**, (2012).

27. Q. Wu and X. C. Zhang, "7 terahertz broadband GaP electro-optic sensor," Appl. Phys. Lett. **70**, 1784–1786 (1997).

28. A. Leitenstorfer, S. Hunsche, J. Shah, M. C. Nuss, and W. H. Knox, "Detectors and sources for ultrabroadband electro-optic sampling: Experiment and theory," Appl. Phys. Lett. **74**, 1516–1518 (1999).
29. X. Ropagnol, M. Khorasaninejad, M. Raeiszadeh, S. Safavi-Naeini, M. Bouvier, C. Y. Côté, A. Laramée, M. Reid, M. A. Gauthier, and T. Ozaki, "Intense THz Pulses with large ponderomotive potential generated from large aperture photoconductive antennas," Opt. Express **24**, 11299 (2016).
30. H. Hirori, A. Doi, F. Blanchard, and K. Tanaka, "Single-cycle terahertz pulses with amplitudes exceeding 1 MV/cm generated by optical rectification in $LiNbO_3$," Appl. Phys. Lett. **98**, 091106 (2011).
31. C. P. Hauri, C. Ruchert, C. Vicario, and F. Ardana, "Strong-field single-cycle THz pulses generated in an organic crystal," Appl. Phys. Lett. **99**, 161116 (2011).
32. H. Hamster, A. Sullivan, S. Gordon, W. White, and R. W. Falcone, "Subpicosecond, electromagnetic pulses from intense laser-plasma interaction," Phys. Rev. Lett. **71**, 2725–2728 (1993).
33. H. Hamster, A. Sullivan, S. Gordon, and R. W. Falcone, "Short-pulse terahertz radiation from high-intensity-laser-produced plasmas," Phys. Rev. E **49**, 671–677 (1994).
34. T. Löffler, F. Jacob, and H. G. Roskos, "Generation of terahertz pulses by photoionization of electrically biased air," Appl. Phys. Lett. **77**, 453 (2000).
35. T. Löffler and H. G. Roskos, "Gas-pressure dependence of terahertz-pulse generation in a laser-generated nitrogen plasma," J. Appl. Phys. **91**, 2611–2614 (2002).
36. D. J. Cook and R. M. Hochstrasser, "Intense terahertz pulses by four-wave rectification in air," Opt. Lett. **25**, 1210 (2000).
37. E. Matsubara, M. Nagai, and M. Ashida, "Ultrabroadband coherent electric field from far infrared to 200 THz using air plasma induced by 10 fs pulses," Appl. Phys. Lett. **101**, 011105 (2012).
38. Y. J. Yoo, D. Kuk, Z. Zhong, and K. Y. Kim, "Generation and Characterization of Strong Terahertz Fields from kHz Laser Filamentation," IEEE J. Sel. Top. Quantum Electron. **23**, (2017).
39. K. N. Egodapitiya, S. Li, and R. R. Jones, "Terahertz-Induced Field-Free Orientation of Rotationally Excited Molecules," Phys. Rev. Lett. **112**, 103002 (2014).
40. A. A. Melnikov, K. N. Boldyrev, Y. G. Selivanov, V. P. Martovitskii, S. V. Chekalin, and E. A. Ryabov, "Coherent phonons in a Bi 2 Se 3 film generated by an intense single-cycle THz pulse," Phys. Rev. B **97**, 214304 (2018).

41. M. Kress, T. Löffler, S. Eden, M. Thomson, and H. G. Roskos, "Terahertz-pulse generation by photoionization of air with laser pulses composed of both fundamental and second-harmonic waves," Opt. Lett. **29**, 1120 (2004).

42. X. Xie, J. Dai, and X.-C. Zhang, "Coherent Control of THz Wave Generation in Ambient Air," Phys. Rev. Lett. **96**, 075005 (2006).

43. K.-Y. Kim, J. H. Glownia, A. J. Taylor, and G. Rodriguez, "Terahertz emission from ultrafast ionizing air in symmetry-broken laser fields," Opt. Express **15**, 4577 (2007).

44. K. Y. Kim, A. J. Taylor, J. H. Glownia, and G. Rodriguez, "Coherent control of terahertz supercontinuum generation in ultrafast laser–gas interactions," Nat. Photonics **2**, 605–609 (2008).

45. K.-Y. Kim, "Generation of coherent terahertz radiation in ultrafast laser-gas interactions," Phys. Plasmas **16**, 056706 (2009).

46. A. L. Gaeta, "Catastrophic collapse of ultrashort pulses," Phys. Rev. Lett. **84**, 3582–3585 (2000).

47. N. Aközbek, M. Scalora, C. M. Bowden, and S. L. Chin, "White-light continuum generation and filamentation during the propagation of ultra-short laser pulses in air," Opt. Commun. **191**, 353–362 (2001).

Chapter 2. **THEORY OF THZ GENERATION MECHANISM FROM TWO-COLOR LASER FILAMENT**

2.1 PHOTOIONIZATION

High energy laser beam illuminated on a target (solid, liquid or gas medium) can form ions and release free electrons from their parent atoms or molecules, which is called as photoionization. For a laser with a central wavelength of 800 nm, its photon energy (~1.5 eV) is too small in relation to the ionization potential (U_i ~ 12 eV for oxygen) to meet the ionization energy requirements in air. However, when the focusing induced by the lens or photonic Kerr effect collapses the beam, the huge intensity increase at the focal point makes the photoionization process possible.

Keldysh developed a theory to describe the photoionization process of a single-electron atom in an intense oscillating electric field [1]. He introduced a dimensionless parameter to characterize photoionization, which can be defined as [2]

$$\gamma = \frac{\omega_0}{eE}\sqrt{2mU_i} = \sqrt{U_i/2U_p}. \tag{2.1}$$

Here U_i is the ionization potential of the atom and U_p is the laser ponderomotive potential. Generally, the "ponderomotive" refers to the cycle-averaged quiver motion of charged particles in response to an applied electromagnetic field [3], so that the Keldysh parameter can be understood as a ratio between the energy required for an electron to be freed and its kinetic energy acquired within one cycle of the laser field. For $\gamma \gg 1$, the ionization potential is much higher than the ponderomotive potential. For this case, several photons with energies below the ionization threshold may combine their energies to excite and release the bound electrons (see Fig. 2.1 (a)). This ionization mechanism is called multiphoton ionization (MPI) and occurs when the laser intensity is below ~10^{12} W/cm^2 with a wavelength of 800 nm. For $\gamma < 1$, the ionization potential is lower than the ponderomotive potential. The Coulomb barrier is instantaneously suppressed by the laser electric field, results in the relatively low and narrow barrier between the bound state and the remaining continuous state, which allows the bound electrons to tunnel out from the atom (see Fig. 2.1 (b)) [4,5]. This ionization mechanism is called tunnel ionization (TI) which occurs when the laser intensity approaches 10^{13} W/cm^2. The photoionization process releases a large number of free electrons, resulting in the complicate propagation process of laser in a medium accompanied by many unique phenomena.

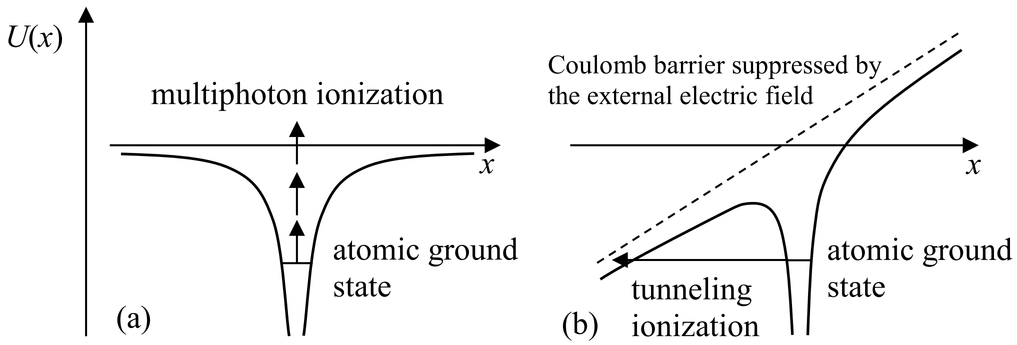

Figure 2.1 Two processes of photoionization. (a) Multiphoton ionization. (b) Tunnel ionization.

2.2 NONLINEAR PROPAGATION OF INTENSE LASER PULSES

A better-known example is the so-called filamentation, which is generally considered to be the result of the balance of multiple nonlinear effects driven by a strong electric field. In this section, we explore the origin of these nonlinearities starting from the basic electromagnetic wave propagation theory. The propagation of a laser pulse in a material medium is dominated by Maxwell equations:

$$\nabla \cdot \mathbf{D} = \rho, \tag{2.2}$$

$$\nabla \times \mathbf{E} = -\frac{\partial \mathbf{B}}{\partial \mathrm{t}}, \tag{2.3}$$

$$\nabla \cdot \mathbf{B} = 0, \tag{2.4}$$

$$\nabla \times \mathbf{H} = \mathbf{J} + \frac{\partial \mathbf{D}}{\partial \mathrm{t}}. \tag{2.5}$$

Here, $\mathbf{D} = \varepsilon_0 \mathbf{E} + \mathbf{P}$ is the dielectric displacement, $\mathbf{P}$ is the overall average dipole moments induced by the laser field, which can be decomposed as linear and non-linear components:

$$\mathbf{P} = \mathbf{P}^{(1)} + \mathbf{P}_{\mathrm{NL}}, \tag{2.6}$$

where the first term $\mathbf{P}^{(1)}$ varies linearly with the electric field and describes the classical linear optical phenomena; the second term $\mathbf{P}_{\mathrm{NL}}$ leads to nonlinear optical effects and induces self-interactions. With the wave vector $\mathbf{k}$ which can be decomposed as $\mathbf{k} = \sqrt{k_x^2 + k_y^2 + k_z^2}$, the z-direction propagated plane wave electric field can be then regarded as $k_z > 0$ and $k_\perp = \sqrt{k_x^2 + k_y^2} \ll |k|$. From this set of equations one can obtain the standard derivation of the frequency domain wave equation [7]:

$$\frac{\partial^2 \mathbf{E}(\omega)}{\partial z^2} + [k(\omega)]^2 \mathbf{E}(\omega) + \nabla_\perp^2 \mathbf{E}(\omega) = -\mu_0 \omega^2 \left(\mathbf{P}_{\mathrm{NL}} + i \frac{\mathbf{J}(\omega)}{\omega} \right), \tag{2.7}$$

where $\nabla_{\perp}^{2} = \partial/\partial x + \partial/\partial y$ is the transversal Laplace operator. We neglect the imaginary part of the linear susceptibility and consider the wave vector $k^2(\omega) = \omega^2\varepsilon(\omega)/c^2$ with real-valued permittivity only, and assumed that the nonlinear response is isotropic and homogeneous [8]. Combined with the paraxiality assumption $\nabla \cdot \mathbf{E} \approx 0$, electric field can be decoupled as the vectoral components $\mathbf{E} = (E_x, E_y, E_z)$ in Eq. (2.7). Consider that the initial laser field is linearly polarized as $\mathbf{E} = (E_x, 0,0)$ and preserved in the paraxial regime during beam propagation. But it should be noted that the latter assumption cannot be maintained for large nonparaxialities which may lead to a complex coupling of different nonlinear polarizations [9]. With the forward propagation assumption $\mathbf{E}(\omega) = \mathbf{E}^{+}(\omega)$, Eq. (2.7) can be rewritten as a first order partial differential equation (PDE) as [10,11]

$$\frac{\partial \mathbf{E}(\omega)}{\partial \mathrm{z}} = \frac{i}{2k(\omega)}\nabla_{\perp}^{2}\mathbf{E}(\omega) + ik^2(\omega)\mathbf{E}(\omega) + \frac{i\mu_0\omega^2}{2k(\omega)}\left(\mathbf{P}_{\mathrm{NL}} + i\frac{\mathbf{J}(\omega)}{\omega}\right). \tag{2.8}$$

For the convenience of discussion, the pulse field **E** is decomposed into envelope **A** and the oscillating field at the carrier frequency ω_0:

$$\mathbf{E}(z,t) = \mathbf{A}(z,t)\exp(-i\omega_0 t)\,. \tag{2.9}$$

We note that the two nonlinearities, the third r.h.s. term in Eq. (2.8), act on the incident light pulse. We first focus on the nonlinear polarization $\mathbf{P}_{\mathrm{NL}}$. In a gaseous medium, the lowest nonlinear process allowed is of third order since only centrosymmetric field inversion exists, which can be given by [6]

$$\begin{aligned}\mathbf{P}^{(3)}(\mathbf{z},t) &= \frac{3}{8}\varepsilon_0\chi^{(3)}(-\omega_0;\omega_0,\omega_0,-\omega_0)|\mathbf{A}(\mathbf{z},t)|^2\mathbf{A}(\mathbf{z},t)\exp(-i\omega_0 t) + c.c.\\ &+\frac{1}{8}\varepsilon_0\chi^{(3)}(-3\omega_0;\omega_0,\omega_0,\omega_0)|\mathbf{A}(\mathbf{z},t)|^2\mathbf{A}(\mathbf{z},t)\exp(-i3\omega_0 t) + c.c..\end{aligned} \tag{2.10}$$

By neglecting the third-harmonic generation term, the third-order nonlinear polarization suggests a refractive index dependent on the laser intensity, known as the optical Kerr effect. This is because the sufficiently intense electromagnetic field distorts the electron distribution in the medium. Since the energy density of the electric field is proportional to the square of the electric field strength, the laser field intensity is expressed as [12]

$$I(z,t) = \varepsilon_0 c n_0 \frac{1}{T}\int_{t-T/2}^{t+T/2} E(z,t')\,\mathrm{d}t', \tag{2.11}$$

where $n_0 = n(\omega_0)$ denotes the linear refractive index at ω_0, and $T = 2\pi/\omega_0$ is averaged optical period. Consider the slowly-varying approximation of the envelope **A** defined in Eq. (2.9) for the optical carrier at ω_0, the period-averaged intensity can be written as

$$I(z,t) = \frac{1}{2}\varepsilon_0 c n_0 |\mathbf{A}(\mathbf{z},t)|^2. \tag{2.12}$$

With the third-order nonlinear polarization considered, the intensity-dependent refractive index caused by the optical Kerr effect is expressed as

$$n(I) = n_0 + n_2 I, \tag{2.13}$$

where n_2 indicates the second-order nonlinear refractive index:

$$n_2 = \frac{3}{4n_0^2\varepsilon_0 c}\chi^{(3)}. \tag{2.14}$$

Besides the optical Kerr effect induced by n_2, another important contribution to the nonlinear refractive index comes from the plasma. The dynamics of the free carriers can be formulated according to the Drude model, where the plasma is considered as a fluid. The overall collective velocity $\mathbf{v_e}$ of the electrons is considered as a response to the optical field, so that the total current density $\mathbf{J}(t) = -N_e e\mathbf{v_e}(t)$ is subject to:

$$\frac{\partial \mathbf{J}(t)}{\partial t} + \frac{\mathbf{J}(t)}{\tau_c} = \frac{N_e e^2}{m_e}\mathbf{E}(t), \tag{2.15}$$

where, e is the electron charge (1.6×10^{-19} C), m_e is the electron mass (9.11×10^{-31} kg), N_e is the electron density and τ_c is the mean time between free carrier collisions. Eq. (2.15) can be solved by Fourier transform in the frequency domain, and the free carriers contributed current density is given by

$$-\frac{\mu_0\omega}{2k(\omega)}\mathbf{J}(\omega) = \frac{1}{2k(\omega)}\left(-\frac{\omega n_0\sigma(\omega)}{c} - i\frac{\omega_0^2}{c^2 N_c(1+\nu_e^2/\omega^2)}\right)N_e\mathbf{E}(\omega), \tag{2.16}$$

where $\nu_e = 1/\tau_c$ and $N_c = \omega_0^2 m_e \varepsilon_0 / N_e^2$ is the critical free carrier density for which the plasma becomes opaque for incident pulsed electromagnetic waves with the carrier frequency ω_0 ($N_c \sim 1.7 \times 10^{21}$ cm^{-3} at 800 nm). The cross-section for the collision of free electrons is

$$\sigma(\omega) = \frac{e^2}{m_e\varepsilon_0 n_0 c\nu_e(1+\omega^2/\nu_e^2)}. \tag{2.17}$$

Then the self-generated plasma density N_e satisfies the rate equation:

$$\frac{\partial N_e}{\partial t} = w(I)(N_0 - N_e) + \frac{\sigma(\omega)}{U_i}N_e I, \tag{2.18}$$

where N_0 is the neutral gas molecule density and $w(I)$ is the laser intensity dependent ionization rate.

Despite the typical time scale associated with filamentation is about ~100 fs, the recombination of ions and electrons occurs on the much longer nanosecond time scale. Therefore, the resulting plasma can be assumed as static within the interaction with the pulse. The r.h.s. terms in Eq. (2.18) describes the contribution of photoionization and collisional ionization to the electron density, respectively. In practice, it can be considered that the laser intensity corresponds to a rather low ionization rate. Under the dilute plasma density approximation, we have $N_e \approx N_0 w(I) \ll N_0$ and $\sigma(\omega) \to 0$. Therefore Eq. (2.18) can be simplified as

$$\frac{\partial N_e}{\partial t} = w(I) N_0. \tag{2.19}$$

Then the nonlinear refractive index contributed by the free electrons can be simplified by

$$\Delta n_p = -\frac{N_e}{2n_0^2 N_c} = -\frac{N_e e^2}{2n_0^2 \omega_0^2 m_e \varepsilon_0}. \tag{2.20}$$

Similarly, plasma permittivity at non-resonant frequencies can also be derived from the oscillation equation containing the collisionless Drude model as follows [13]:

$$\varepsilon(\omega) = n^2(\omega) = 1 - \frac{\omega_p^2}{\omega^2}, \tag{2.21}$$

where $\omega_p = \sqrt{\frac{N_e e^2}{m_e \varepsilon_0}}$ is the plasma frequency which describes the oscillatory behavior of electrons in a non-equilibrium plasma subjected to Coulomb forces. The difference between the two results is that the additional wave vector due to nonlinearity in Eq. (2.7) is linearized under the approximation. In practice, for a duration of 120 fs with a central wavelength of 800 nm laser pulse induced air filament, the plasma density has been measured in the order of $10^{16}/\mathrm{cm}^3$ and gives the plasma frequency $\frac{\omega_p}{2\pi} = 3 \times 10^9\mathrm{Hz}$ [14]. This is much smaller than optical frequency ($\sim 10^{14}$ Hz). By assuming that $\omega_p \ll \omega$, we have

$$n(\omega) = n_0 + \Delta n_p = 1 - \frac{\omega_p^2}{2\omega^2}, \tag{2.22}$$

with the same form of Δn_p in Eq. (2.20).

2.3 LASER FILAMENTATION

In most cases, a transverse Gaussian TEM_{00} mode beam is often used, whose intensity $I(r, t)$ decreases radially from its center to its edges. This leads to a spatial effect i.e. the radial wave vector $k_\perp$ cannot be neglected either. Specifically, optical Kerr effect causes the refractive index to depend on $I(r, t)$ and gradually collapses the wavefront curvature to acts as a lens, which is known as self-focusing (see Fig. 2.2(a)). Self-focusing cancels diffraction when the beam exceeds the critical power [15]

$$P_{\mathrm{cr}} = 3.72\lambda_0^2/8\pi n_2 n_0, \tag{2.23}$$

where λ_0 is the central wavelength. When the center of the beam becomes intense enough to ionize gas media, plasma is generated near the collapse center, which causes the core of the beam to scatter (see Fig. 2.2(b)). Once scattered, the beam may still contain power above P_{cr} and undergo another focus-scatter cycle. The repetition sustains long-range, self-guided propagation in the form of a thin filament. As shown in Fig. 2.3, laser filament formation is therefore a highly dynamic process with periodic ionization spikes whenever the beam starts to collapse again. The repetition of these cycles depends especially on the peak power of the input pulse, and the self-guided process maintains an average filament diameter of about 100 µm over long distances in air.

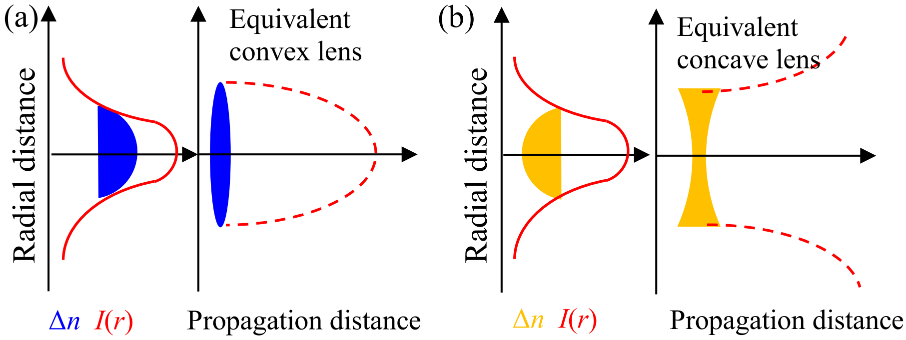

Figure 2.2 Schematic diagram of the self-focusing (a) and self-dispersion (b) effects.

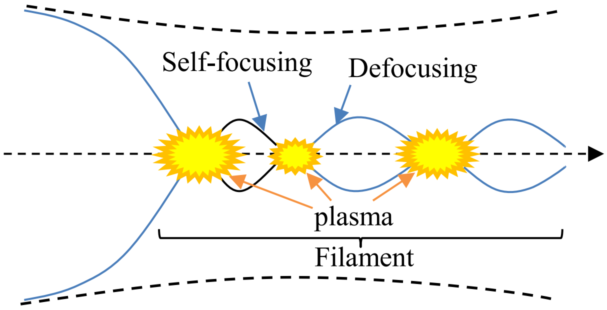

Figure 2.3 Schematic diagram of the focusing - defocusing cycles that the intense core of the beam undergoes. Solid curves denote the diameter of the intense core; Dashed curves denote the root mean square radius of the full beam.

2.4 FOUR-WAVE MIXING MODEL AND ITS LIMITATIONS

Cook et al., who first reported the mechanism of two-color filament generation, attributed the principle to four-wave mixing (rectification), a third-order nonlinear optical process induced by bound electrons of gas molecules [17]. Three photons (two at ω and one at 2ω) are mixed to produce a rectified (quasi-DC) polarization term, denoted as

$$P^{(3)} \propto \chi^{(3)} |E_\omega E_\omega E_{2\omega}| \cos(\theta), \tag{2.24}$$

where E_ω and $E_{2\omega}$ are the laser fields of fundamental and second harmonic waves, θ is the relative phase between those two fields and $\chi^{(3)}$ is the third-order nonlinear optical susceptibility.

This process is similar to the second-order OR used to explain the THz emission in nonlinear crystals. The four-wave mixing model is a phenomenological explanation based on early experimental observations. However, as the study progresses some reports suggest that the four-wave mixing model cannot explain the physical mechanism of THz radiation from two-color filaments.

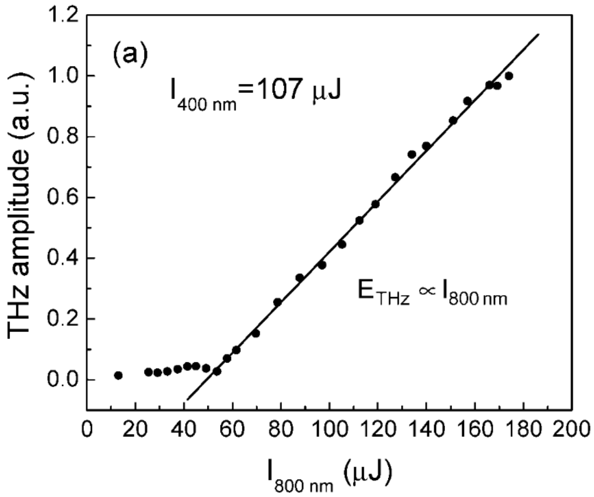

Figure 2.4 Linear relationship between emitted THz field and fundamental beam intensity at fixed intensity of second harmonic. The turning point near 50 μJ indicates the ionization threshold. (Reprinted from [18])

The third-order nonlinearity $\chi^{(3)}$ coefficient seems to be too small to explain the high conversion efficiency (10^{-4}) of THz radiation. Xie's experiment results (see Fig. 2.4) has shown that the minimum laser intensity required to generate THz radiation coincides with the threshold value for ionization [18]. Only above this threshold does the emitted THz amplitude increases linearly with the ω beam intensity. Meanwhile, they indicated that the calculated THz field is four orders of magnitude smaller than the experimentally measured field. If the $\chi^{(3)}$ contributes most of the THz emission, the scaling above and below the ionization threshold should not be by such a large difference. This implies that the THz emission originates from the contribution of free electrons.

Borodin et al. simulated the THz generation contributions from bound and free electrons and compared them with the experimentally obtained spectrum. The agreement in the 1 ~ 10 THz is the evidence for the contribution from the free carrier to the THz generation. They found that the contributions of both to the spectral components do not coincide: the free electron contribution is in the lower frequency region (center frequency lower than 5 THz), while the bound electron contribution is more concentrated in the higher frequency band (center frequency larger than 5 THz). Andreeva et al. also reveal that the FWM contribution is much weaker than free electrons current surge and it occurs at higher frequencies [19]. The FWM arises mainly from the leading edge of the self-focusing laser pulse which always sees the neutral gas and emits in the forward direction. However, the followed photoionization overwhelms the FWM contribution and emits conically.

These theoretical simulations and experimental observations point to the fact that the nonlinearity due to free electrons is the main origin of the THz emission. This was realized by Kim et al. and a novel photocurrent model based on photoionization and subsequent laser-driven currents [21-23] was proposed.

2.5 ASYMMETRIC TRANSIENT PHOTOCURRENT MODEL

The transient currents are formatted by accelerating the photoionization released free electrons with two-color combined laser field $E_\mathrm{L}(t)$ with the same polarization, which can be expressed as

$$E_\mathrm{L}(t) = A_1 \cos(\omega_1 t) + A_2 \cos(\omega_2 t + \theta), \tag{2.25}$$

where ω_1 and ω_2 are the respective wavelengths of the two-color mixed field, A_1 and A_2 are the corresponding amplitude envelopes, and θ is the relative phase between the two fields. The freed electrons ionized at t_0 can be accelerated at a time varying velocity of

$$v(t) = -\frac{e}{m_e}\int_{t_0}^{t} E_\mathrm{L}(t')\mathrm{d}t = \frac{e}{m_e}\left[\frac{A_1}{\omega_1}\sin(\omega_1 t) + \frac{A_2}{\omega_2}\sin(\omega_2 t + \theta)\right]. \tag{2.26}$$

The resulting transient electron current at time t can be expressed as

$$J(t) = \int_{-\infty}^{t} \mathrm{d}J(t') = -e\int_{-\infty}^{t} v(t')\,\mathrm{d}N_e(t')\,\mathrm{d}t'. \tag{2.27}$$

Here $\mathrm{d}N_e(t')$ is the density of free electrons released by photo-ionization at the time between $t'$and $t' + \mathrm{d}t'$, which can be obtained from the following equation:

$$\mathrm{d}N_e(t) = [N_0 - N_e(t)]w(t)\mathrm{d}t \approx N_0 w(t)\mathrm{d}t, \tag{2.28}$$

where $w(t)$ is the ionization rate or the ionization probability in unit time. Similar as section 2.2, we have $[N_0 - N_e(t)]w(t) \approx N_0 w(t)$ under the dilute plasma density approximation and electron density does not drop immediately after the electric field disappears with the nanosecond time scale of electron-ion recombination [20,21]. The accumulation of net current per optical cycle forms a long period of quasi-DC surge over the pulse width. Thus, the electromagnetic waves radiated from the laser filament is proportional to the derivative of quasi-DC density as

$$E_\mathrm{THz}(t) \propto \mathrm{d}J_\mathrm{DC}(t)/\mathrm{d}t. \tag{2.29}$$

2.6 PARAMETERS AFFECTING THZ EMISSION EFFICIENCY

2.6.1 *Incident laser intensity*

According to the above description, the degree of time variation of the quasi-DC surge current determines the electric field strength at THz. Eq. (2.27). shows that the current variation is related to the increment of the electron density per unit time and acceleration obtained from the mixed field. They are actually all related to the incident laser intensity: stronger laser intensity provides greater acceleration for the free electrons and also ionizes more free electrons per unit of time. The dependence of the free electron density on the incident laser intensity has been confirmed by the experimental results of Talebpour et al. (see Fig. 2.5) [22]. The THz yield is increased with IR pumping energy without considering the THz absorption and other nonlinear effects as transport, space charge, or re-scattering effects included (see Fig. 2.6(b)) [23].

2.6.2 *Gas species and pressure*

Gas species and pressures will also affect the THz output. The far field THz pulse energy for various two-color laser ionized gases (helium, nitrogen, air, argon and krypton) measured by a pyroelectric detector shown the trend that increases as the radius or equivalent radius of these gas molecules [23], corresponding to the increased tunnel ionization potential. In Fig. 2.5, the ionization rate of argon is slightly higher than that of nitrogen, which is also consistent with the observations in Fig. 2.6(a). The neutral gas density that increases with the gas pressure also provides a higher density of free electrons, thereby increasing the transient current to generate a stronger THz electric field. It should be noted that laboratory ambient air containing water vapor which resonantly absorbs part of the generated THz emission. In practice, pure nitrogen atmosphere has a higher THz yield than air, although oxygen (20% of air) has higher ionization rate than nitrogen (see Fig. 2.6(a)).

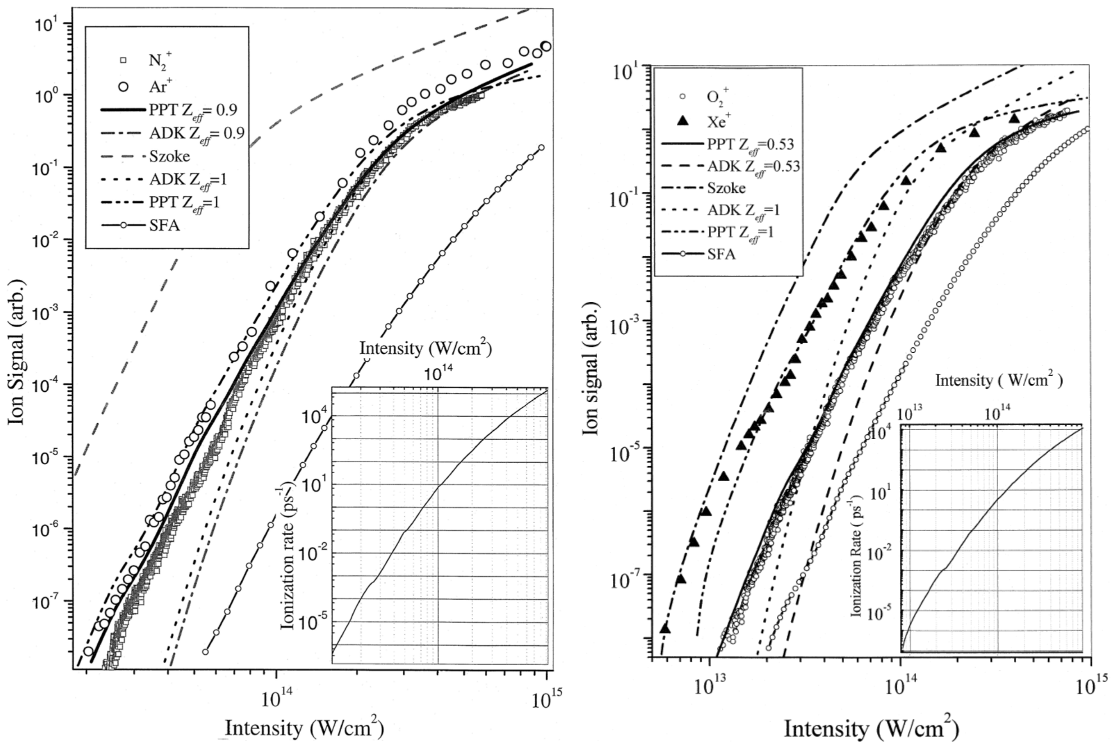

Figure 2.5 The symbols indicate the experimental ion vs. intensity of N_2 (left, square), Ar (left, big circle), O_2 (right, small circle) and Xe (right, triangle) obtained by linearly polarized 800 nm laser pulses; The curves correspond ionization rates predicted by theoretical models with different effective charge Z_{eff}.(Reprinted from [22])

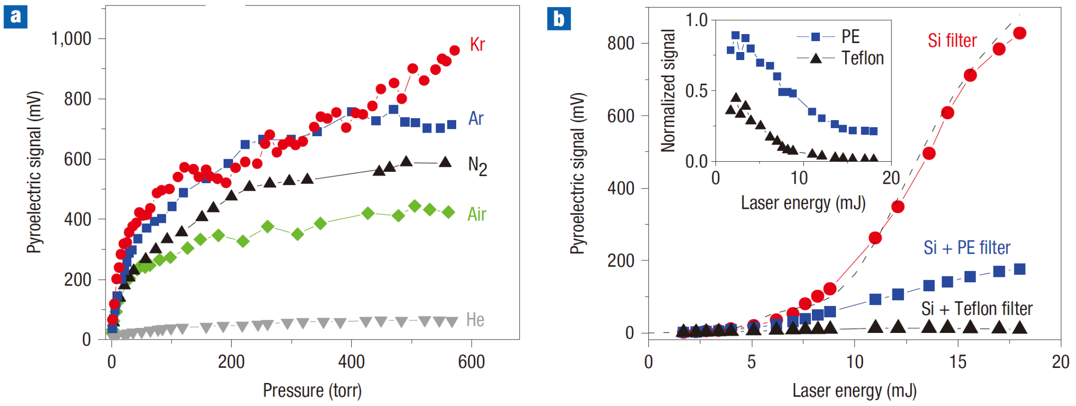

Figure 2.6 THz intensity measured by a pyroelectric detector. (a) THz intensity vs. gas pressure for various gas species; (b) THz intensity vs. IR pump power for two-color laser filament emission excited by argon at 580 Torr. Use 3 mm thick silicon, 1 mm thick PE or 3 mm thick PTFE as optical filters. THz intensity is detected by a pyroelectric detector. (Reprinted from [23])

2.6.3 *Two-color phase difference*

Numerous experimental results in the past have shown that the phase difference of two-color fields subject to air dispersion or artificially added by an in-line phase compensator modulates the THz emission intensity [23–25]. The PC model also revealed the origin of the relationship between two-color phase difference with THz yield. For $\theta = 0$, the phase dependence of electron density around the peak is symmetric, but that of drift velocity is anti-symmetric. The current surge shown in the grey area of Fig. 2.7(a) yields zero. For $\theta = \pi/2$, the electron density peaks when the drift velocity is nonzero, due to the asymmetry of the electric field around the peak. The gray area in Fig. 2.7(b) indicates that more electrons travel in the negative direction, resulting in a directional current. This directional current surge produces THz radiation in the far-field. [26]. It also predicts that the THz output has a sin(θ) dependence, i.e., the maximum occurs with a $\theta = \pi/2$ phase slippage between ω and 2ω fields [27].

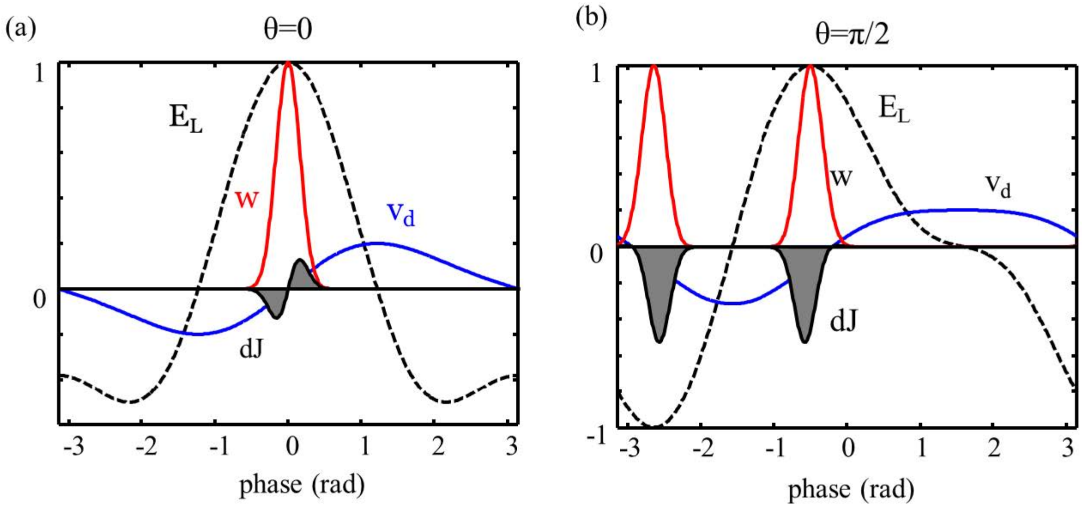

Figure 2.7 Drift velocity (blue curves) of freed electrons in a two-color field (dotted lines) for two different relative phases (a) $\theta = 0$ and (b) $\theta = \pi/2$. Time-dependent ionization rates are shown in red solid curves. The gray areas indicate the product of electron density and drift velocity.

We have also confirmed this dependence through simple theoretical calculations. As shown in Fig. 2.8(a), we calculated the cumulative current intensity for a pulse width of 100 fs according to Eq. (2.27), where the ionization rate model of the electron density is described by the power law of multiphoton absorption [16]. The net current maximum value of each phase difference fits the sinusoidal function dependence perfectly (see Fig. 2.8(b)).

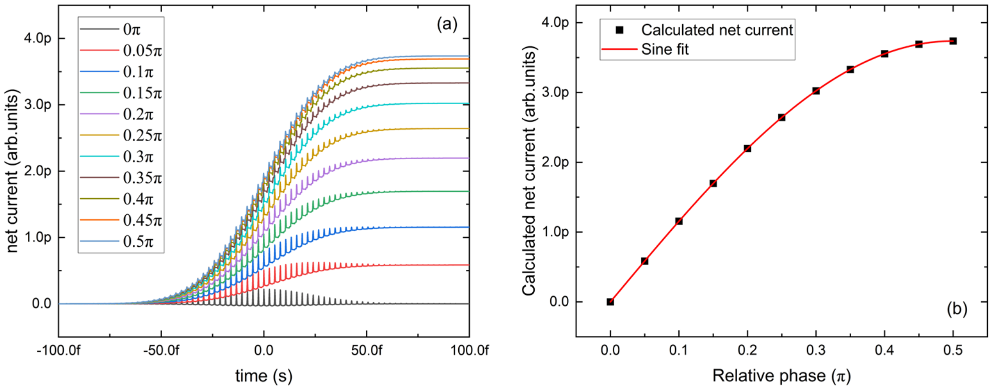

Figure 2.8 Calculated net current intensity within a 100-fs pulse period (a) and sine function dependence of maximum value (b).

2.6.4 *BBO azimuth*

Most of the two-color ionization schemes currently used in the laboratory are all-in-line second harmonic and THz generation arrangements as shown in Fig. 2.9(a). The commonly used β-BBO is a negative uniaxial crystal, which has a larger refractive index for ordinary beam (ô) than extraordinary (ê) beam. The second harmonic generation is achieved by satisfying the type-I phase-matching condition of angular tuning, i.e. ô(ω) + ô(ω) → ê(2ω) [28]. If only the fundamental frequency light along the o-axis is incident, the polarization direction of the 2ω beam emitted from the BBO is orthogonal to the ω beam.

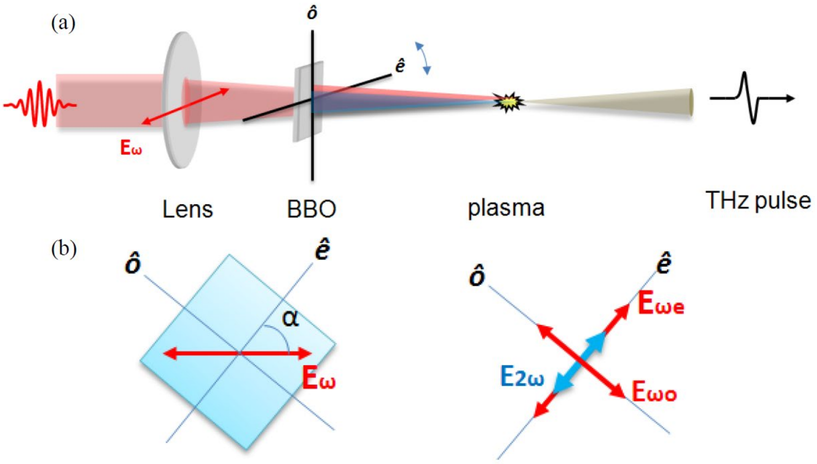

Figure 2.9 (a) THz and second harmonic generation in the same optical path. (b) The BBO crystal is rotated to an angle α with the polarization direction of the incident fundamental beam to ensure that the extraordinary polarization component in the crystal is parallel to the second harmonic. (Reprinted from [29])

Although there is maximum second harmonic generation efficiency, it is difficult to observe strong THz generation because the orthogonal mixing field cannot effectively accelerate the free electrons in the plasma. Therefore, the tuning of an azimuthal orientation of the BBO crystal is required. As can be seen in Fig. 2.9(b), when the fundamental laser beam passes through the birefringent BBO crystal, its amplitude can be decomposed into two orthogonal polarization directions, $E_{\omega o}$ and $E_{\omega e}$, along the ô and ê axes in the crystal respectively. In this case, the fundamental pulse becomes elliptically polarized as it passes through the BBO, while the second harmonic remains polarized along the ê axis. Then the combined laser field at the focus is expressed as:

$$E_{\mathrm{L}}(t) = E_{\omega e}(t)\cos(\omega t)\,\hat{e} + E_{\omega o}(t)\cos(\omega t + \varphi)\hat{o} + E_{2\omega e}(t)\cos(2\omega t + \theta)\hat{e}, \quad (2.30)$$

where φ is the phase difference due to the difference in refractive index along the ô and ê axes in the crystal inside the BBO crystal, which can be controlled by tilting the angle of the BBO crystal and thus varying the optical path length. Thus, both azimuth and tilt angle need to be carefully adjusted to obtain the maximum THz output. In addition, it is also feasible to add a dual-wavelength waveplate (DWP) after the BBO crystal to achieve the strongest THz output while meeting the maximum second harmonic generation efficiency [30].

2.6.5 *Pump wavelength and frequency combination*

Most experiments with two-color filaments have been done between 800 nm and 400 nm frequency combinations, but the possibility of other frequency ratios is not denied. Kostin et al. performed detailed calculations with ω_2/ω_1 from 0.4 to 3 and found that THz radiation can also be generated when ω_2/ω_1 is 2/3 and 3/2 [31]. These conclusions were verified experimentally by Zhang et al., and they found that the multi-wave mixing theory cannot explain the scaling law and polarization modulation, while the PC model can explain these phenomena well [32]. In addition, three-color combinations have also been tried, and a wider bandwidth THz pulse has been achieved [33]. It has also been recently shown that the two-color filamentation of a 3.9 μm femtosecond mid-infrared laser pulse can produce ultrashort THz pulses with sub-millijoule energy and 2.36% conversion efficiency [34]. Compared to the 800 nm near-IR laser, long wavelength pulses can provide greater acceleration for free electrons in a single optical cycle, thereby increasing the transient current to improve THz yield. These new attempts have inspired new possibilities for the development of strong THz sources.

2.7 AIR-BIASED COHERENT DETECTION (ABCD) METHOD

Gas-based detectors are also powerful tools for detecting ultrawideband THz pulses. Since gases have little dispersion in the optical and THz ranges, the gas-based THz detection is not affected by phase mismatch in EO sampling schemes. A typical example is the air-biased coherent detection (ABCD) method which can achieve coherent detection means to obtain the electric field amplitude of THz pulses [35]. ABCD does not require ionized air, the detection mechanism is based on the second harmonic generation induced by the third-order nonlinear effect of a gaseous medium under the strong THz field. As shown in Fig. 2.10(a), the probe fundamental pulse (red) and the THz beam (blue) are co-focused and produce a second harmonic (purple). The fundamental frequency is filtered by an infrared filter (IRF) and the intensity of second harmonic pulses are detected by a photomultiplier tube (PMT). This process can be expressed as [35]

$$E_{2\omega} \propto \chi^{(3)} I_\omega E_{\text{THz}} , \tag{2.31}$$

where $E_{2\omega}$ and E_{THz} are respectively the second harmonic and THz electric field, and I_ω is the fundamental beam intensity. Since $E_{2\omega} \propto E_{\text{THz}}$, the measured SH intensity $I_{2\omega}$ is proportional to the THz intensity I_{THz}, i.e. $I_{2\omega} \propto I_{\text{THz}}$ (hollow purple column in Fig. 2.10(b)). Due to this, we can only obtain the intensity-correlation signal which does not contain phase information (see Fig. 2.11(a)). By introducing a bias voltage E_{DC} at the optical focus, the bias field induces a second harmonic pulse-field, thus the time-dependent second harmonic intensity can be expressed as

$$I_{2\omega} \propto \left(\chi^{(3)} I_\omega\right)^2 \cdot (E_{\text{THz}} + E_{\text{DC}})^2 \propto (E_{\text{THz}}^2 + 2E_{\text{THz}}E_{\text{DC}} + E_{\text{DC}}^2) . \tag{2.32}$$

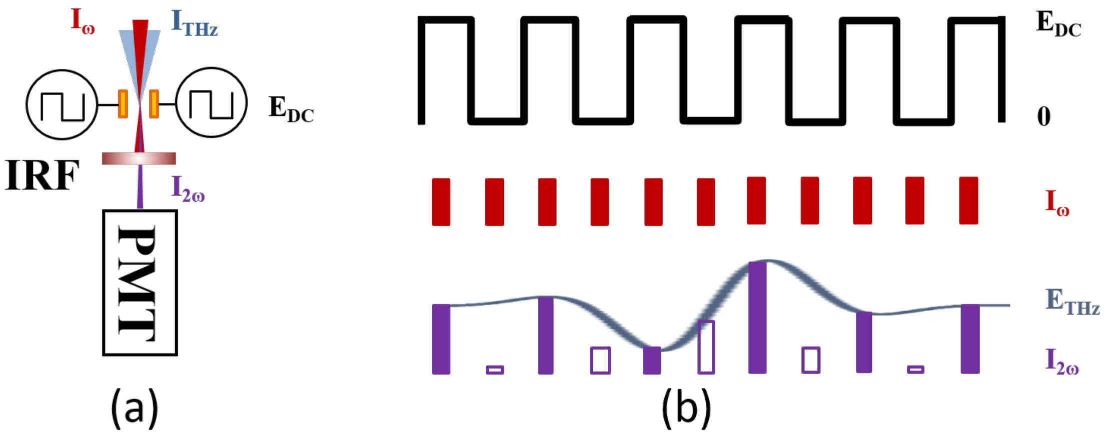

Figure 2.10 Schematic of the ABCD detection device (a) and the coherent detection principle (b). The fundamental probe beam (red) and THz beam (blue) are focused between two high-voltage electrodes and generate the second harmonic (purple). Without the bias voltage, only the THz contributes to the second harmonic generation (hollow purple); With the bias voltage, both the bias field and THz fields contribute to the second harmonic generation, and a cross term

proportional to the THz field strength exists (solid purple). By extracting the cross term with phase-sensitive (lock-in) detection and controlling the time delay between the probe pulse and the THz pulse, the instantaneous THz field can be sampled and obtain the THz waveform.

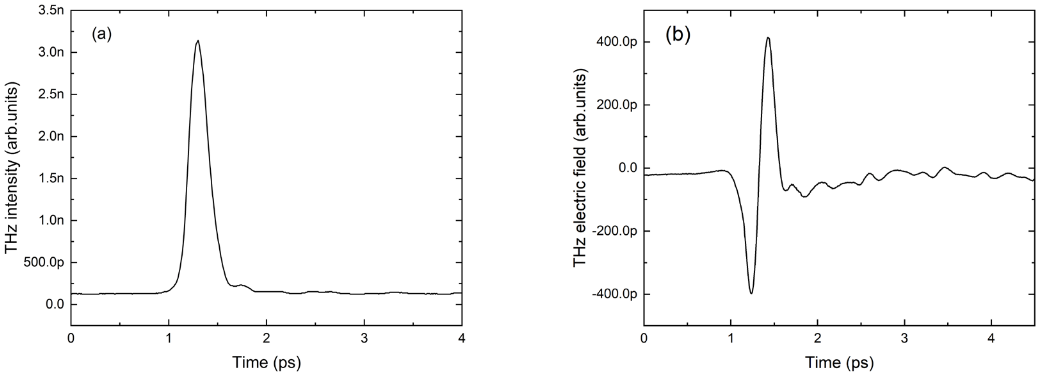

Figure 2.11 (a) Time-resolved THz intensity signal measured by induced second harmonic generation method; (b) THz electric field amplitude obtained by coherent detection through the introduction of an external bias.

The bias voltage E_{DC} can be switched at a period of half of the repetition rate and act as a local oscillator. Therefore, the cross term in Eq. (2.32) which is linearly proportional to the THz field amplitude (solid purple column in Fig. 2.10(b)) can be eventually isolated from the switching frequency by a lock-in amplifier. THz pulse can be then sampled by varying the delay between the pump and probe laser pulse so that the entire temporal waveform can be obtained (see Fig.2.11 (b)). Since the frequency coverage is not limited by the phonon resonance and reflection from the interface, the temporal shape of THz pulses emitted from the filament can be measured with nearly no distortion. As shown in Fig. 2.12, when the 30 THz bandwidth source is sampled by a 1-mm-thick ZnTe crystal, the lattice vibration mode centered around 5.3 THz limits the bandwidth to only 2.5 THz. But for an ABCD device, the entire source bandwidth can be effectively detected [36].

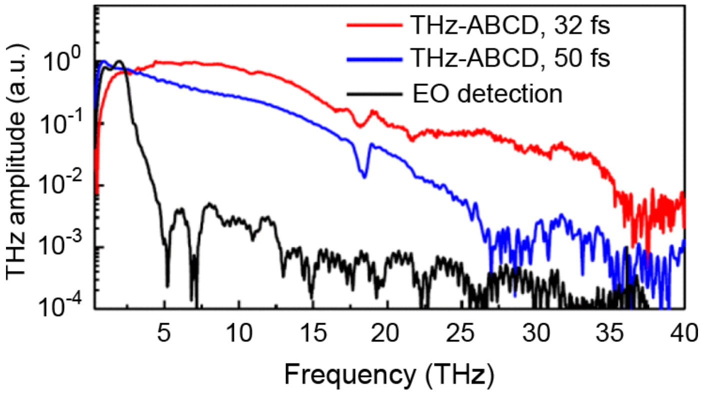

Figure 2.12 Two-color laser plasma emitted THz spectra detected by EO (1 mm thick ZnTe crystal) sampling (black) and THz-ABCD technique using 32 fs (red) and 50 fs (red) laser pulses, respectively. (Reprinted from [36])

2.8 CONCLUSION

This chapter briefly reviews the mechanism of photoionization, laser field propagation with intensity induced nonlinearities and THz radiation from the two-color laser plasma current surge. The ionization caused by the intense laser field interacts with the third-order nonlinear effects in the gas medium, leading to a complex filamentation process. In which the asymmetric currents due to the two-color laser field are considered as the main mechanism of far-field THz radiation. Although the phenomenology-based four-wave mixing model has been proposed, it has a number of limitations including the inability to account for the conversion efficiency of third-order nonlinear effects. In addition, some important parameters affecting the THz yield are presented, including the incident IR power related to scaling and the phase difference of the two-color light for the phase-matching condition. After that, we present the air-based coherent detection scheme, which allows for a wider frequency range due to the absence of solid material dispersion.

REFERENCES:

1. L. V. Keldysh, "Ionization in the Field of a Strong Electromagnetic Wave," J. Exp. Theor. Phys. 20, 1307 (1965).
2. A. Dubietis, G. Tamošauskas, R. Šuminas, V. Jukna, and A. Couairon, "Ultrafast Supercontinuum Generation in Bulk," Lith. J. Phys. 57, 113–157 (2017).
3. P. H. Bucksbaum, R. R. Freeman, M. Bashkansky, and T. J. McIlrath, "Role of the ponderomotive potential in above-threshold ionization," J. Opt. Soc. Am. B 4, 760 (1987).
4. K. Yamanouchi, S. L. Chin, P. Agostini, and G. Ferrante, Progress in Ultrafast Intense Laser Science II, Springer Series in Chemical Physics (Springer Berlin Heidelberg, 2007), Vol. 85.
5. K. Yamanouchi, S. L. Chin, P. Agostini, and G. Ferrante, Progress in Ultrafast Intense Laser Science III, Springer Series in Chemical Physics (Springer Berlin Heidelberg, 2008), Vol. 89.
6. R. Boyd, Nonlinear Optics (Elsevier, 2020).
7. A. V. Husakou and J. Herrmann, "Supercontinuum generation of higher-order solitons by fission in photonic crystal fibers," Phys. Rev. Lett. 87, 203901-1-203901–4 (2001).
8. L. Bergé, S. Skupin, R. Nuter, J. Kasparian, and J. P. Wolf, "Ultrashort filaments of light in weakly ionized, optically transparent media," Reports Prog. Phys. 70, 1633–1713 (2007).
9. G. Fibich and B. Ilan, "Deterministic vectorial effects lead to multiple filamentation," Opt. Lett. 26, 840 (2001).
10. S. Amiranashvili and A. Demircan, "Hamiltonian structure of propagation equations for ultrashort optical pulses," Phys. Rev. A - At. Mol. Opt. Phys. 82, 1–11 (2010).
11. S. Amiranashvili, A. G. Vladimirov, and U. Bandelow, "A model equation for ultrashort optical pulses around the zero dispersion frequency," Eur. Phys. J. D 58, 219–226 (2010).
12. J. C. Diels and W. Rudolph, Ultrashort Laser Pulse Phenomena, Second Edi (Elsevier, 2006).
13. I. G. Koprinkov, "Ionization variation of the group velocity dispersion by high-intensity optical pulses," Appl. Phys. B Lasers Opt. 79, 359–361 (2004).
14. Y. H. Chen, S. Varma, T. M. Antonsen, and H. M. Milchberg, "Direct measurement of the electron density of extended femtosecond laser pulse-induced filaments," Phys. Rev. Lett. 105, (2010).
15. J. H. Marburger, "Self-focusing: Theory," Prog. Quantum Electron. 4, 35–110 (1975).

16. A. Couairon and A. Mysyrowicz, "Femtosecond filamentation in transparent media," Phys. Rep. 441, 47–189 (2007).
17. D. J. Cook and R. M. Hochstrasser, "Intense terahertz pulses by four-wave rectification in air," Opt. Lett. 25, 1210 (2000).
18. X. Xie, J. Dai, and X.-C. Zhang, "Coherent Control of THz Wave Generation in Ambient Air," Phys. Rev. Lett. 96, 075005 (2006).
19. V. A. Andreeva, O. G. Kosareva, N. A. Panov, D. E. Shipilo, P. M. Solyankin, M. N. Esaulkov, P. González De Alaiza Martínez, A. P. Shkurinov, V. A. Makarov, L. Bergé, and S. L. Chin, "Ultrabroad terahertz spectrum generation from an air-based filament plasma," Phys. Rev. Lett. 116, 1–5 (2016).
20. A. Sharma, M. N. Slipchenko, M. N. Shneider, X. Wang, K. A. Rahman, and A. Shashurin, "Counting the electrons in a multiphoton ionization by elastic scattering of microwaves," Sci. Rep. 8, 2874 (2018).
21. C. Jusko, A. Sridhar, E. Appi, L. Shi, U. Morgner, and M. Kovacev, "Filamentation-assisted plasma lifetime measurements in atomic and molecular gases via third-harmonic enhancement," J. Opt. Soc. Am. B 36, 3505 (2019).
22. A. Talebpour, J. Yang, and S. L. Chin, "Semi-empirical model for the rate of tunnel ionization of N2 and O2 molecule in an intense Ti:sapphire laser pulse," Opt. Commun. 163, 29–32 (1999).
23. K. Y. Kim, A. J. Taylor, J. H. Glownia, and G. Rodriguez, "Coherent control of terahertz supercontinuum generation in ultrafast laser–gas interactions," Nat. Photonics 2, 605–609 (2008).
24. M. Kress, T. Löffler, S. Eden, M. Thomson, and H. G. Roskos, "Terahertz-pulse generation by photoionization of air with laser pulses composed of both fundamental and second-harmonic waves," Opt. Lett. 29, 1120 (2004).
25. M. Li, W. Li, Y. Shi, P. Lu, H. Pan, and H. Zeng, "Verification of the physical mechanism of THz generation by dual-color ultrashort laser pulses," Appl. Phys. Lett. 101, 1–4 (2012).
26. K.-Y. Kim, "Generation of coherent terahertz radiation in ultrafast laser-gas interactions," Phys. Plasmas 16, 056706 (2009).
27. Y. S. You, "Physical Mechanism of Terahertz Generation in Two-color Photoionization," University of Maryland, College Park (2014).
28. W. Zhang, H. Yu, H. Wu, and P. S. Halasyamani, "Phase-Matching in Nonlinear Optical Compounds: A Materials Perspective," Chem. Mater. 29, 2655–2668 (2017).
29. T. I. Oh, Y. S. You, and K. Y. Kim, "Two-dimensional plasma current and optimized terahertz generation in two-color photoionization," Opt. Express 20, 19778 (2012).

30. Y. Minami, T. Kurihara, K. Yamaguchi, M. Nakajima, and T. Suemoto, "High-power THz wave generation in plasma induced by polarization adjusted two-color laser pulses," Appl. Phys. Lett. 102, 041105 (2013).

31. V. A. Kostin, I. D. Laryushin, A. A. Silaev, and N. V. Vvedenskii, "Ionization-Induced Multiwave Mixing: Terahertz Generation with Two-Color Laser Pulses of Various Frequency Ratios," Phys. Rev. Lett. 117, 19–21 (2016).

32. L.-L. Zhang, W.-M. Wang, T. Wu, R. Zhang, S.-J. Zhang, C.-L. Zhang, Y. Zhang, Z.-M. Sheng, and X.-C. Zhang, "Observation of Terahertz Radiation via the Two-Color Laser Scheme with Uncommon Frequency Ratios," Phys. Rev. Lett. 119, 235001 (2017).

33. V. Vaičaitis, O. Balachninaite, U. Morgner, and I. Babushkin, "Terahertz radiation generation by three-color laser pulses in air filament," J. Appl. Phys. 125, (2019).

34. A. D. Koulouklidis, C. Gollner, V. Shumakova, V. Y. Fedorov, A. Pugžlys, A. Baltuška, and S. Tzortzakis, "Observation of extremely efficient terahertz generation from mid-infrared two-color laser filaments," Nat. Commun. 11, 292 (2020).

35. N. Karpowicz, J. Dai, X. Lu, Y. Chen, M. Yamaguchi, H. Zhao, X.-C. Zhang, L. Zhang, C. Zhang, M. Price-Gallagher, C. Fletcher, O. Mamer, A. Lesimple, and K. Johnson, "Coherent heterodyne time-domain spectrometry covering the entire “terahertz gap,”" Appl. Phys. Lett. 92, 011131 (2008).

36. J. Dai, B. Clough, I. Ho, X. Lu, J. Liu, and X. Zhang, "Recent Progresses in Terahertz Wave Air Photonics," IEEE Trans. Terahertz Sci. Technol. 1, 274–281 (2011).

Chapter 3. **SELF-PHASE MODULATION EFFECT ON THZ ENERGY EVOLUTION**

3.1 SCALING LAW FAILURE OF THE PC MODEL

The asymmetric transient plasma current (PC) model successfully explains the THz radiation in laser-gas interactions. It shows that the nonlinearity responsible for this phenomenon is caused by tunneling ionization and subsequent electron motion in the laser field. Despite being one-dimensional in time and not including transport, space charge, or re-scattering effects, the model can explain the phase-dependent THz radiation very well. However, for practical applications, it still needs to involve the nonlinear effects in the filament associated with changes of the refractive index when the pulse propagates through gaseous media that have not been considered. A number of nonlinear optical phenomena of strong field-induced filaments have been reported, such as supercontinuum generation [1–3], self-steepening [3], and intensity clamping [4,5], etc. These nonlinearities may have a profound impact on the THz emission, leads to the time domain reshaping of the THz pulse, or even to the failure of the scaling law. With this in mind, we need to re-understand the physical mechanism of pulse propagation in a filament and study the THz modulation due to nonlinearity in depth.

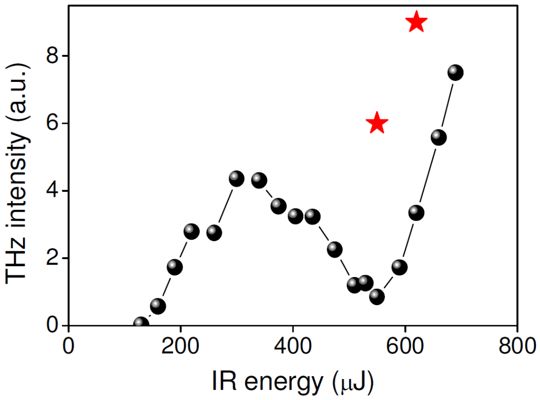

Figure 3.1 THz intensity as a function of the incident IR pulse energy. The stars show the results with the BK7 rephaser for quasi phase-matching. (Reprinted from [1])

The scaling law of the PC model seems to suggest that the THz yield is guaranteed to its maximum efficiency as long as the relative phase of the two-color field in the optical path is precisely controlled to $\pi/2$. However, some studies demonstrated that the oscillatory behavior of the THz intensity evolution when the IR laser pulse energy is increased without artificially introducing an additional phase difference. We can see clearly that a tendency to decrease with pulse energy at 300~600 μJ shown in Fig. 3.1 reported by Liu et al [6]. By re-compensating the phase, the THz output can meet the scaling law again as red star marks. This observation differs from the previously mentioned scaling law where THz yield increases monotonically with increasing IR pump energy.

Besides this, some studies also demonstrated some intriguing observations that the maximum THz yield regulated by the distance d between the BBO and the focal point was not always at a fixed position. In such a measurement, due to the dispersion of air, distance d modulates the relative phase between ω and 2ω. The air dispersion induced phase slippage can be described as

$$\Delta\theta = 2\omega\,(n_{2\omega} - n_{\omega})\,/\,c, \tag{3.1}$$

where c is the speed of light in vacuum, n_{ω} and $n_{2\omega}$ are the refractive indices of the fundamental and second-harmonic waves in air, respectively [7]. In general, this dispersion law remains unchanged in situations where the surrounding environment, such as temperature and pressure, does not change drastically. It fixes the relative phase evolution between ω and 2ω at the focus with the limit of a localized plasma. However, when the incident power and the focal length of the lens are changed, the deviation of the optimal THz generation position on the millimeter to centimeter scale is observed [6,8] (see Fig.3.2). These observations indicate that there are additional factors causing the failure of the scaling law during the photoionization process.

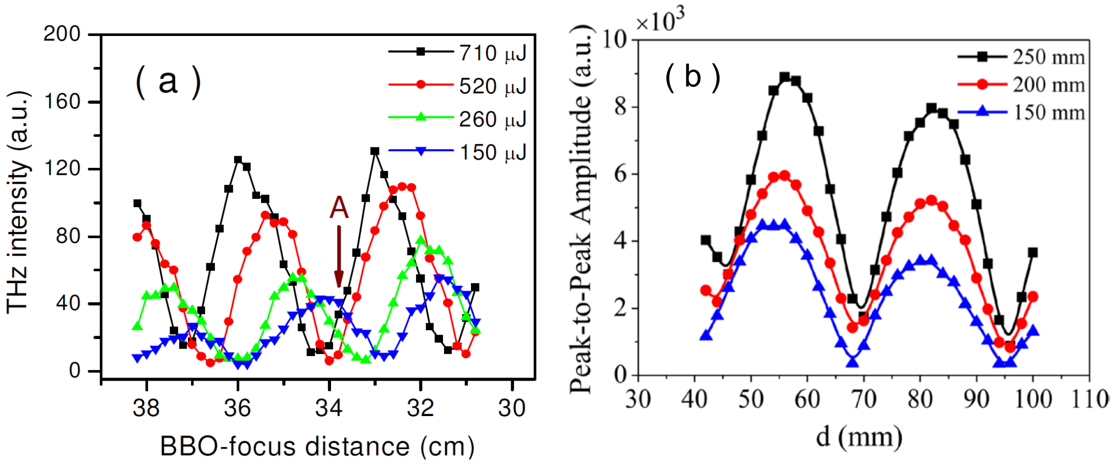

Figure 3.2 THz peak-to-peak amplitude versus BBO-to-plasma distance with (a) different IR pump energy and (b) different focusing lenses. (Reprinted from [6] and [8])

In this chapter, we introduce our quantitatively investigation of the evolution of THz radiation from a two-color laser filament in the air by varying the incident infrared pulse energy and BBO to focal length. The shift of the optimal position of the THz radiation observed in the experiment implies an intensity-dependent additional relative phase. Theoretical analysis suggests that this phase is likely to originate from the self-phase modulation due to the nonlinear refractive index of the filament formation process, because the spectral broadening of the two-color pulsed field after passing through the filament is also closely related to the same reason. This provide a clue for finding the cause of the failure of the scaling law.

3.2 INTENSITY INDUCED NONLINEARITIES

We have already discussed the nonlinear effects during the filamentation in Section 2.2. These additional refractive indices all exhibit properties that vary with the incident laser intensity. The typical ultrafast laser pulse has the property of time-varying intensity. For example, at sufficiently high input intensities, the output THz emission is accompanied by significant white light production as known as supercontinuum generation. And the stronger the input power, the more obvious this phenomenon is and the wider the spectrum covered. This is most likely explained by the intensity-dependent refractive index change resulting in temporal distortion of the laser pulse and is likely to be closely related to the modulation of the THz output. Due to the presence of an additional refractive index Δn, the interaction of the high-intensity optical field with the neutral gas and plasma leads to modulation of the pulse phase; i.e., self-phase modulation (SPM). Considering that the pulsed optical field is usually a Gaussian envelope, the refractive index is also time-varying. transform the time variable $\xi = t - z/v_g$ to a frame comoving with the group velocity v_g of the laser pulse. For the case of a monochromatic plane wave, the forward plane wave front is given by

$$\mathbf{E}(z,t) = \exp(i\omega_0 t - ik_z z) = \exp[i\omega_0 t - i\tfrac{\omega_0}{c}n(t)z] \quad , \tag{3.2}$$

with time-varying refraction index change:

$$n(t) = n_0 - \Delta n(t) = n_0 + n_2 I(t) - \tfrac{\omega_p^2}{\omega^2}. \tag{3.3}$$

Therefore, the additional phase introduced by the SPM at time ξ is expressed as:

$$\Delta\varphi_{\mathrm{SPM}}(\xi) = -\tfrac{\omega_0 \Delta n(\xi)}{c} z = \tfrac{\omega_0}{c}\left[\tfrac{\omega_p^2}{2n_0^2\omega_0^2} - \ n_2 I(\xi)\right] z\,, \tag{3.4}$$

and the pulse frequency change due to SPM is:

$$\Delta\omega_{\mathrm{SPM}}(\xi) = \tfrac{\partial}{\partial\xi}\varphi_{\mathrm{SPM}}(\xi) = \tfrac{e^2 z}{2n_0^2\varepsilon_0 m_e c\omega_0}\tfrac{\partial N_e(\xi)}{\partial\xi} - \tfrac{\omega_0 z}{c} n_2 \tfrac{\partial I(\xi)}{\partial\xi}. \tag{3.5}$$

Similarly, for the second harmonic wave 2ω that is co-focused with the fundamental wave ω and passes through the laser filament, it is also subjected to the nonlinear refractive index caused by the fundamental wave and is appended with an additional phase that results in a frequency shift. This process is also known as cross-phase modulation (XPM). The additional phase caused by XPM can be expressed as

$$\Delta\varphi_{\mathrm{XPM}}(\xi) = -\frac{2\omega_0\Delta n(\xi)}{c}z = \frac{2\omega_0}{c}\left[\frac{\omega_p^2}{8n_0^2\omega_0^2} - n_2 I(\xi)\right]z\,. \tag{3.6}$$

Likewise, the pulse frequency change due to XPM is:

$$\Delta\omega_{\mathrm{XPM}}(\xi) = \frac{\partial}{\partial\xi}\varphi_{\mathrm{SPM}}(\xi) = \frac{e^2 z}{4n_0^2\varepsilon_0 m_e c\omega_0}\frac{\partial N_e(\xi)}{\partial\xi} - \frac{2\omega_0 z}{c}n_2\frac{\partial I(\xi)}{\partial\xi}. \tag{3.7}$$

3.3 EXPERIMENT: RELATIONSHIP BETWEEN AIR DISPERSION INDUCED THz EMISSION EVOLUTION AND SPECTRAL BROADENING AND AT DIFFERENT INCIDENT LIGHT INTENSITIES

According to Eq. (3.4) and (3.6), ω and 2ω waves are appended with an additional phase due to the self-generated refractive index change, and their frequency shifts described by equations Eq. (3.5) and (3.7) correspond to what we observed as white light generation or spectra expansion by the same reason. Based on the above theoretical description, it is not difficult to speculate that additional phase slippage should be introduced when changing the incident IR power, which leads to a modulation in THz yield evolution related to the distance between the BBO-to-focal point. And it can be confirmed by relating ω and 2ω shifts caused by SPM and XPM with the modulated of THz intensity.

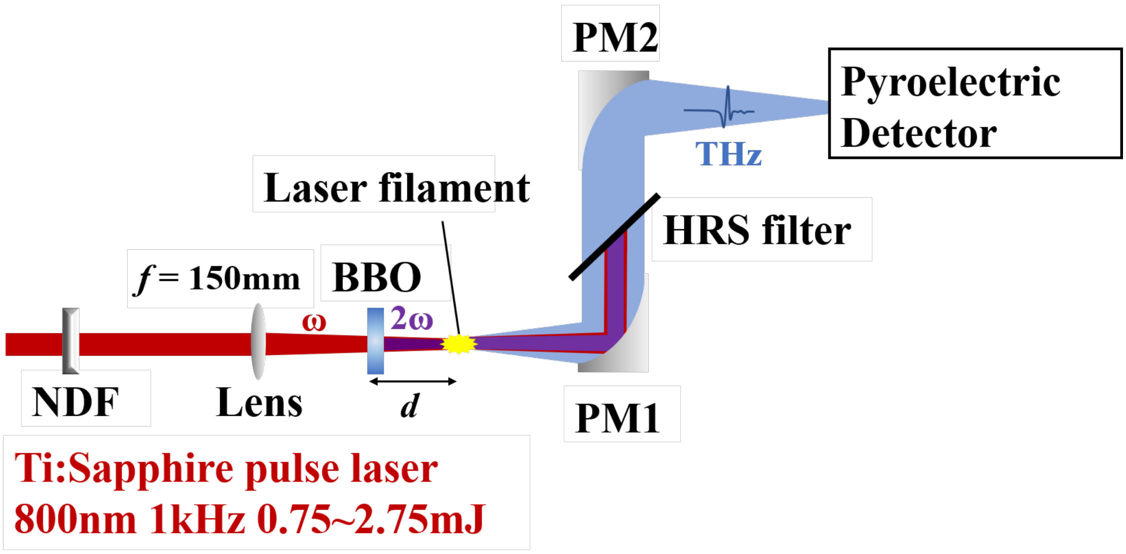

Figure 3.3 Schematic setup of a dual-color laser filament THz generation system.

Detailed information for experimental equipment shown in Fig. 3.3 and methods are explained in the following. All experiments were performed at room temperature and standard atmospheric pressure. We use a Ti:sapphire regenerative amplifier (Spitfire Pro, Spectra Physics) to generate horizontally polarized laser pulses with a center wavelength of 800 nm, repetition frequency of 1 kHz, and time width of 100 fs. These emitted intense laser pulses are focused by a convex lens with a focal length of 150 mm and then passed through a 0.1 mm thick type I β-BBO frequency doubling nonlinear crystal. By utilizing the BBO's second-order nonlinear effects, we can obtain the corresponding second harmonic pulses. The plane of incidence of the BBO crystal is adjusted to be perpendicular to the incident beam. By fixing the BBO crystal on a one-dimensional linear translation stage, the distance *d* between the BBO and the focal point can be adjusted in the range of 20 to 55 mm.

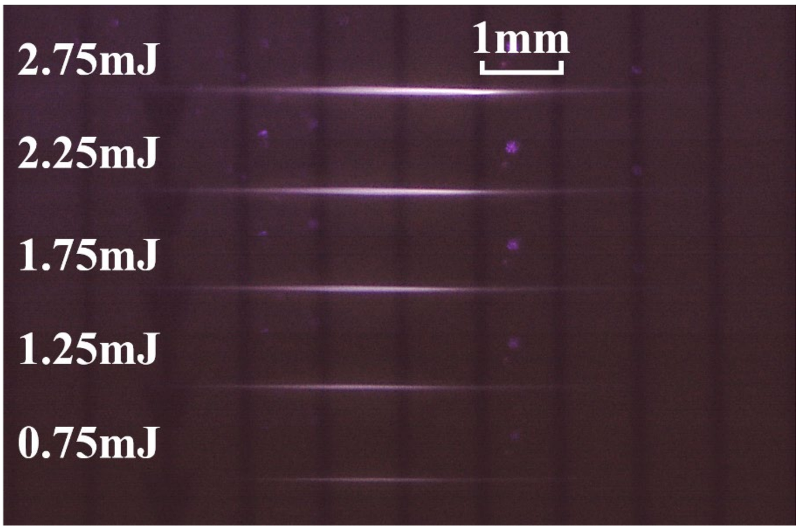

Figure 3.4 CCD images of two-color laser filaments taken at the corresponding incident pulse energy adjusted by a circular variable neutral density filter (NDF).

At the focal point, the intense photoelectric field ionized series of cumulative ionization trajectories that observed macroscopically along the propagation direction are known as laser filaments. Fig. 3.4 shows a series of photographs of the laser filament with different incident pulse energies captured by a charge-coupled device (CCD) camera. At a pulse energy of 2.75 mJ, the length of the laser filament is approximately 6 mm. Both the length and width of the filament decrease with incident IR power. These filaments exhibit a spindle shape with a brighter center and darker edges, and both length and width decrease with incident power.

After passing through the focus, unlike the deep red color of the incident fundamental frequency pulse, a series of ring-like iridescent tint emanated from the filament. THz radiation is collected and collimated by a pair of off-axis parabolic mirrors (PM1 and PM2) with the spectral broadened two-color pulses eliminated by a high-resistance silicon (HRS) filter. Subsequently, a calibrated pyroelectric detector (SPI-A-62-THz, Gentec-EO) is used to measure THz pulse energy varied with BBO-to-focus distance *d*. The detector has a spectral response covering a bandwidth from 0.1 to 30 THz, noise equivalent power (NEP) of 0.4 nW/Hz$^{-1/2}$, and a high responsiveness of 33 kV/W at a chopping frequency of 13 Hz. The pump pulse energy was adjusted from 2.75 mJ to 0.75 mJ by a circular variable neutral density filter (NDF).

The two-color spectra emitted directly from the laser filament were measured using a spectrometer (USB2000+, Ocean Optics) which was placed at the focal position of the second off-axis parabolic mirror PM2 when the HRS filter was removed. To prevent the probe from being damaged by the intense laser energy, we used a broadband attenuator covering the visible to infrared band with a uniform absorption spectrum.

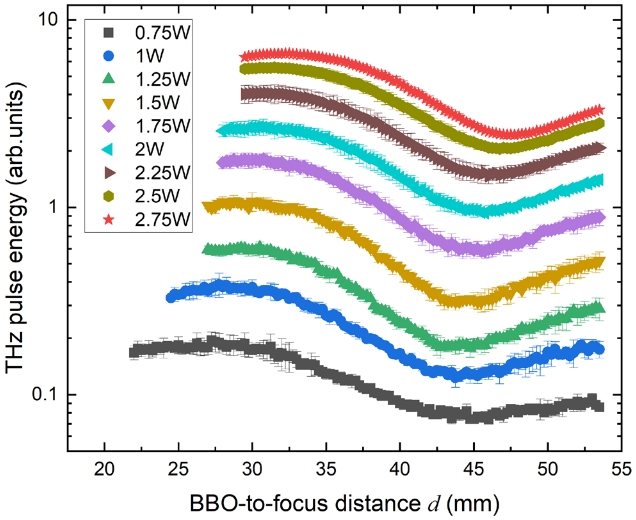

Figure 3.5 THz radiation evolution by changing the incident IR pulse energy and BBO-to-focal distance. Symbolic points are the THz pulse energy obtained at different BBO-to-focal distance *d* and incident pulse energy I_ω adjusted by an optical attenuator from 0.75 to 2.75 mJ. Error bars represent the standard deviation of three measurements.

Fig. 3.5 displays the measured THz pulse energy I_{THz} emitted from the two-color laser filament versus BBO-to-focal length *d*, with the incident IR pulse energy I_ω is adjusted from 0.75 to 2.75 mJ in units of 0.25 mJ. For ease of comparison, these data are presented on the logarithmic vertical axis.

The first point we notice is that as I_ω increases, I_{THz} shows an overall exponential growth and exhibits periodic oscillations with *d*. Similar to this oscillatory behavior mentioned before in Section 3.1, it is considered as a dispersion due to the difference in the refractive index of the air between ω and 2ω. Perhaps some readers have noticed that the period of oscillation, or the distance between peaks, is not the same as the values in some previous reports [17]. Because the data we measured are the total energy of the THz pulse, not the peak electric field amplitude at a specific time. According to the sinusoidal-dependent THz scaling related to the phase difference mentioned in Section 2.6.2, the oscillation should be expressed as $\sin^2\theta$ for $I \propto |E|^2$. A different trend, as we predicted, what we have found is a gradual shift of the max THz yield position away from the focus as I_ω increases. Similarly, the position of the minima varies by approximately the same degree, as shown in Fig. 3.6.

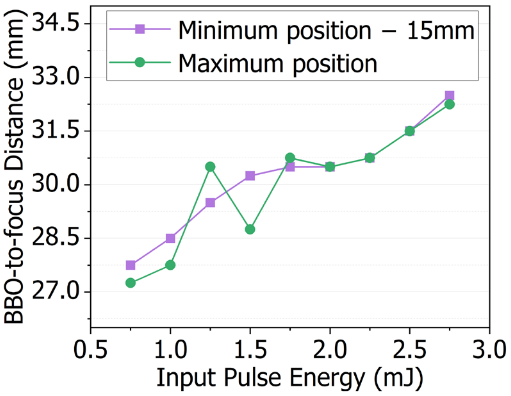

Figure 3.6 Variation of maximum and minimum THz yield position versus the incident IR pulse energy

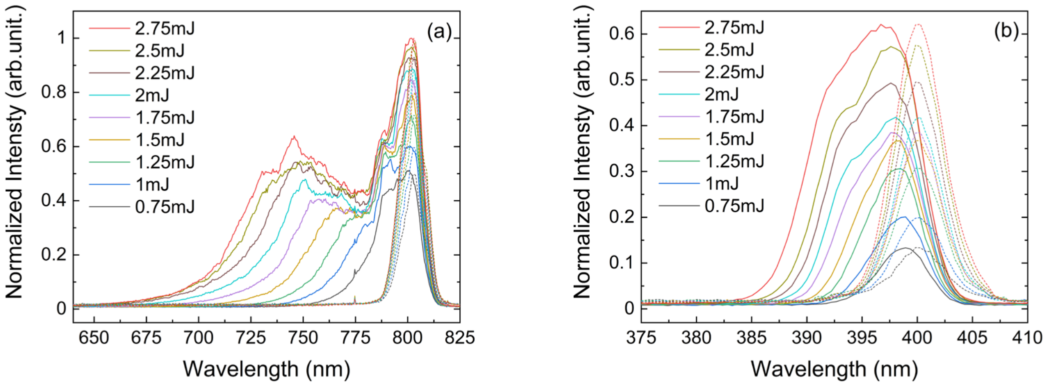

Figure 3.7 Normalized spectra of fundamental ω (a) and second harmonic 2ω (b). Solid lines are their spectra after propagating through the laser filament, and the dashed lines are the spectra measured before focus.

According to Fig. 3.6, the maximum value of the 2.75 mJ pump has a position shift of about 5 mm compared to the 0.75 mJ pump, suggesting an intensity-dependent phase shift. To gain insight into the origin of this phase shift, the spectra of the two-color pulses before and after focusing at different incident IR pulse energies are measured as presented in Fig. 3.7, in which the center frequency shift and increased broadening on the blue side of both ω and 2ω were observed as I_ω increased. In Fig. 3.7(a), The spectrum of the fundamental wave is extended to about 650 nm on the blue side with $I_\omega = 2.75$ mJ, which corresponds to a frequency shift of ~ 80 THz. And a plateau-like spike is formed near 740 nm. The spectrum expansion of 2ω light shown in Fig. 3.7(b), although also broadened to the blue side, is not as pronounced as that of ω light, which is only about 20 THz. Surprisingly, the spectral broadening occurs only on the blue side, while no shift is observed on the red side. The second terms on the r.h.s. of Eq. (3.5) and (3.7) have explicitly shown that these nonlinear contributions of the optical Kerr effect account for the negative increments of frequency, i.e., redshifts. And the positive increment of frequency is contributed by the free electrons, which corresponds to the blueshift.

However, the previously described filamentation process does not involve external geometric focusing. When geometric focusing is added to self-focusing, a concave wavefront with greater curvature compared to a self-focusing planar wavefront. To overcome this stronger focusing, the self-generated plasma must become denser, and the free carrier density increases dramatically so that negative lensing effects can balance the focusing effects. We introduce the lens equivalent refractive index n_{lens} when it is added to the nonlinear increase of the refractive index and they are balanced together by the refractive index of the self-generated plasma, i.e.

$$n_{\text{lens}} + n_2 I = \frac{\omega_p^2}{\omega^2} \quad . \tag{3.8}$$

There is no doubt that to reach this equilibrium, N_e must be larger than it would be without geometric focusing (free propagation). And small changes in intensity during highly nonlinear multiphoton/tunneling ionization will result in a large increment in plasma density. In this case, whether it is the refractive index change caused by the lens or the optical Kerr effect, their time derivative is negligible compared to the plasma contribution, so that almost no redshift component is present in the spectra we observe. Therefore, we assume that only the spectral blueshift due to the plasma contributes to all additional phases. Set the pulse peak at the time coordinate origin, the SPM induced total phase slippage of the fundamental wave with pulse width τ_0 can be calculated as follows:

$$\Delta\varphi_{\text{SPM}} = \int_{-\tau_0/2}^{+\tau_0/2} \omega_{\text{SPM}}(\xi) d\xi \cong \frac{e^2 z}{2 n_0^2 \varepsilon_0 m_e c \omega_0} \int_{-\tau_0/2}^{+\tau_0/2} \mathrm{d}N_e(\xi). \tag{3.9}$$

In the same way, for a second harmonic wave with a pulse width of τ_0', we have:

$$\Delta\varphi_{\text{XPM}} = \int_{-\tau_0'/2}^{+\tau_0'/2} \omega_{\text{XPM}}(\xi) d\xi \cong \frac{e^2 z}{4 n_0^2 \varepsilon_0 m_e c \omega_0} \int_{-\tau_0'/2}^{+\tau_0'/2} \mathrm{d}N_e(\xi). \tag{3.10}$$

As can be seen from Eqs. (3.9) and (3.10) based on the plane wave assumption, the phase shift due to the filament is only related to the integration of $\mathrm{d}N_e(\xi)$ with time. We assume that the two-color pulses have the same pulse width and little deviate in the axial propagation distance, the total phase shift $\Delta\varphi_{\text{SPM}}$ for fundamental wave through the laser filament can be then considered proportional to its frequency shift $\Delta\omega_{\mathrm{SPM}}$, i.e. $\Delta\varphi_{\mathrm{SPM}} \propto \Delta\omega_{\mathrm{SPM}}$, and similarly $\Delta\varphi_{\mathrm{XPM}} \propto \Delta 2\omega_{\mathrm{XPM}}$. Based on these approximations, the additional relative phase $\Delta\theta_{\mathrm{f}}$ of the two-color laser caused by SPM and XPM can be written as follows

$$\Delta\theta_{\mathrm{f}} \propto \Delta\omega_{\mathrm{SPM}} - \Delta 2\omega_{\mathrm{XPM}}. \tag{3.11}$$

However, it is important to note that in practice, inhomogeneous intensity distributions near the focal point may lead to invalidation of the plane wave assumption. A more general approach is to further resolve the spatial distribution of the laser pulse as a three-dimensional function by converting the effect of the lens into a transversely equivalent refractive index and combining it with plasma self-scattering focus. That is, the transverse Laplace operator in Eq. (2.8) needs to be solved. However, a full theoretical consideration of the dispersion inside the filament requires extensive numerical simulations of the propagation process to obtain each ionization event with spatially distributed laser intensity. Limiting the capabilities of this dissertation, we simply model the filament as a uniform one-dimensional line source and consider the phase modulation in the propagation direction only.

3.4 NONLINEAR FITTING FUNCTION

To extract the additional phase slippage associated with the incident light, we investigate the relationship between the input IR pulse energy I_ω, BBO to focal distance d by fitting the measured THz pulse energy evolution I_{THz} nonlinearly. We use the standard Levenberg-Marquardt algorithm with a tolerance of 10^{-6}. The oscillatory power function used for the fit is

$$I_{\mathrm{THz}} = \frac{I_\omega^3}{d}\left[\alpha + \beta \sin^2(\gamma d - \delta I_\omega + \varphi_0)\right]. \tag{3.12}$$

The best fit is shown as a curved surface in Fig. 3.8 with a coefficient of determination $R^2 = 0.9945$, and the fitted parameters are listed in Table 1.

Table 3.1 Fitting parameters of Eq. (3.12) based on the experimental results in Fig. 3.5 (SI units)

α	β	γ (fixed)	δ	φ_0
5.862×10^{-6}	5.069×10^{-6}	0.1211	3.104×10^{-4}	1.413

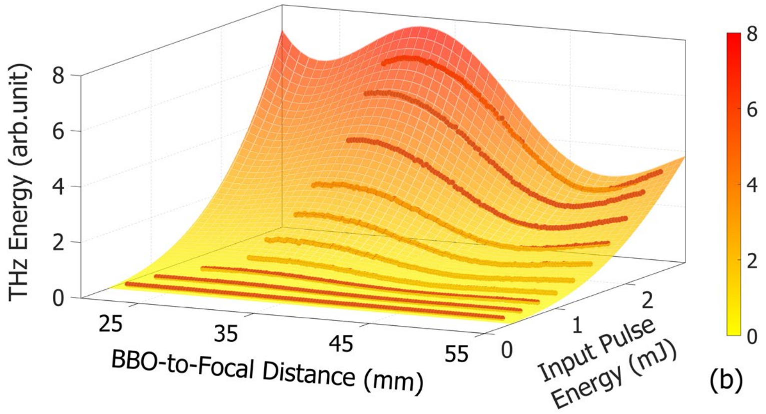

Figure 3.8 THz radiation evolution (solid dots) by changing the incident IR pulse energy and BBO-to-focus distance and the nonlinear curve fitting results (curved surface) according to Eq. (3.12)

The oscillation-related term in Eq. (3.12) is our primary concern. Note that this oscillation term is described by $\sin^2\theta$ rather than the sinusoidal-dependent mentioned in Section 2.6.3, since we measure the THz pulse energy I_{THz} instead of the electric field amplitude E_{THz}. The γd term denotes the air dispersion calculated using Eq. (3.1). The constant term φ_0 represents a series of additional relative phases during the propagation of ω and 2ω waves that are independent of I_ω and d, which may be caused by BBO birefringence mentioned in Section 2.6.4 or Gouy phase shift [20].

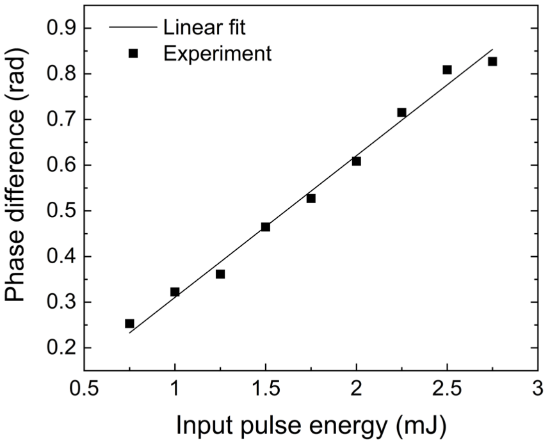

Figure 3.9 Intensity-dependent nonlinearity induced two-color relative phase evolution. Additional relative phase shift $\Delta\theta_f$ calculated from Eq. (3.11) (square) and linear fitting δI_ω from Eq. (3.12) (solid line) as a function of the incident pulse energy.

The linear relative phase δI_ω, which depends on I_ω, seems to be caused by the plasma dispersion. Filament introduced phase slippage obtained by subtracting the frequencies at the 1/e

peak of the spectrum before and after focusing shown in Fig. 3.7, calculated by Eq. (3.11), are represented as squares in Fig. 3.9, and they are fitted by the linear correlation term δI_ω as shown by the solid line. The good agreement between the measured data and fitted term supports that the intensity-dependent laser-induced filament affects the relative phase of the two-color laser field.

In addition, the non-zero minimum value in the oscillation curve is also a point worth noting. According to Section 2.6.3, the minimum value of the THz yield regulated by the sinusoidal function should be zero, corresponding to the case of no net current generation in Fig 2.8. According to Section 2.6.4, the polarization of the 2ω pulse generated from the BBO crystal is not parallel but at an angle θ to the incident ω pulse. Only the projected component of the ω field along the 2ω polarization contributes to the generation of THz. In this case, the generated THz pulse does not necessarily follow a polarization of ω or 2ω, but is usually elliptical [21]. In particular, the ellipticity is attributed to the laser phase and polarization modulation caused by the plasma. As the plasma length increases, the THz polarization evolves from linear to elliptical. If we consider a series of ionization events on the laser filament as a line THz source, the varying phase between the ω and 2ω fields on the line source also leads to a polarization change in the far-field radiation, as shown in Fig. 3.10. In other words, the XPM leads to a change in the polarization of the 2ω field, thus changing the emitted THz to elliptical polarization.

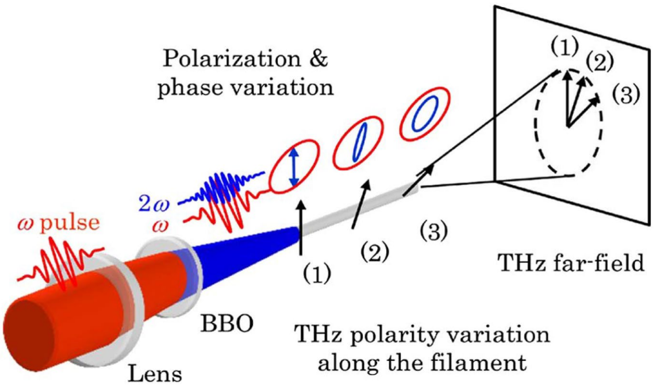

Figure 3.10 Schematic of two-color (ω and 2ω) laser pulse propagation and THz polarization rotation. The THz far-field is constructed from successive time-delayed THz waves emitted with varying polarization. (Reprinted from [21])

Then Eq. (3.12) can be considered as a superposition of two orthogonal polarization components, which can be rewritten as follows:

$$I_{\mathrm{THz}} = \frac{I_\omega^3}{d}\left[\alpha\cos^2(\gamma d - \delta I_\omega + \varphi_0) + (\alpha+\beta)\sin^2(\gamma d - \delta I_\omega + \varphi_0)\right]. \quad (3.13)$$

The sine and cosine functions in Eq. (3.13) represent the two orthogonal polarization components, respectively. To confirm this, we added a wire grid polarizer in front of the pyroelectric detector shown in Fig. 3.3 to measure the energy of THz pulses with different polarization directions at the corresponding peak positions. The measurement results are shown in Fig. 3.11. The two polarization intensity extremes agree with parameters described in Eq. (3.13), further verifying the accuracy of the fitting results.

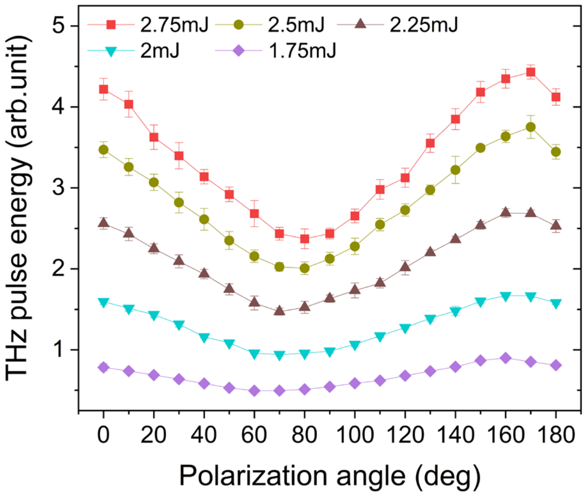

Figure 3.11 Dependence of THz intensity on polarization angle and input IR power.

3.5 CONCLUSION

In this chapter, we focus on the results noted in some previous studies that are inconsistent with the PC model scaling law, and speculate that it may be related to the nonlinear effects introduced by the intensity. According to the theoretical derivation, the nonlinear effects mainly originate from the photoionization of the plasma releasing free electrons. The two-color pulses propagating through the filament also cause spectral broadening due to the same modulation effect. This can be considered as a means to confirm our speculation.

By measuring the THz pulse energy evolution modulated by IR pump intensity and BBO-to-focus distance, we observe the optimal yield position shift with the IR intensity. An oscillatory exponential function is proposed to fit the observed THz pulse energy evolution, where there is a term that causes the relative phase of the THz modulation to be proportional to the incident pump pulse energy. Our speculation is supported by measuring the phase difference extracted from the two-color filament spectra of SPM and XPM, which are in good agreement with the linear term. and THz polarization quadrature component ratios also confirm the validity of the curve fit.

Although the phase modulation at short focal lengths is not as pronounced as for long laser filaments, the observed nonlinear effects introduced by the high-intensity optical field are still not negligible, which provides further insight into the formation and evolution mechanisms of the THz emission process. However, our result cannot explain the scalar law of THz energy versus incident infrared energy, i.e., the cubic term in the fitting function, which requires accurate spatio-temporal modeling of the filament within this particular experimental parameter range. This study will be useful to those studying the principles of THz generation mechanism of laser filaments and will also help to construct strong broadband THz sources and systems for further application experiments.

REFERENCES:

1. A. V. Husakou and J. Herrmann, "Supercontinuum generation of higher-order solitons by fission in photonic crystal fibers," Phys. Rev. Lett. **87**, 203901-1-203901–4 (2001).
2. R. R. Alfano, *The Supercontinuum Laser Source*, 3rd ed. (Springer-Verlag, 2006).
3. N. Aközbek, M. Scalora, C. M. Bowden, and S. L. Chin, "White-light continuum generation and filamentation during the propagation of ultra-short laser pulses in air," Opt. Commun. **191**, 353–362 (2001).
4. A. Becker, N. Aközbek, K. Vijayalakshmi, E. Oral, C. M. Bowden, and S. L. Chin, "Intensity clamping and re-focusing of intense femtosecond laser pulses in nitrogen molecular gas," Appl. Phys. B Lasers Opt. **73**, 287–290 (2001).
5. O. G. Kosareva, W. Liu, N. A. Panov, J. Bernhardt, Z. Ji, M. Sharifi, R. Li, Z. Xu, J. Liu, Z. Wang, J. Ju, X. Lu, Y. Jiang, Y. Leng, X. Liang, V. P. Kandidov, and S. L. Chin, "Can we reach very high intensity in air with femtosecond PW laser pulses?," Laser Phys. **19**, 1776–1792 (2009).
6. Y. Liu, A. Houard, M. Durand, B. Prade, and A. Mysyrowicz, "Maker fringes in the Terahertz radiation produced by a 2-color laser field in air," Opt. Express **17**, 11480 (2009).
7. P. E. Ciddor, "Refractive index of air: new equations for the visible and near infrared," Appl. Opt. **35**, 1566 (1996).
8. J. Xie, W.-H. Fan, and X. Chen, "Systematic experimental study on a highly efficient terahertz source based on two-color laser-induced air plasma," Laser Phys. **26**, 055002 (2016).
9. L. Bergé, S. Skupin, R. Nuter, J. Kasparian, and J. P. Wolf, "Ultrashort filaments of light in weakly ionized, optically transparent media," Reports Prog. Phys. **70**, 1633–1713 (2007).
10. G. Fibich and B. Ilan, "Deterministic vectorial effects lead to multiple filamentation," Opt. Lett. **26**, 840 (2001).
11. S. Amiranashvili and A. Demircan, "Hamiltonian structure of propagation equations for ultrashort optical pulses," Phys. Rev. A - At. Mol. Opt. Phys. **82**, 1–11 (2010).
12. S. Amiranashvili, A. G. Vladimirov, and U. Bandelow, "A model equation for ultrashort optical pulses around the zero dispersion frequency," Eur. Phys. J. D **58**, 219–226 (2010).
13. R. Boyd, *Nonlinear Optics* (Elsevier, 2020).
14. J. C. Diels and W. Rudolph, *Ultrashort Laser Pulse Phenomena*, Second Edi (Elsevier, 2006).

15. I. G. Koprinkov, "Ionization variation of the group velocity dispersion by high-intensity optical pulses," Appl. Phys. B Lasers Opt. **79**, 359–361 (2004).

16. Y. H. Chen, S. Varma, T. M. Antonsen, and H. M. Milchberg, "Direct measurement of the electron density of extended femtosecond laser pulse-induced filaments," Phys. Rev. Lett. **105**, (2010).

17. M. Kress, T. Löffler, S. Eden, M. Thomson, and H. G. Roskos, "Terahertz-pulse generation by photoionization of air with laser pulses composed of both fundamental and second-harmonic waves," Opt. Lett. **29**, 1120 (2004).

18. J. H. Marburger, "Self-focusing: Theory," Prog. Quantum Electron. **4**, 35–110 (1975).

19. A. Couairon and A. Mysyrowicz, "Femtosecond filamentation in transparent media," Phys. Rep. **441**, 47–189 (2007).

20. F. Lindner, G. G. Paulus, H. Walther, A. Baltuška, E. Goulielmakis, M. Lezius, and F. Krausz, "Gouy Phase Shift for Few-Cycle Laser Pulses," Phys. Rev. Lett. **92**, 113001 (2004).

21. Y. S. You, T. Il Oh, and K.-Y. Kim, "Mechanism of elliptically polarized terahertz generation in two-color laser filamentation," Opt. Lett. **38**, 1034 (2013).

Chapter 4. **SELF-PHASE MODULATION EFFECT ON THZ WAVEFORM MODULATION**

4.1 INTRODUCTION

The development of ultrafast lasers and new semiconductor technologies has ushered in a new epoch of THz science and technology development. Since the invention of the first THz photoconductive antenna by Auston et al. an effective method for coherent THz generation and detection has matured and is now widely known as THz time-domain spectroscopy (THz-TDS) [1]. This highly integrated system is based on a THz emitter, a THz detector, and an optical system arrangement for free-space coupling to the sample. In detail, the generation and detection of THz are accomplished by different methods related to several physical mechanisms mentioned in Chapter 1, and a parabolic mirror or a spherical silicon lens is used to guide the THz beam. Because direct electrical detectors and circuits typically have rise and fall times in the picosecond to nanosecond range, there is no effective means of temporal resolution for short THz pulses in the picosecond or even femtosecond range. The method to achieve sub-picosecond resolution is to use an optical technique in which ultrashort NIR light pulses (typically shorter than 100 fs) are split along two paths to generate a THz field that is time-dependent on the detection time. Note that THz-TDS generally uses a coherent measurement method to obtain the transient electric field of the THz time-domain signal rather than its intensity. Analyzing the amplitude and phase changes in the projected or reflected THz signal using a wave propagation analysis model provides direct access to the optical properties of the material under test, which is attractive to researchers in a wide range of fundamental disciplines.

Nowadays, THz-TDS systems have moved from just staying in the laboratories to commercial systems shared with wider society with rapidly improving performance. The advent of gaseous-media-based THz photonics offers the opportunity to efficiently convert the full bandwidth of ultrashort laser pulses into THz signals. The availability of such desktop two-color laser filament-based THz-TDS systems with extremely wide spectral bandwidths is tremendous, as it allows for a significantly extended frequency range, thus providing indispensable direct information about material properties and nonlinear effects in this new frequency range. Despite this, we note that the complex nonlinear dynamics between free-electrons and two-color laser fields during propagation in the filament have been significant influenced by the laser intensity and then modulate and the emitted THz temporal waveform characteristics. However, there are only a very limited number of reports for such phenomena. High-intensity pulses give rise to many of the nonlinear phenomena on the radiation itself, which associated nonlinear index of refraction over the temporally varying intensity profile $I(t)$. By varying the input IR pulse energy, the intensity causes an additional relative phase between the two-color pulses that cannot be ignored. With this in mind, it is necessary to understand the key role that nonlinearity plays in the THz emission mechanism from the laser filament.

In this chapter, we present the shaping of THz pulses emitted from bipolar laser filaments with different pump energies studied experimentally. Using a low-dispersion detection method, we find that the positive and negative peaks of the bipolar THz waveform increase and decrease with increasing excitation light power, respectively, and the smooth peak in the tail gradually disappears. We analyzed this phenomenon in detail based on the modified PC model and concluded that it was caused by a relatively rapid phase transition inside the filament. These results provide a unique possibility to directly understand the two-color field propagation dynamics and the THz wave generation mechanism during the interaction between the femtosecond laser and the air plasma.

4.2 EXPERIMENT: INTENSITY INDUCED PULSE SHAPING

The experimental setup is a home-built all gaseous-medium-based THz generation-detection system, as shown in Fig. 4.1. Horizontally polarized pulse of ~100 fs duration is generated from the same regenerative amplifier described in section 3.3 at a central wavelength of 800 nm with a 1 kHz repetition rate, and split into a pump beam and a detector beam by a beam splitter (BS) to generate and detect THz pulses. The pump pulse energy is first attenuated by a circular variable neutral density filter (NDF) and then focused by an off-axis paraboloidal mirror (PM1) with a reflected focal length of 152.4 mm. A 0.1 mm thick type I barium β-borate (BBO) crystal is fixed perpendicular to the incident light between the focal point and PM1 to generate the 2ω pulse. The co-propagating two-color pulses form a filament at the focal point. THz pulses from the filament are collected and collimated by a series of off-axis parabolic mirrors (PM2 ~ PM5) after the pump laser pulses are removed with a 0.35 mm thick high resistance silicon (HRS) filter. The detection beam is attenuated to ~40 μJ by another NDF and passed through a delay line for air-biased coherent detection (ABCD) device introduced in Section 2.7. We use a commercially available ABCD detector (ZAP-APD, Daheng New Epoch Technologies, Inc.) for THz pulse sampling. The entire optical path is purged with dry nitrogen gas to minimize the effect of water vapor.

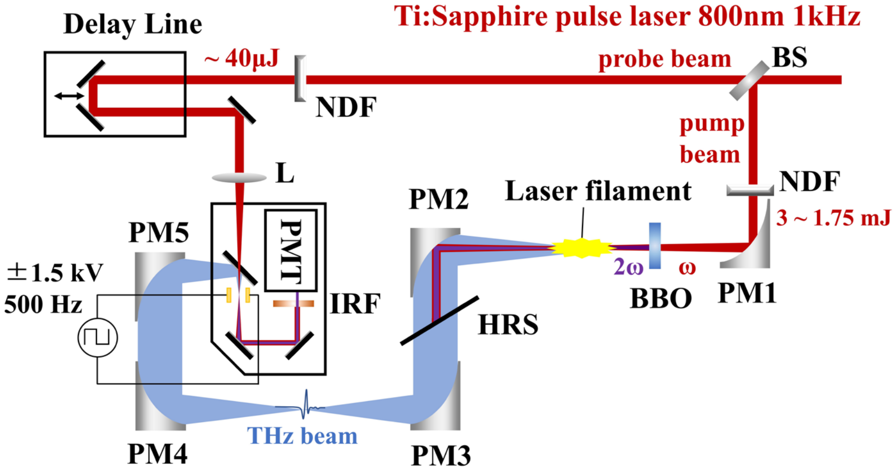

Figure 4.1 Schematic of all gaseous-medium-based THz spectroscopy system. BS, beam splitter; NDF, circular variable neutral density filter; PM1 ~ PM5, off-axis parabolic mirrors with reflected focal length of 152.4 mm (PM1, PM3, PM4), 50.8mm (PM2) and 101.6 mm (PM5); BBO, 0.1 mm-thick type-I β-barium borate; HRS, 0.35 mm-thick high-resistance silicon filter; L, plano-convex lens with focal length *f* = 100 mm; IRF, infrared filter; PMT, photomultiplier tube.

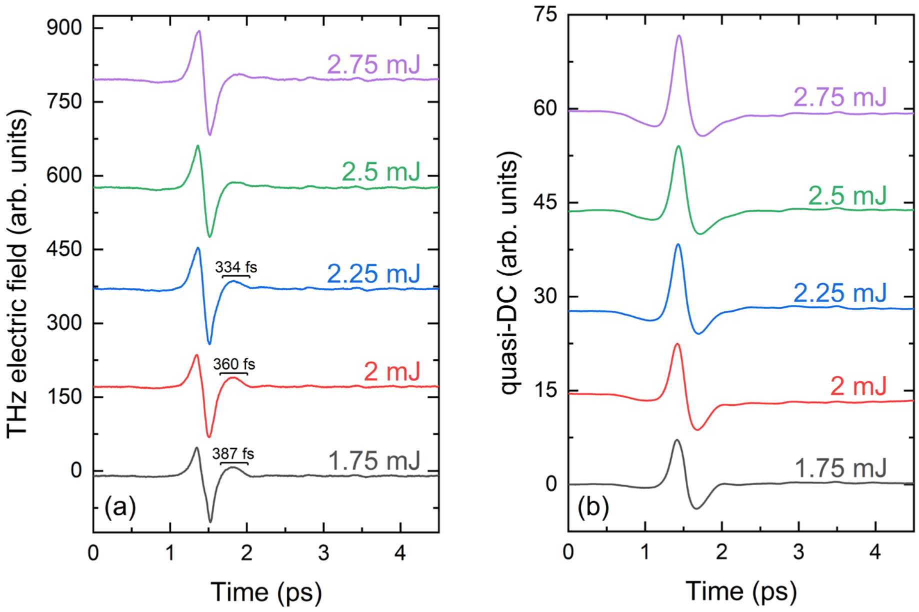

Figure 4.2 (a) THz electric fields recorded through ABCD method for different repetition rates together with different IR pump energy. (b) corresponding quasi-DC temporal distribution obtained by integrating THz waveforms.

By adjusting the IR pumping pulse energy from 1.75 mJ to 2.75 mJ, we obtain the time-domain THz electric field as shown in Fig. 4.2(a). These pulses have typical bipolar waveforms with two sharp peaks followed by a relatively slowly varying peak. In the following, the magnitudes of these peaks are referred to as $E_{\mathrm{p}+}$, $E_{\mathrm{p}-}$, and E_{ps}, respectively. It can be seen that there is no significant change in the temporal width of these positive and negative peaks, nor a temporal shift. But the amplitude ratio $E_{\mathrm{p}+}/E_{\mathrm{p}-}$ increases with the incident power. In addition, when the positive and negative peaks are nearly equal in size, the slowly varying peak E_{ps} almost disappears.

4.3 RECONSIDERATION OF THE PC MODEL

Before discussing why IR pump intensity variations cause shaping of the outgoing THz waveform, we first concentrate on two fundamental questions: why the emitted THz pulse width is much wider than the pump pulse; why the THz waveform is bipolar? These two issues are raised because they arise from experimental observations that are inconsistent with the predictions of the PC model.

The first problem arises from the unique nature of the ABCD method. Since the ABCD method is based on the gaseous medium, there is less absorption of phonon vibration modes and dispersion caused by solid media, thus enabling ultra-wide spectrum measurements. According to the model predictions in Section 2.5, an asymmetric current surge occurs on the time scale of photoionization (for 50 fs pump pulse durations typically <20 fs), and the process can radiate ultra-broadband electromagnetic radiation over 50 THz [3]. However, neither our observations, nor previous studies based on the ABCD method [4–6], show that these detected THz spectral ranges are as broad as predicted by the PC model. Even with 32 fs IR pulsed pumping, only a bandwidth of about 35 THz can be obtained [7]. In our opinion, the model restricts the THz generation process to one pulse period and ignores the complex space-time dynamics of the laser propagation process in the filament. During the focusing process, the density of free electrons near the focal point also varies with the peak intensity, forming a spindle-shaped plasma filament. For a focal length of 150 mm, the laser filament can be extended to several millimeters long (see Fig. 3.4), corresponding to a travel distance of more than 100 pulse widths. With such a large difference in spatial and temporal scales, it is difficult to recognize that THz emission corresponds to transient photocurrents excited only by a single optical pulse cycle at a certain position. It has been suggested by several studies that THz radiation can be coherently superimposed as a set of localized emitters corresponding to the plasma density distribution along the macroscopically observed cumulative ionization trajectories [8–10]. The net current formation during the two-color pulse filamentation and propagation is then likely to be the result of successive ionization events generated over multiple pulse periods. The time derivatives of these long-period current surges correspond to the actual observed THz waveforms. Based on this, the transverse current generated by $t + \mathrm{d}t$ can be rewritten as

$$\mathrm{d}J_{\perp}(t) = -ev_{\mathrm{d}}(t)N_e(t). \tag{4.1}$$

Here, both the photoionized free electron density $N_e(t)$ and the average drift velocity $v_{\mathrm{d}}(t)$ obtained by the electrons are the results in one pulse period T, denoted as

$$v_{\mathrm{d}}(t) = -\frac{e}{m_e}\int_0^T \mathrm{d}E_{\mathrm{L}}(t), \tag{4.2}$$

$$N_e(t) = \int_0^T N_g w(t)\,\mathrm{d}t. \tag{4.3}$$

Although every ionization event along the filament contributes to THz radiation, for a waveform with single-period oscillations, the only part observed is that emitted where $N_e(t)$ or laser intensity changes sharply [11]. In other words, the transverse current generated when the two-color pulse passes through the geometric focal point contributes to the THz waveform formation.

The second question similarly challenges the validity of the PC model under macro conditions. According to the description of Eq. (2.6), the THz field is proportional to the derivative of the quasi-DC density, which corresponds to the instantaneous quasi-DC intensity variation. Given that, the corresponding time-varying quasi-DC can be obtained by integrating the THz waveform in the time domain, as shown in Fig. 4.2(b). We note that these temporal currents show a Gaussian-like distribution, and the current distribution in Fig. 2.8(a) is an error function. In this case, the THz electric field corresponding to its differential function should be a Gaussian function, not a bipolar waveform. This also involves the scaling law controlled by the relative phase of the two-color field. If this phase difference θ is constant as the two-color field propagates through the filament, $J_{\perp}(t)$ should increase monotonously as $N_e(t)$ grows and the mixed field imposes $-y$ acceleration to the ionized free electrons when $\theta = \pi/2$. However, the corresponding time-varying quasi-DC shown in Fig. 4.2(b) implies a weakening or even a negative enhancement. Considering that the photoionization reduction only leads to a slowdown of the quasi-DC variation, the negative peak should be caused by the $-y$ acceleration on free electrons, which suggests a π phase slippage between ω and 2ω caused by the SPM and XPM. This phase shift occurs at least in the time range of the positive and negative peaks, which is about 200 fs. The time scale of this process is relatively short and is unlikely to be a long period variation of the Gouy phase shift or air dispersion. The recent study by Wu et al. provides an important basis for revealing this process. The pre-ionized plasma formed by the high-intensity laser causes a rapid π-shift in the two-color phase difference, resulting in a THz waveform inversion [12,13]. Then the process is similar to the previous chapter described phase slippage due to the refractive index of high-density free electrons, defined as

$$\mathrm{d}\varphi(z) = (2\omega/c)(n_{p,2\omega} - n_{p,\omega})dz, \tag{4.4}$$

where $n_{\mathrm{p},\omega} = 1 - \omega_{\mathrm{p}}^2(z)/2\omega^2$ and $n_{\mathrm{p},2\omega} = 1 - \omega_{\mathrm{p}}^2(z)/8\omega^2$ are the plasma refractive indices of ω and 2ω. With $\omega_{\mathrm{p}}^2 \propto N_e$, we have $\mathrm{d}\varphi(z) \propto N_e(z)$. For the filaments with a several millimeters length should not cause significant differences in group velocity (see details in Appendix), $\mathrm{d}\varphi(z) \propto N_e(z)$ can thus be transformed into $\mathrm{d}\varphi(t) \propto N_e(t)$ by recognizing that $z = ct$. The temporal phase slip along the entire laser filament is noted as

$$\theta(t) = \theta_0 + \Delta\varphi(t), \tag{4.5}$$

where θ_0 is the initial relative phase and $\Delta\varphi(t) = -\int_{t_0}^{t} d\varphi(t) \propto -\int_{t_0}^{t} dN_e(t)$ is the time-varying additional relative phase induced by free electrons. According to our modified macroscopic PC model, the THz field is re-expressed as the derivative of the long-period time-varying current in the filament

$$E_{\mathrm{THz}} \propto \mathrm{d}J_{\perp}(t)/\mathrm{d}t = -ev_d(t)N_e(t)/\mathrm{d}t. \tag{4.6}$$

4.4 THZ WAVEFORM MODULATED BY ADDITIONAL PHASE SLIPPAGE

According to Eq. (4.2), (4.3), and (4.6), if we obtain the temporal intensity distribution $I_{\mathrm{pump}}(t)$ of the two-color pulses near the focal point, we can estimate the free electron density distribution $N_e(t)$ and its average drift velocity $v_d(t)$ correspondingly. However, the complete extraction of the spatio-temporally varying $I_{\mathrm{pump}}(t)$ is quite difficult, since a full theoretical consideration of the filament internal dispersion requires extremely laborious numerical simulations of the propagation process. Taking this into account we consider $I_{\mathrm{pump}}(t)$ at the focal point as a temporal normal distribution comparable to the width of the detected THz pulse. Hence, the waveform modulation due to phase change can be effectively described by a simpler approximation. We define $v_d(t) = v_{\max}(I_{\mathrm{pump}}, t) \cdot \sin[\theta_0 + \Delta\varphi(t)]$, where $v_{\max}(I_{\mathrm{pump}}, t)$ is the maximum speed that the electron obtains when the phase is optimally matched at time *t*. Consequently both $v_d(I_{\mathrm{pump}}, t)$ and $N_e(I_{\mathrm{pump}}, t)$ can be approximated as normally distributions over time, and $\Delta\varphi(t)$ is then the cumulative distribution function that varies with $-\int_{t_0}^{t} \mathrm{d}N_e(t)$ from π to $-\pi$. Here, the total phase slip is not π but 2π by considering the current distribution also has some negative values before the peak shown in Fig. 4.2(b). With the opinion of that the experiment of Wu et al. where the two-color pulses were passed through the side of a pre-ionized filament, corresponding only to the ionization event at the focal point. In contrast, the case of SPM and XPM propagates throughout the whole filament, where each ionization event contributes to the additional refractive index, so we considered a larger range of phase modulation. The functions we use for calculation is expressed as follows

$$v_{\max}\left(I_{\text{pump}},t\right) \propto \exp(-t^2), \tag{4.7}$$

$$N_e\left(I_{\text{pump}},t\right) \propto \exp(-t^2), \tag{4.8}$$

$$\theta(t) = \theta_0 + \varDelta\varphi(t) = \theta_0 - \pi\,\text{erf}(t) = \theta_0 - \sqrt{\pi}\int_{-\infty}^{t}\exp(-t'^2)dt', \tag{4.9}$$

$$E_{\text{THz}} = \sin[\theta(t)]\cdot N_e(I_{\text{pump}},t)\cdot v_{\max}\left(I_{\text{pump}},t\right). \tag{4.10}$$

Setting the initial phase θ_0 from -0.5 to $+0.5$, the THz electric field calculated by Eqs. (4.7) to (4.10) is shown in Fig. 4.3. These waveforms exhibit the characteristic that the positive peak decreases with the initial phase, while the negative peak increases. And when the initial phase is 0, it shows a symmetrical bipolar waveform (see Fig. 4.3(f)). In other words, the ratio of $+y$ and $-y$ acceleration for phase control also determines the ratio of $E_{\text{p}+}/E_{\text{p}-}$ in the THz waveform. If $\sin\theta(t)$ has negative at the peak of the normal distribution (Fig. 4.3(g) ~ (k)), it shows a negative peak in the THz waveform, and vice versa (Fig. 4.3(a) ~ (e)). Therefore, for our experimental conditions, the intensity-dependent initial phase $\theta_0(I_{\text{pump}})$ causes THz waveform shaping. We extracted the experimental amplitude ratio $E_{\text{p}+}/E_{\text{p}-}$ for each waveform in Fig. 4.2(a), indicated in the black squares in Fig. 4.4. According to the experimental results in Section 3.4, the intensity-dependent phase $\theta_0(I_{\text{pump}})$ varies linearly. On this assumption, the calculated continuous amplitude ratio variation trend is shown in the red solid line and agrees well with the experimental observations.

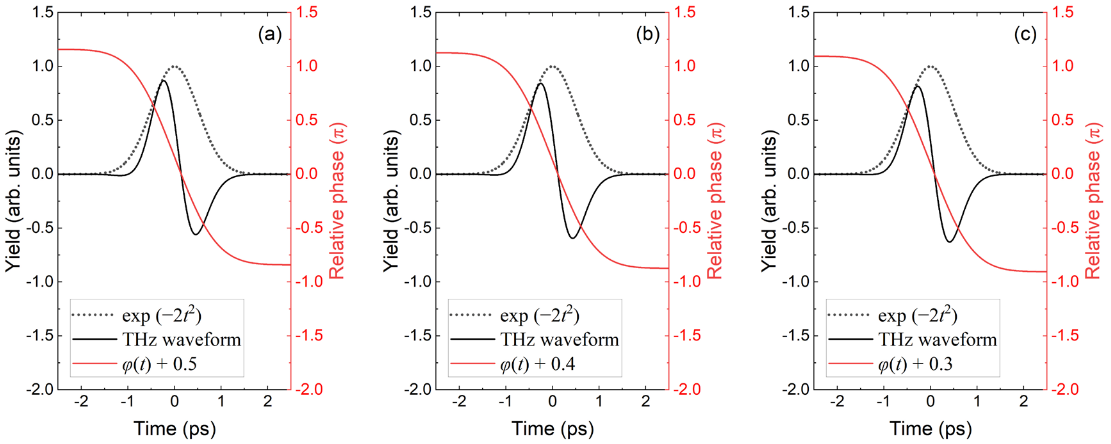

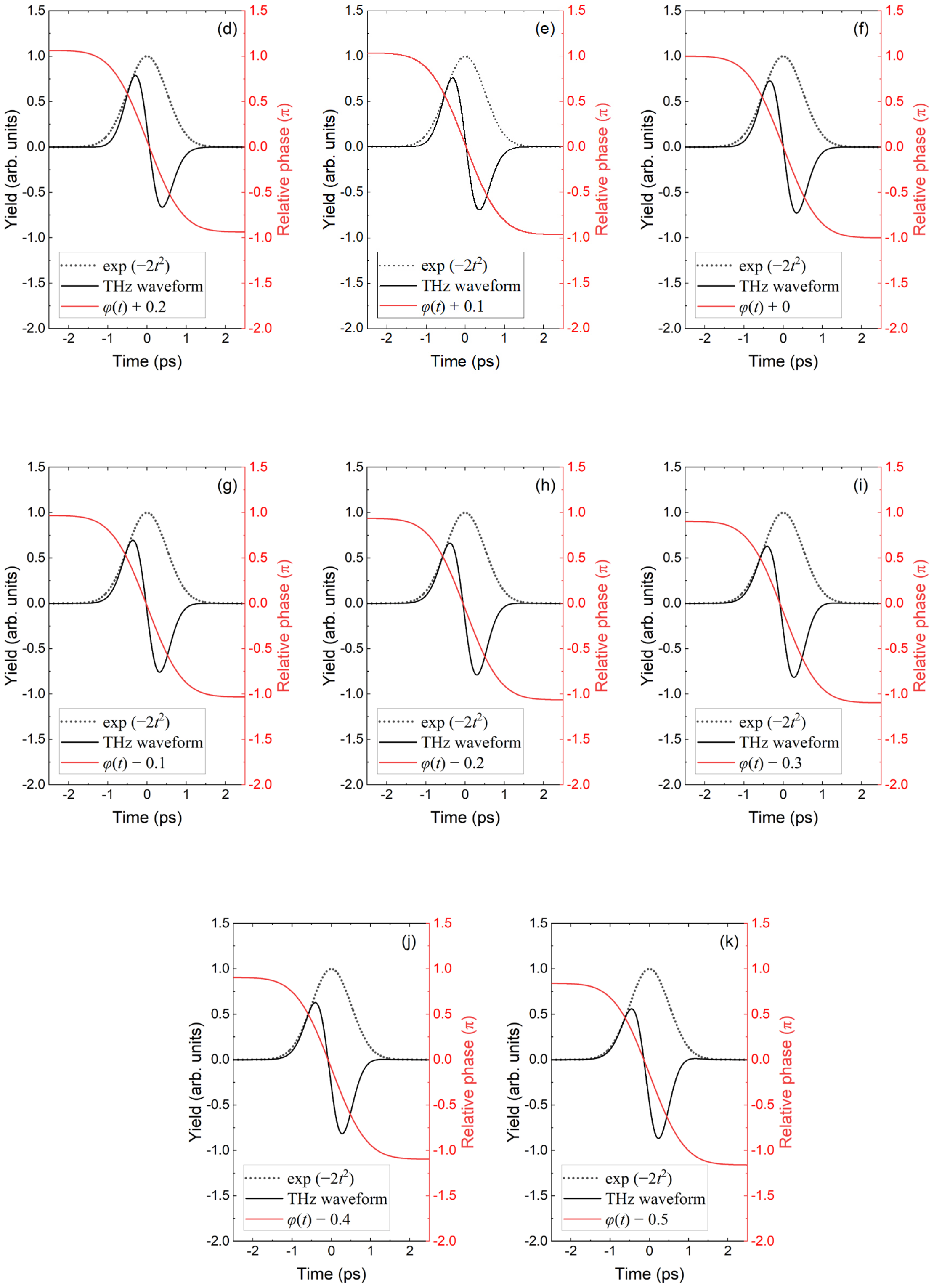

Figure 4.3 Calculated THz time-domain electric fields (black solid line, left ordinate axis) by Eq. (4.10) with initial phases of $\theta_0 = -0.5 \sim 0.5$ (a)~(k). The corresponding time-varying phase change $\theta(t)$ is obtained by Eq. (4.9) (red line, right ordinate axis). The product of normal temporal

distributed maximum electron velocity $v_{\max}(I_{\text{pump}}, t)$ and the electron density $N_e(I_{\text{pump}}, t)$ obtained by Eq.(4.7) and (4.8) respectively (black dots, left ordinate axis).

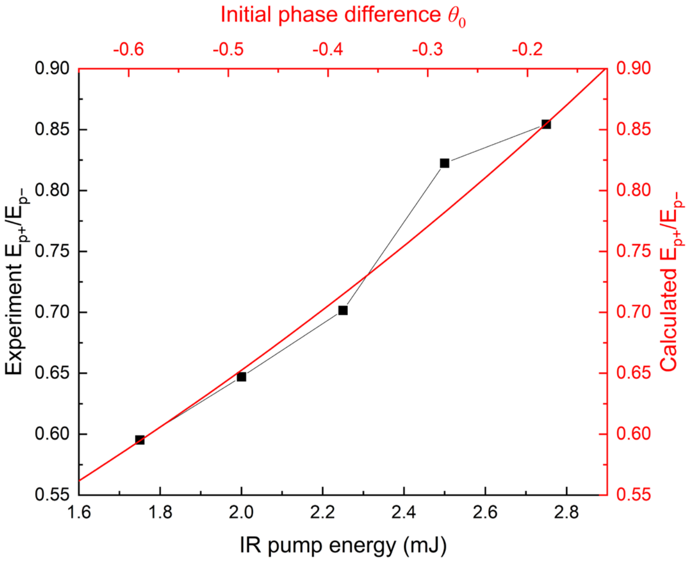

Figure 4.4 Magnitude ratio of the positive peak $E_{\text{p}+}$ to the negative peak $E_{\text{p}-}$ varies incident IR energy I_{pump} (black squares, left and down ordinate axis) and calculated results versus linear initial phase θ_0 (red line, right and up ordinate axis).

4.5 ORIGIN OF ADDITIONAL PHASES AND SMOOTHING PEAKS

Although we have made it clear in Chapter 3 that the phase slip of the two-color field inside the filament comes from the contribution of the plasma refractive index. However, the π-integer times' phase slip near the focal point will only result in the inversion of the THz waveform and will not affect the amplitude. A question then naturally arises: where does this intensity-dependent phase slip originate?

THz beam pattern is affected by the plasma geometry or spatial distribution of free electron density. However, the THz spot change necessarily causes an additional optical path length, resulting in a peak time shift. In Fig. 4.2(a), no significant shift in the peak position of the waveform occurs, indicating that the THz directional map is not changed. We used an uncooled microbolometer-based THz imager (NEC IRV-T0832) to record the THz beam pattern as shown in Fig. 4.5 (a) at the ~10 mm in front of the focal plane of PM2. The images consist of 360 × 240 pixels and each pixel size is 23.5 μm. The spatial distribution is almost unchanged as shown in Fig. 4.5 (b) and (c). Therefore, the change in the temporal profile affected by THz radiation pattern is negligible in our experimental implementation.

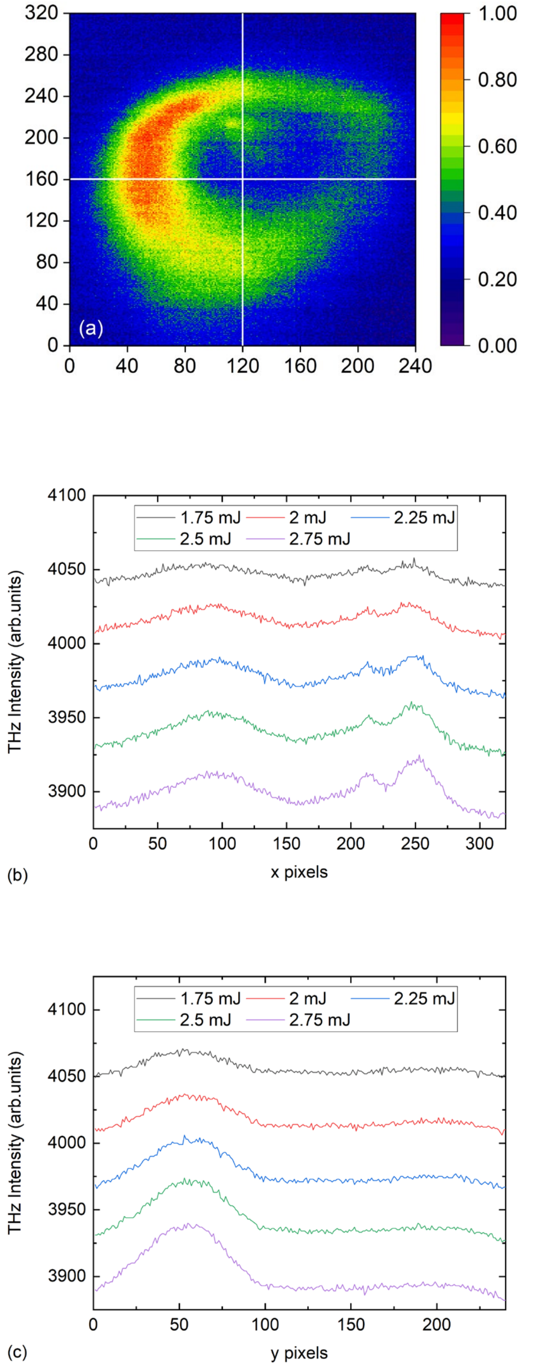

Figure 4.5 (a) Image of a THz radiation pattern captured at ~10 mm in front of the focal plane of PM2 by a THz camera (microbolometer detector array); Corresponding midline profile with different pump energy at $y = 160$ (b) and $x = 120$ (c).

For weakly ionized gas media, the collisional absorption and electron cyclotron resonance may cause plasma absorption [14], which seems to be a possible reason. However, these absorptions usually occur on the scale of several centimeters and are more pronounced in the lower frequency bands below the plasma frequency [15]. Under our experimental conditions, the negligible plasma absorption due to the propagation distance of several millimeters at atmospheric pressure is not of main relevance for our results. Also, we did not observe significant spectral changes in the low frequency.

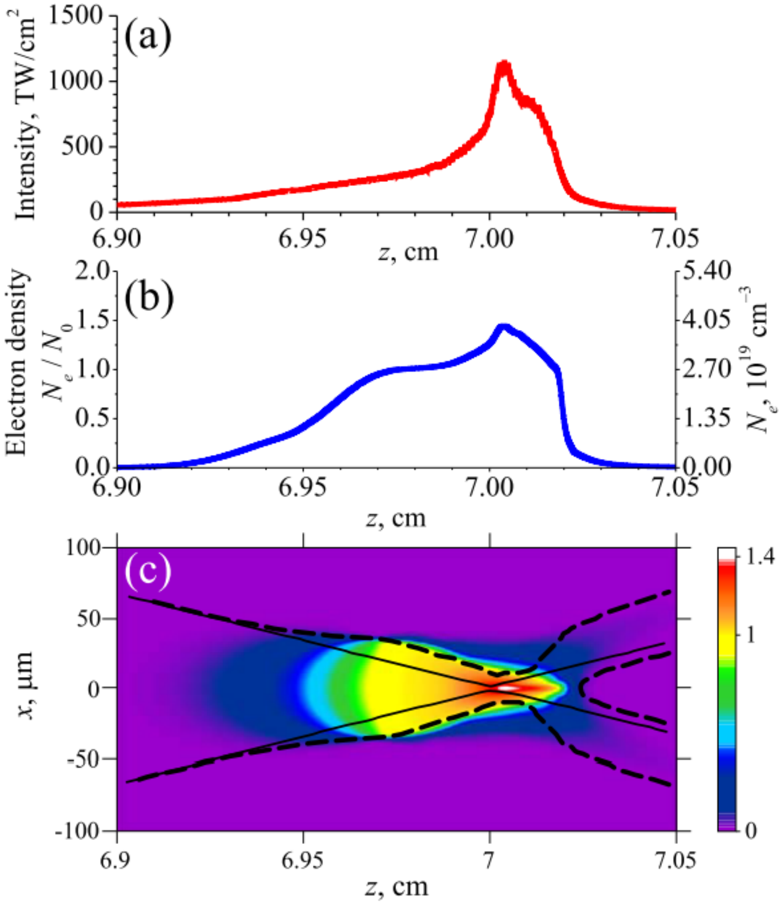

Figure 4.6 Simulated dependencies of (a) laser peak intensity and (b) plasma density on the propagation distance *z* with focal length *f* = 7cm. (c) The longitudinal section of the plasma channel. Solid black indicates the FWHM level of laser beam fluence in the linear propagation case and dashed black line—in line simulations (reprinted from [16]).

Recent simulation results provide a unique perspective that seems to reasonably explain the origin of θ_0. To estimate the variation of intensity and plasma density with shortening of the focus length, Mokrousova et al. used the unidirectional pulse propagation equation (UPPE) to simulate the pulse propagation at a positive lens focal length of 7 cm pieces [16]. The simulation results show that the length of the filament with an intensity above 100 TW/cm^2 lasts about 1 mm (see Fig. 4.6(a)). And those parts where the intensity changes drastically (6.99 ~ 7.02 cm), by converting to the time domain which is close to our measured THz pulse width (~1 ps). However, the electron density does not increase sharply like intensity, but forms a relatively smooth distribution in front of the focal point. However, the electron density does not increase as sharply as intensity, but forms a relatively smooth distribution in front of the focus (see Fig. 4.6(b)). We inclined to the view that the phase-modulated by the I_{pump} is likely to originate with those electron densities in front of the focus. The more drastic changes in N_e near the focus are responsible for the large and fast phase slip. After the geometrical focus, both intensity and N_e rapidly decrease down to almost zero due to both the divergence and nonlinear defocusing in the filament. It is worth noting that the magnitude and linearity of the phase slip we calculated are also close to the experimental results in Chapter 3. This suggests that these phenomena are likely to all originate from the same reason.

However, it also raises a new problem for the explanation of E_{ps} at the tail. Our calculation results do not show an obvious protrusion after the negative peak as observed in the experiment. Considering that the femtosecond laser pulse duration used in practice is much longer than the mean free time of the ionized electrons, quasi-DC attenuation due to collisions of the free electrons with surrounding molecules or ions are typically ignored. We mentioned the absorption effect due to free-electron collisions in Section 2.3. Although we neglect these absorptions under the effect of a strong electric field, the momentum transfer collisional effects are the main cause of current attenuation. Once the electric field disappears, no ionization events can significantly affect the current distribution anymore, so the electrons keep their velocity to form a non-vanishing current. The mean free time of a free electron is given by the formula [17]

$$(\Delta t)_{\mathrm{mean}} = 1/\sigma N_g v_e \quad . \tag{4.11}$$

For the laser intensity of ~10^{13} W/cm^2, nonrelativistic velocity is thus $v_e \sim 4.5 \times 10^7$ cm/s. With neutral gas density $N_g \sim 2.68 \times 10^{19}$ cm^{-3} and the electron-neutral collision cross-section $\sigma \sim 10^{-15}$ cm^2, we obtain $(\Delta t)_{\mathrm{mean}} \sim 300$ fs. The measured duration of E_{ps} shown in Fig. 4.4(a) is slightly longer than the calculated $(\Delta t)_{\mathrm{mean}}$, and they decrease with increasing I_{pump}. It can be considered as a decline in the residual current due to an additional phase, that is, a decreasing v_e of electrons.

4.6 CONCLUSION

In this chapter, we show that the THz waveform emitted by a two-color laser field from a gas filament is intrinsically linked to the input infrared energy, and speculate that it may be related to the nonlinear effects introduced by the intensity. However, the microscopic PC theoretical model does not match the experimental observations either in terms of THz pulse width or waveform. Based on the coherent superposition of the THz emission originating from the equivalent line source on the filament, we attribute the THz waveform formation to a long period quasi-DC surge by adding multiple photoionization events rather than limiting them within a pulse duration. And according to recent studies, the drastic change in plasma density at the center of the focus leads to a π-phase shift between the two-color fields, resulting in a bipolar THz waveform.

By assuming that the intensity of the optical field at the focal point is temporal-Gaussian distributed, we calculate that the initial phase before the fast phase slip modulates the output THz waveform. Although such a simple model does not involve higher-order nonlinearity, optical pulse distortion, qualitative dynamics, or THz absorption, it can explain the phase-dependent waveform shaping well and is consistent with experimental results. This phenomenon is attributed to the fact that as the pumping energy increases, the surrounding low-density electrons gradually affect the initial phase, resulting in waveform shaping. And the slowly changing peak in the tail is caused by the residual current decay. We hope that this study will help those working with broadband THz sources and systems to better understand the generation mechanisms and provide a way to control THz waveforms.

REFERENCES:

1. D. H. Auston, K. P. Cheung, and P. R. Smith, "Picosecond photoconducting Hertzian dipoles," Appl. Phys. Lett. **45**, 284–286 (1984).
2. N. Karpowicz, J. Dai, X. Lu, Y. Chen, M. Yamaguchi, H. Zhao, X.-C. Zhang, L. Zhang, C. Zhang, M. Price-Gallagher, C. Fletcher, O. Mamer, A. Lesimple, and K. Johnson, "Coherent heterodyne time-domain spectrometry covering the entire "terahertz gap,"" Appl. Phys. Lett. **92**, 011131 (2008).
3. K.-Y. Kim, "Generation of coherent terahertz radiation in ultrafast laser-gas interactions," Phys. Plasmas **16**, 056706 (2009).
4. F. D'Angelo, Z. Mics, M. Bonn, and D. Turchinovich, "Ultra-broadband THz time-domain spectroscopy of common polymers using THz air photonics," Opt. Express **22**, 12475 (2014).
5. J. Liu and X. C. Zhang, "Terahertz radiation-enhanced-emission-of-fluorescence," Front. Optoelectron. **7**, 156–198 (2014).
6. X. Lu and X. Zhang, "Investigation of ultra-broadband terahertz time-domain spectroscopy with terahertz wave gas photonics," Front. Optoelectron. **7**, 121–155 (2014).
7. I.-C. Ho, X. Guo, and X.-C. Zhang, "Design and performance of reflective terahertz air-biased-coherent-detection for time-domain spectroscopy," Opt. Express **18**, 2872 (2010).
8. Y. S. You, T. I. Oh, and K. Y. Kim, "Off-axis phase-matched terahertz emission from two-color laser-induced plasma filaments," Phys. Rev. Lett. **109**, 183902 (2012).
9. A. Gorodetsky, A. D. Koulouklidis, M. Massaouti, and S. Tzortzakis, "Physics of the conical broadband terahertz emission from two-color laser-induced plasma filaments," Phys. Rev. A - At. Mol. Opt. Phys. **89**, 1–6 (2014).
10. Z. Zhang, Y. Chen, M. Chen, Z. Zhang, J. Yu, Z. Sheng, and J. Zhang, "Controllable Terahertz Radiation from a Linear-Dipole Array Formed by a Two-Color Laser Filament in Air," Phys. Rev. Lett. **117**, 243901 (2016).
11. P. A. Chizhov, A. A. Ushakov, V. V. Bukin, and S. V. Garnov, "Terahertz radiation from extended two-colour air filaments," Laser Phys. Lett. **16**, 075301 (2019).
12. T. Wu, L. Dong, S. Huang, R. Zhang, S. Zhang, H. Zhao, C. Zhang, Y. Zhao, and L. Zhang, "Excitation-wavelength-dependent terahertz wave modulation via preformed air plasma," Appl. Phys. Lett. **112**, 171106 (2018).
13. T. Wu, L. Dong, S. Zhang, H. Zhao, K. Kang, C. Zhang, R. Zhang, Y. Zhao, and L. Zhang, "Modulation of terahertz wave generation from laser-induced filament based on a preionized plasma," Opt. Commun. **444**, 137–141 (2019).

14. C. Yuan, Z. Zhou, X. Xiang, H. Sun, and S. Pu, "Propagation of broadband terahertz pulses through a dense-magnetized- collisional-bounded plasma layer," Phys. Plasmas **17**, (2010).
15. J. X. Liu, L. H. Meng, Y. J. Liu, J. L. Feng, and H. W. Yang, "Study of the Absorption Properties of Terahertz Wave in the Plasma Medium," Zeitschrift fur Naturforsch. - Sect. A J. Phys. Sci. **74**, 1031–1036 (2019).
16. D. V. Mokrousova, S. A. Savinov, L. V. Seleznev, G. E. Rizaev, A. V. Koribut, Y. A. Mityagin, A. A. Ionin, I. A. Nikolaeva, D. E. Shipilo, N. A. Panov, A. A. Ushakov, A. B. Savel'ev, O. G. Kosareva, and A. P. Shkurinov, "Tracing Air-Breakdown Plasma Characteristics from Single-Color Filament Terahertz Spectra," J. Infrared, Millimeter, Terahertz Waves **41**, 1105–1113 (2020).
17. S. L. Chin, "Femtosecond Laser Filamentation," in *Springer-Verlag New York* (2010), pp. 11–48.

Chapter 5. **OPTICAL CHARACTERIZATIONS OF CYCLIC OLEFIN POLYMERS BY USING A TWO-COLOR LASER FILAMENT SOURCE**

5.1 INTRODUCTION

Although the most advanced emerging THz technologies, including spectroscopy devices and imaging systems, have been developed significantly, such applications remain challenging because THz waves are strongly attenuated by the presence of water (H_2O) in the atmosphere. For the next-generation mobile communication technology that has begun to advance globally, THz waves will undoubtedly be the waveband of choice for the development of "6G" to push the limit of transmission bandwidth even higher. However, when preparing THz waveguide chips, the use of conventional methods is susceptible to signal loss caused by the loss of substrate materials. In addition, with the booming research interesting on THz nonlinear effects, applied optic components such as lenses, cuvettes, etc. in the THz band also need to have extremely low absorption and dispersion at wider bands.

Hydrocarbon polymer materials are preferred as engineering plastics because of their high transparency, thermal stability, chemical resistance, and low moisture absorption. Copolymerization of bulky cyclic olefins with simple olefins is a promising approach to obtain the corresponding polymeric materials, so-called cyclic olefin copolymers (COCs, see Fig. 5.1(a)), with the great advantage of low-cost starting olefin monomers [1]. Conversely, ring-opening complex decomposition polymerization (ROMP, see Fig. 5.1(b) and (c)) can be another complex approach by applying olefin ring monomers with bulky substituents [2,3]. COC/COP materials possess many unique properties: These amorphous endocyclic compounds highly transparent in the visible range, lightweight because of their low specific gravity, exhibit good mechanical strength, show only a slight deterioration due to moisture, and have a high glass transition temperature depending on the chain structure. They are non-polar polymers and therefore have low absorption of water vapor and chemical resistance to acids and polar solvents, which makes them compatible with common photolithographic etching methods. [4]. A number of recent applications based on this material in the THz band have made them notable. Such as broadband mesh filters and single-mode flexible fibers [5,6]. The microstrip line waveguide on a COC substrate has achieved a low loss of 0.9 dB/mm at 170 GHz [7].

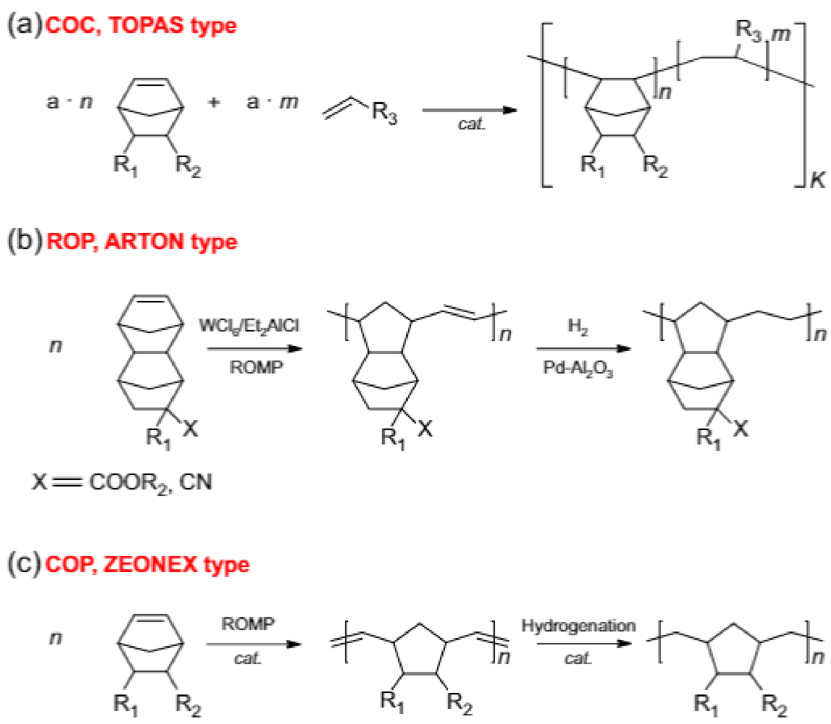

Figure 5.1 General synthesis for cyclo olefin copolymers. (a) Topas type, ring opening polymers (ROP). (b) Arton type and cyclo olefin polymers. (c) Zeonex type. (Reprinted from [6])

This chapter serves as an example of the application of broadband, intense THz sources of two-color laser filament. In this chapter, we characterize the dispersion and dielectric properties of COPs materials and other amorphous materials by using transmission THz-TDS experiments. The comparison among these substrates with theoretical analysis methods should provide insight to verify the availability of COC/COP as an option for the THz band. We demonstrated that COPs have rarely low dielectric loss and flat dispersion over 4 THz bandwidth, these unique characteristics provide an exciting opportunity to meet multiple aspects of THz applications.

5.2 SAMPLES AND EXPERIMENTAL SETUP

The neat samples were prepared by taking commercially available polymer plates from chemical distributors. Fig. 5.2 lists these samples with photos, brand, model, and manufacturer information. Except for fused silica, which is 1 mm thick, all other materials are 2 mm thick. Type RS420 COP is a white opaque solid material which has been designed for the usage of circuit substrates, and type E480 and 480R COP are colorless transparent solids expected for making lenses and sample cells.

The dielectric properties of COPs in the THz region had been investigated systematically by using the transmission THz-TDS method at room temperature (~293K). We used the air-based TDS system which is the same setup as described in section 4.2. To eliminate the absorption of vapor, the THz beam pathway was completely purged with dry nitrogen to keep the humidity less than 5%. The usable frequency band was from 0.5 to 4 THz, but the valid range tended to decrease due to signal attenuation by the samples.

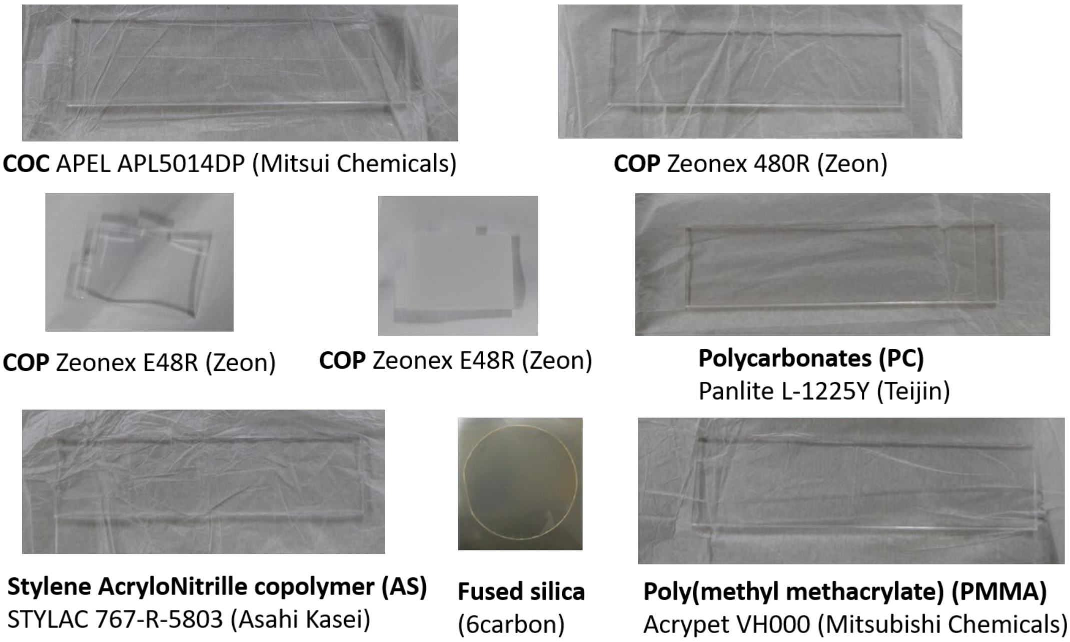

COC APEL APL5014DP (Mitsui Chemicals)

COP Zeonex 480R (Zeon)

COP Zeonex E48R (Zeon)

COP Zeonex E48R (Zeon)

Polycarbonates (PC)
Panlite L-1225Y (Teijin)

Stylene AcryloNitrille copolymer (AS)
STYLAC 767-R-5803 (Asahi Kasei)

Fused silica
(6carbon)

Poly(methyl methacrylate) (PMMA)
Acrypet VH000 (Mitsubishi Chemicals)

Figure 5.2 Photograph of the sample to be tested. Material names are shown in bold font; trade names and models are shown in normal font; manufacturer is shown in brackets at the end.

5.3 ANALYTICAL METHODS

The optical characteristic of the samples was analyzed by measuring electric fields of the THz pulses with and without the sample in the time-domain. Then the frequency-dependent spectrum was obtained by performing a fast Fourier transform (FFT) on the measured time-domain data. The complex transmittance $\widetilde{H}(\omega)$ of the ratio between sample spectrum and reference spectrum was used for obtaining the refractive index $\tilde{n}(\omega)$ [8]:

$$\widetilde{H}(\omega) = T(\omega)e^{-i\phi(\omega)} = \frac{4\tilde{n}(\omega)}{[1+n(\omega)]^2}\exp\left\{-i\omega d\left[\frac{\tilde{n}(\omega)-1}{c}\right]\right\}, \tag{5.1}$$

where d is the thickness of the sample, $T(\omega)$ and $\phi(\omega)$ are the amplitude and phase of $\widetilde{H}(\omega)$. Eq. (5.1) assumes a plane wave entering an isotropic and homogeneous medium with normal incidence. The macroscopic optical properties can generally be expressed by the following complex index of refraction

$$\tilde{n}(\omega) = n(\omega) - i\kappa(\omega)\,, \tag{5.2}$$

where $n(\omega)$ and $\kappa(\omega)$ represent the real part and imaginary part (or extinction coefficient) of the complex refractive index $\tilde{n}(\omega)$. They describe the dispersion and absorption characteristics of the sample, which can be further worked out as follows

$$n(\omega) = 1 + \frac{c}{\omega d}\,\phi(\omega), \tag{5.3}$$

$$\kappa(\omega) = \frac{c}{\omega d}\ln\left[\frac{4n(\omega)}{[n(\omega)+1]^2|T(\omega)|}\right]. \tag{5.4}$$

For a non-magnetic material, the permittivity is defined as:

$$\tilde{\varepsilon}(\omega) = \varepsilon'(\omega) - i\varepsilon''(\omega)\,. \tag{5.5}$$

Then we can calculate the loss tangent related to the dielectric loss caused by the dipole polarization and ionic conductance of the dielectric medium. As the frequency increases, the dipole motion of the molecules inside the material is affected by the surrounding viscous damping, which leads to the delay between the polarization and electric field. The electric field forces the dipole to rotate, consuming electrical energy to overcome the internal viscous resistance of the dielectric. The conversion of electromagnetic wave energy into thermal energy causes dielectric losses. The loss angle tangent of the substrate material is a measure of this loss and is expressed as

$$\tan\delta = \frac{\varepsilon'(\omega)}{\varepsilon''(\omega)}\quad. \tag{5.6}$$

5.4 RESULTS AND DISCUSSIONS

The refractive index and extinction coefficient of each sample is shown in Fig.5.3. Although these samples are very similar in Fig. 5.2, the optical properties in the THz band are quite different from each other. The refractive indices of COC, PC, and AS all increase with frequency, but the extinction coefficients of COC are quite smaller in comparison with others. Both PC and AS have considerable absorption, and PC even has a characteristic peak at 1.5 THz. The refractive index of PMMA decreases with frequency and exhibits anomalous dispersion characteristics. This behavior seems to originate from the bosonic peak caused by the vibrational properties of the glassy state. The bosonic peak is an intrinsic feature of non-static matter, which is associated with a relative excess of vibrational modes [9]. The alternating polarization of molecules inside the dielectric and the energy dissipation by lattice collisions also cause absorption. In addition, there seems to be significant absorption and dispersion near 0.5 THz and resonance peaks near 3.75 THz and 4.0 THz. Given that they are not the focus of this chapter, we did not analyze them in more depth. The refractive indices of fused silica and COPs are almost constant throughout the tested frequency band. This property is important for the application of THz lenses and cuvettes.

Especially for lenses, it is important to ensure the relationship between the geometric focus and the incident surface. If the dispersion characteristics are too complex in the several THz ranges, it will undoubtedly complicate the design for THz optical applications.

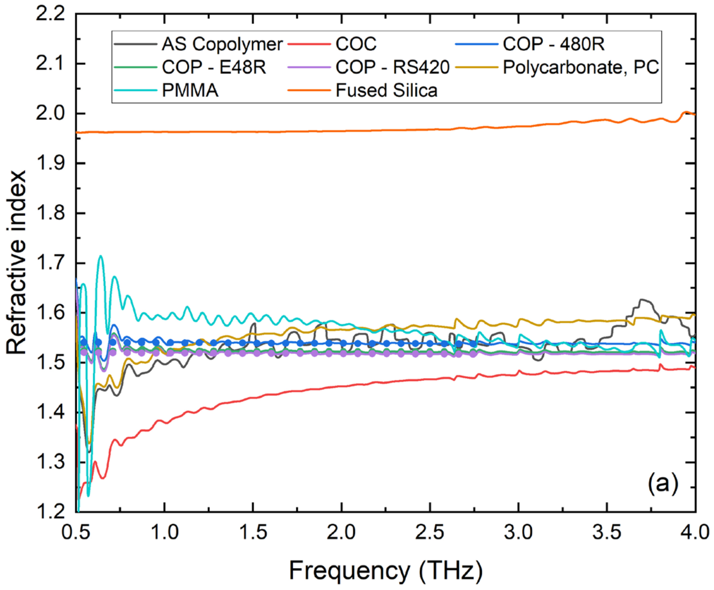

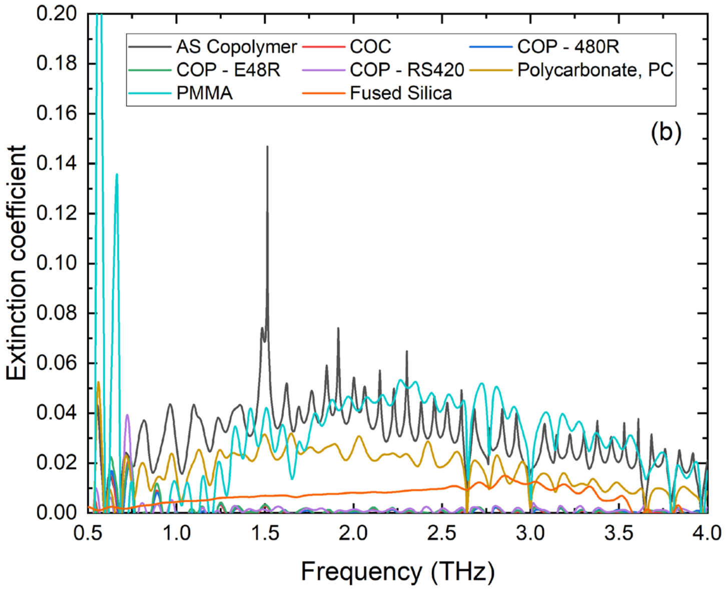

Figure 5.3 Refractive index (a) and extinction coefficient of (b) each sample. Dots in (a) are the results measured by a PCA-based low-intensity THz source.

Another problem for THz lenses is the nonlinear effect, which can also affect the performance of the lens if the refractive index of the material itself changes under high-intensity

THz irradiation. As a complementary test, we measured the refractive index of three COP materials using a weak THz source emitted from a PCA antenna, and the results were almost indistinguishable from those at an air plasma emission source (THz power of about 0.25 mW). This assures that COP materials can be used in any situation in THz optics.

5.5 SUBSTRATE LOSS CHARACTERIZATION FOR THZ TRANSMISSION LINES

For high-speed communications, the development of THz-band waveguides is very important. In addition, it can also be used for another application: an on-chip THz-TDS system. This functional systems integrated the photoconductive generation and detection of pulsed THz waves with the metal transmission lines formed by lithography and surface metallization [10,11]. They have several advantages in comparison with free-space THz-TDS techniques. The small size of the spectrometer makes it ideal for studying different samples in a convenient place instead of transporting them to the laboratory. Compared with the traditional free space setting of the THz-TDS system, the design of the spectrometer concentrates the THz radiation into a smaller volume, which will improve the analytical sensitivity and reduce the absorption by water in the atmosphere since electric fields are mostly confined around the transmission line. Low cost emphasizes "use and throw away", while making the spectrometer suitable for a wider range of users, where doctors in healthcare clinics and hospitals, airport security can afford it

Table 5.1 List of samples and their optical parameters at 1 THz.

Sample		Transmittance	Refractive index	Real permittivity	Imaginary permittivity	Loss tangent
COP	480R	94.5%	1.523	2.320	0.0010	4.31×10^{-4}
	E48R	92.2%	1.540	2.372	0.0014	1.08×10^{-4}
	RS420	94.0%	1.519	2.31	0.0025	5.99×10^{-4}
PMMA		65.5%	1.611	2.593	0.1098	4.24×10^{-2}
Fused silica		80.6%	1.963	3.853	0.0190	4.94×10^{-3}
COC		94.3%	1.453	2.116	0.0025	3.78×10^{-4}
PC		88.0%	1.480	2.189	0.0286	1.31×10^{-2}
AS		31.0%	1.497	2.239	0.0787	3.51×10^{-2}

To capitalize on the advantages of on-chip THz-TDS, the designs of transmission line make a great difference. Especially, as an important component of the transmission line, the dielectric substrate has a great influence on the transmission line losses. The losses affected by the substrate mainly consist of two parts, one of which is the dielectric loss caused by the dipole polarization and ionic conductance of the substrate material, the other is the radiation loss due to the large difference in the dielectric constant between the substrate and the air, with which the electromagnetic energy on the transmission line is radiated to the substrate as a shock-wave [12]. Table 5.1 summarizes the results for the extracted transmittance, refractive index, dielectric constant, and the loss tangent of each sample at 1THz.

Based on the experimental results, we analyze the different types of losses caused by the substrate material which can help to optimize the transmission line structure including its substrate and dimensions. We consider the dielectric loss caused by polarization relaxation first. For the example of coplanar waveguide (CPW), a THz wave is transmitted through a dielectric material, the intrinsic dipole moment is forced to vibrate and part of the electromagnetic wave energy is consumed in the form of heat. The dielectric loss can be expressed as [13]

$$\alpha_d = \frac{27.3\varepsilon\prime(\omega)\cdot(\varepsilon_{eff}-1)\tan\delta}{\sqrt{\varepsilon_{eff}}\,[\varepsilon'(\omega)-1]}\cdot\frac{\omega}{2\pi} \quad , \tag{5.7}$$

where ε_{eff} is the effective dielectric constant of CPW:

$$\varepsilon_{eff} = \frac{\varepsilon'(\omega)+1}{2}\cdot\frac{K(k')}{K(k)}\frac{K(k_1)}{K(k_1')}. \tag{5.8}$$

The parameters are as follows: $k = s/(s+2W)$, $K(k)$ is the complete elliptic integral of the first kind, and $k' = \sqrt{1+k^2}$; $k_1 = \sinh(\frac{\pi s}{4h})/\sinh[\frac{\pi(s+2W)}{4h}]$; W, s and h are geometric parameters related to the waveguide structure as demonstrated in Fig. 5.4.

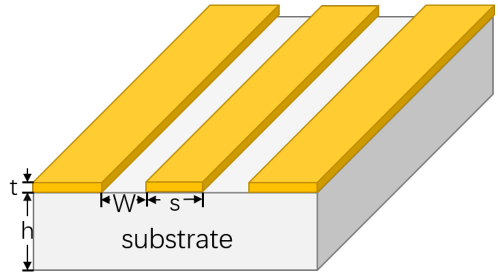

Figure 5.4 Schematic diagram of coplanar waveguide structure and parameters.

Another attenuation affected by the substrate is the radiation loss caused by the permittivity mismatch between the substrate and air. When the group velocity of THz radiation is larger than the phase velocity, ultra-short electric pulse propagated in the semi-infinite dielectric substrate of the metal transmission line will produce the reverse-cone Cherenkov electromagnetic shock wave, which causes the dissipation of the THz pulse energy [12]. The radiative losses are dominant for frequencies over 200 GHz with a cubic frequency f^3 dependence under quasi-static approximations [17]. The radiation loss formulas of CPW are expressed by [14]:

$$\alpha_{r,\text{CPW}} = \left(\frac{\pi}{5}\right)^2 2\left[\left(1-\frac{\varepsilon_{eff}(f)}{\varepsilon_r}\right)^2 \Big/ \sqrt{\frac{\varepsilon_{eff}(f)}{\varepsilon_r}}\right]\frac{(s+2W)^2\varepsilon_r^{3/2}}{c^3K(k')K(k)} f^3. \tag{5.9}$$

We take COPs, PMMA and fused silica as examples with relatively smooth dispersion properties in the THz band. The dielectric parameters of each material are substituted into Eq. (5.7) and (5.9) to obtain their dielectric and radiation losses, as shown in Fig. 5.5. The COP material has lower losses than the other materials when used as a substrate for CPW.

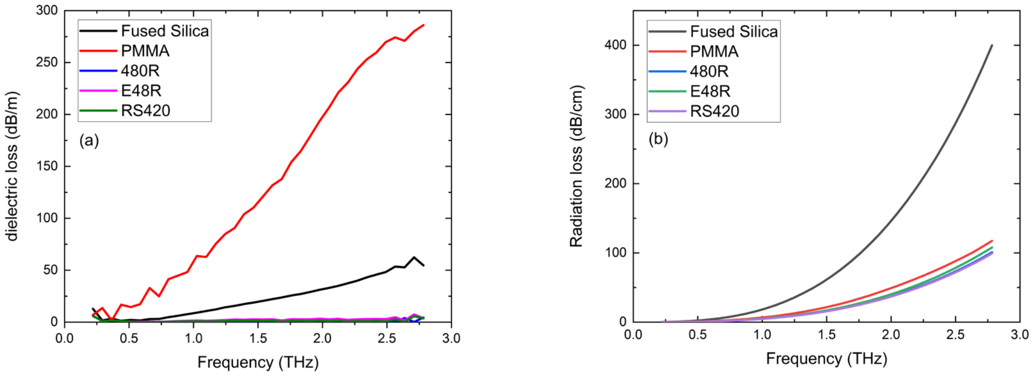

Figure 5.5 (a) Dielectric loss (b) and radiation loss (CPW) of each material

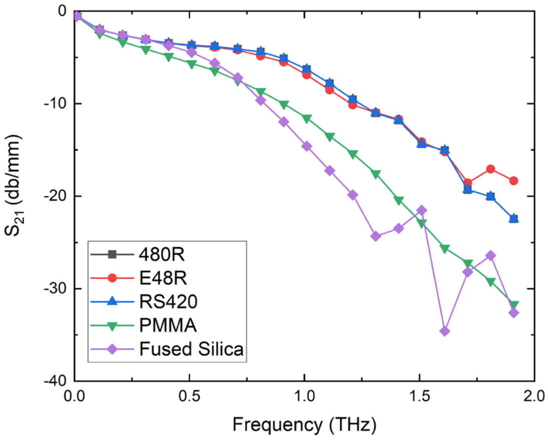

Figure 5.4 S_{21} parameters obtained from finite element simulation of CPW deposited on each material

To understand in detail the transmission characteristics of THz transmission lines when using individual materials as substrates, we solve for the fields and propagation modes within the transmission line structure based on the finite element method. The loss of the transmission line system is illustrated by the forward transmission parameter S_{21}. S_{21} is the logarithmic ratio of output to input power measured in decibels (dB), where 0 dB indicates lossless transmission and

−dB values indicate signal loss during transmission. The result S_{21} parameters are shown in Fig. 5.4 that associated radiation loss increases with increasing frequency. Among them, COP substrate has the lowest loss. In addition, the fused silica substrate has some loss characteristics above 1.2 THz, which is caused by the mode dispersion of the propagating THz wave.

5.6 CONCLUSION

This chapter presents an example of the application of a two-color laser filament THz source. In this chapter, the optical and complex dielectric properties of the COPs and other common dielectric substrate materials are extracted by using the transmission THz-TDS system, and the scattering parameter of coplanar waveguide deposited on these materials was simulated by finite element method. A comparison between the results from the characterization of these samples with experiment and simulation should provide insight into the suitability of the potential THz applications. COP materials stand out with their extraordinary performance as high transparency in the THz band, rarely low dielectric loss and relatively flat dispersion over a 4 THz bandwidth. The stability of its optical properties under different intensities of THz irradiation also proves that COP can be fully utilized in a wider range of applications, such as THz lenses, THz cuvettes, etc. In addition, COPs are considered as an ideal substrate material that can reduce the loss of the transmission line because of their high transmittance in the THz band. THz transmission lines are an important part of the research and development topic of THz devices. The structural design and effective application of low-loss THz transmission lines is also a major problem in the field of THz that needs to be solved. This work can provide a meaningful reference for the development of related topics.

REFERENCES:

1. M. Hong, L. Cui, S. Liu, and Y. Li, "Synthesis of Novel Cyclic Olefin Copolymer (COC) with High Performance via Effective Copolymerization of Ethylene with Bulky Cyclic Olefin," Macromolecules **45**, 5397–5402 (2012).
2. O. J. Kwon, H. T. Vo, S. B. Lee, T. K. Kim, H. S. Kim, and H. Lee, "Ring-opening metathesis polymerization and hydrogenation of ethyl-substituted tetracyclododecene," Bull. Korean Chem. Soc. **32**, 2737–2742 (2011).
3. M. Shiotsuki and T. Endo, "Synthesis of hydrocarbon polymers containing bulky dibenzobicyclic moiety by ROMP and their characteristic optical properties," J. Polym. Sci. Part A Polym. Chem. **52**, 1392–1400 (2014).
4. C. A. Bunge, T. Beckers, and M. Gries, *Polymer Optical Fibres: Fibre Types, Materials, Fabrication, Characterisation and Applications* (Elsevier, 2017).
5. F. Pavanello, F. Garet, M. B. Kuppam, E. Peytavit, M. Vanwolleghem, F. Vaurette, J. L. Coutaz, and J. F. Lampin, "Broadband ultra-low-loss mesh filters on flexible cyclic olefin copolymer films for terahertz applications," Appl. Phys. Lett. **102**, (2013).
6. W. Talataisong, J. Gorecki, R. Ismaeel, M. Beresna, D. Schwendemann, V. Apostolopoulos, and G. Brambilla, "Singlemoded THz guidance in bendable TOPAS suspended-core fiber directly drawn from a 3D printer," Sci. Rep. **10**, 1–10 (2020).
7. A. Chahadih, S. Keya, A. Ghaddar, T. Akalin, M. Chudzik, I. Arnedo, I. Arregui, F. Teberio, A. Lujambio, and T. Lopetegi, "Low loss transitions and microstrip lines on cyclo-olefin co-polymer substrate for terahertz applications," Mediterr. Microw. Symp. (2013).
8. T. D. Dorney, R. G. Baraniuk, and D. M. Mittleman, "Material parameter estimation with terahertz time-domain spectroscopy," J. Opt. Soc. Am. A **18**, 1562 (2001).
9. Y. Hashimoto, T. Mori, and S. Kojima, "Broadband terahertz time-domain spectroscopy and low-frequency Raman scattering of glassy polymers: Boson peak of PMMA," Mol. Cryst. Liq. Cryst. **629**, 258–263 (2016).
10. L. Dazhang, J. Cunningham, M. B. Byrne, S. Khanna, C. D. Wood, A. D. Burnett, S. M. Ershad, E. H. Linfield, and A. G. Davies, "On-chip terahertz Goubau-line waveguides with integrated photoconductive emitters and mode-discriminating detectors," Appl. Phys. Lett. **95**, (2009).

11. M. B. Byrne, J. Cunningham, K. Tych, A. D. Burnett, M. R. Stringer, C. D. Wood, L. Dazhang, M. Lachab, E. H. Linfield, and A. G. Davies, "Terahertz vibrational absorption spectroscopy using microstrip-line waveguides," Appl. Phys. Lett. **93**, 182904 (2008).

12. D. Grischkowsky, I. N. Duling III, J. C. Chen, and C.-C. Chi, "Electromagnetic shock waves from transmission lines," Phys. Rev. Lett. **59**, 1663–1666 (1987).

13. C. Nguyen, *Radio-Frequency Integrated-Circuit Engineering* (John Wiley & Sons, Inc, 2015).

14. M. Y. Frankel, S. Gupta, J. A. Valdmanis, and G. A. Mourou, "Terahertz Attenuation and Dispersion Characteristics of Coplanar Transmission Lines," IEEE Trans. Microw. Theory Tech. **39**, 910–916 (1991).

Chapter 6. **CONCLUSIONS**

Two-color laser filament can emit intense, well-directed, ultra-wide spectrum THz electric pulse and are therefore widely adopted. It offers unlimited possibilities for the study of nonlinear interactions of strong THz fields with the matter. However, the filamentation process is accompanied by a complex and diverse set of nonlinear optical processes. They play a non-negligible role in the THz generation mechanism, modulating the THz emission efficiency and waveform. This thesis presents a detailed study of the nonlinear phase modulation effect introduced by the filament formation process itself.

First, the widely used scaling law based on the current model cannot be applied under certain specific conditions. If the optimal THz emission efficiency is obtained by adjusting parameters such as the position azimuth of the BBO crystal at a specific incident power, then its efficiency decreases after changing the incident power. This is because self-phase modulation (SPM) and cross-phase modulation (XPM) introduced additional phases between the fundamental and second harmonic fields (ω and 2ω), thus interfering with the normal phase-matching conditions. We confirm that the BBO position for the best efficiency of THz emission is shifted by studying the relationship between air dispersion and input IR intensity. We construct a function of the third power of the incident pulse energy and oscillating with relative phase between ω and 2ω to fit the experimentally observed output THz intensity evolution. From the oscillation term of this function, we extract an additional phase slippage proportional to the energy of the incident pump pulse energy. The consistency of the linear fit by measuring the two-color spectral spread confirms that the origin of the additional phase is due to SPM and XPM. In addition, the nonzero term of the oscillation curve is also verified by the ratio of the polarization components.

Second, we present the results of the modulation of the THz emission waveform by different incident powers. We recorded the THz waveform evolution for the case of input IR pump energy modulated from 1.75 ~ 2.75 mJ. THz waveform detection is achieved by the ABCD method, which features being unaffected by absorption and dispersion of solid materials. The experimental results show that the THz waveform exhibits a bipolar pattern with the amplitude ratio of positive and negative peaks increasing with the pump pulse energy, and the smooth peak in the tail gradually disappears. Since the microscopic photocurrent model could not explain the phenomenon, we modified the model based on the laser filamentation process. And a simpler model for the modulation process is proposed for simulation. Our calculations show that the modulation is caused by a plasma-induced additional phase that varies with the incident laser intensity. In addition, the smoothed peak in the tail is considered to be caused by the decay of the residual current after the negative peak.

Although a good agreement was obtained for these fits, they are based on approximations and speculations and but not the strict theoretical model. Therefore, these conclusions are very limited and can only be applied under our experimental conditions. More accurate predictions are still based on the high precision 3D moment model - although it will take a lot of effort and time for numerical optimization. Higher-order nonlinear effects, optical pulse distortion, qualitative dynamics, or THz absorption have not yet been fully considered, which means that there is still a lot of work to be done in the future. In addition, the modulating factor is not limited to the intensity of the incident light. Changing the focal length of the lens, the incident spot shape, and polarization characteristics, and even the type of excitation gas are all topics worthy of investigation. Nonlinear effects on the modulation of far-field THz spot, polarization, and other optical field properties have not yet been studied. We believe that the two-color filament is not only a powerful THz source but also a promising tool for deeper investigation of fundamental optics.

The practical significance of this study is to alert those working on the nonlinear interaction of THz fields with matter that the behavior of THz intensity variation by adjusting the pump energy is likely to be very dangerous. Because that can lead to misattribution of experimental observations. For example, when studying the intensity dependence of the material absorption coefficient, it is likely that the phase mismatch in the filament emission will be mistaken for a property of the material itself. Or in the case of coherent oscillations or rotations of molecules induced by strong THz fields, the intensity-induced waveform modulation is mistaken for the material's oscillation mode, and so on. More general practice is to use broadband transmissive high-resistance silicon wafers as THz attenuators. Nevertheless, there are a large number of possible sources of error in the experimental system that need to be carefully considered, such as the nonlinear response of the detector under strong fields, etc. In addition, this study will help those working with broadband THz sources and systems to better understand the generation mechanisms. It may even be possible to exploit this nonlinearity to develop a method for controlling THz waveforms.

Additionally, as an example of the application of a two-color laser filament THz source, we demonstrate optical and complex dielectric properties of the COPs and other common dielectric substrate materials measured by transmission THz-TDS system based on a two-color laser filament source. COP materials stand out with their extraordinary performance as high transparency in the THz band, rarely low dielectric loss and relatively flat dispersion over a 4 THz bandwidth. The stability of its optical properties under different intensities of THz irradiation also proves that COP can be fully utilized in a wider range of applications, such as THz lenses, THz cuvettes, etc. In addition, the finite element simulation results also show the possibility of COP application in THz transmission line substrates. This work can provide a meaningful reference for the development of related topics.

APPENDIX: THE EFFECT OF GROUP VELOCITY DISPERSION IN THE FILAMENT

The propagation of high-intensity femtosecond light pulses along a nonlinear medium is a complex phenomenon. Among them, group velocity dispersion (GVD) plays a crucial role. The GVD of a two-color optical pulse within a laser filament is likely to lead to waveform shaping with group delay, resulting in a change in the THz output. This appendix presents the GVD influence of ionization on the group velocity.

The group velocity v_g and GVD k_2 of the ionized medium are defined as [1]

$$v_g = \left(\frac{dk}{d\omega}\right)^{-1} = c\left[n(\omega) + \omega\frac{dn(\omega)}{d\omega}\right]^{-1}, \tag{A.1}$$

$$\beta_2 = \frac{d^2k}{d\omega^2} = \frac{1}{c}\left[2\frac{dn(\omega)}{d\omega} + \omega\frac{d^2n(\omega)}{d\omega^2}\right]. \tag{A.2}$$

Substitute $n(\omega) = \sqrt{n_0^2 - \frac{\omega_p^2}{\omega^2}}$ in Eqs. (A.1) and (A.2), the group velocity and GVD of the ionized medium can be expressed as follows:

$$v_g = c\frac{\sqrt{n_0^2 - \frac{\omega_p^2}{\omega^2}}}{n_0\left(n_0 + \omega\frac{dn_0}{d\omega}\right)}, \tag{A.3}$$

$$k_2 = \frac{n_0}{n}k_{20} - \frac{\omega_p^2}{c\omega n^3}\left(\frac{n_0}{\omega} + \frac{dn_0}{d\omega}\right)^2, \tag{A.4}$$

where k_{20} is the neutral medium GVD. In the case where the ionization rate is quite low and the neutral is not completely ionized, the total GVD of the medium can be expressed as a simple sum of the neutral medium GVD and the plasma GVD ($k_2 = k_{20} + k_{2i}$). For a gas medium at pressure not substantially exceeding the atmospheric pressure, the free space refractive index $n_0(\omega)$ can be taken unity. Therefore, the second term in the brackets of Eq. (A.4) is negligible in comparison with the first one. Expressions for the variation of GV and plasma GVD with wavelength are

$$v_g = c\frac{\sqrt{n_0^2 - \frac{e^2\lambda^2 N_e}{\pi m_e c^2}}}{n_0\left(n_0 + \omega\frac{dn_0}{d\omega}\right)}, \tag{A.5}$$

$$k_{2i} = -\frac{e^2\lambda^3 N_e}{2\pi^2 m_e c^4\sqrt{1 - \frac{e^2\lambda^2 N_e}{\pi m_e c^2}}}. \tag{A.6}$$

The effect of the plasma density on the GVD within the root sign in Eq. (A.6) is negligible. A simple expression accounting for the plasma GVD for optical range ($\lambda \approx 0.3 \sim 10\mu\text{m}$) has been derived as

$$\beta_{2i} = -\frac{e^2\lambda^3 N_e}{2\pi^2 m_e c^4} = -1.58 \times 10^{-5}\lambda^3 N_e \ [\text{fs}^2/\text{cm}]\,, \tag{A.7}$$

where the wavelength λ and free electron density N_e are given in units of cm and cm^{-3}, respectively. Using the typical wavelength of a Ti:sapphire laser, $\lambda = 800$ nm and a fraction of approximately 0.1% of ionized air molecules, the latter being the characteristic plasma density achieved in a femtosecond filament, a plasma GVD of $\beta_{2i} = -0.22\text{fs}^2/\text{cm}$ is obtained. At millimeter-scale filaments, the group delay dispersion of both fundamental and second harmonic wave is negligible, so these effects are not considered in our theoretical analysis.

References:

1. G. P. Agrawal, *Nonlinear Fiber Optics*, 5th ed. (Artech House Publishers, 2008).

ACHIEVEMENTS

Papers:

1. Gong, C., Zuo. J., Zhang, C. L., “Analysis of Complex Dielectric Constant and Loss Properties of Cyclic Olefin Polymer Substrate by Terahertz Time-Domain Spectroscopy”, Spectroscopy and spectral analysis **38**, 10, 2998-3003 (2018).
2. Gong, C., Kawayama, I., Murakami, H., Teramoto, T., and Tonouchi, M., “Intensity-dependent self-induced dual-color laser phase modulation and its effect on terahertz generation”, Scientific Reports **11**, 498 (2021). https://doi.org/10.1038/s41598-020-80105-7
3. Gong, C., Teramoto, T. and Tonouchi, M., “Observation of the Terahertz Pulse Shaping Due to Intensity-Induced Additional Phase in Two-Color Filaments”, J Infrared Milli Terahz Waves (2021). https://doi.org/10.1007/s10762-021-00797-4.
4. Jiang, H., Gong, C., Nishimura, T. et al. “Terahertz Emission Spectroscopy and Microscopy on Ultrawide Bandgap Semiconductor β-Ga_2O_3”, Photonics **7**, 3, 73 (2020); https://doi.org/10.3390/photonics7030073

Conferences:

1. Gong, C., Kawayama, I., Murakami, H. and Tonouchi, M., “Modulation of Terahertz Generation in Two-Color Photoionization Verified by the Spectral Broadening”, Conference on Lasers and Electro-Optics (CLEO), JW1A.60, (2021.05.12, Online).
2. Gong, C., Teramoto, T. and Tonouchi, M., “Self-induced nonlinearity modulates the THz waveform generated by the two-color laser filament”, The 68th Japan Society of Applied Physics (JSAP) spring meeting, 18a-Z18-7, (2021.03.18, Online).